

# **Human Impact on Groundwater Temperatures**

Zur Erlangung des akademischen Grades einer  
DOKTORIN DER NATURWISSENSCHAFTEN

von der Fakultät für

Bauingenieur, Geo- und Umweltwissenschaften

des Karlsruher Instituts für Technologie (KIT)

genehmigte

DISSERTATION

von

M. Sc. Susanne Amelie Benz

aus Reutlingen

Tag der mündlichen Prüfung:

15.12.2016

Referent: Prof. Dr. habil. Philipp Blum

Korreferent: Prof. Dr. Nico Goldscheider

Karlsruhe (2016)



*“Just a heads up: we're gonna have a superconductor turned up full blast and pointed at you for the duration of this next test. I'll be honest - we're throwing science at the wall here to see what sticks. No idea what it'll do. Probably nothing. Best-case scenario, you might get some superpowers. Worst case, some tumors, which we'll cut out.”*

Cave Johnson, Portal 2





## Abstract

Sustainable water resources and sustainable energy supply are two of the main challenges we face in today's society. Shallow groundwater temperatures (GWT) play a crucial role in both of these areas, especially within densely populated regions. Still, there is a lack in understanding the influence modern humanity has on the thermal regime of the shallow subsurface.

Human activity directly influences ambient air, surface and groundwater temperatures. The most prominent phenomenon is the urban heat island (UHI) effect, which has been investigated particularly in large and densely populated cities. Urban heat islands in the subsurface (SUHI) contain large quantities of energy in the form of elevated groundwater temperatures caused by anthropogenic heat fluxes (AHF<sub>s</sub>) into the subsurface. One of the main heat sources are elevated ground surface temperatures - urban heat islands at surface and subsurface are coupled through conductive heat transport. However, the link between them is not yet sufficiently understood.

The first part of this study discusses shallow GWTs unaltered by human influence. Due to the limited accessibility of aquifers, temperature measurements are scarce and GWTs are largely unknown. Hence, they are often approximated, most commonly by adding an offset to annual mean surface air temperatures. Yet, the value of this offset is not well defined, often arbitrarily set, and rarely validated. Here, the usage of satellite derived land surface temperatures (LST) is recommended instead. 2,548 measurement points in 29 countries are compiled, revealing characteristic trends in the offset between shallow groundwater temperatures and land surface temperatures. Evapotranspiration and snow govern this offset globally through latent heat flow and insulation, respectively. Considering these two processes only, global shallow groundwater temperatures can be estimated with a root mean square error (RMSE) of 1.4 K.

The second part of this study explores the anthropogenic impact on temperatures on a country wide scale. At the example of three temperature datasets in Germany (measured surface air temperature, measured GWT, and satellite-derived LST) the so-called anthropogenic heat intensity (AHI) is introduced. Taking nighttime lights as an indicator of rural areas, it provides the difference between local temperatures and median rural background temperatures. This concept is analogous to the established urban heat island intensity, but applicable independent of land use and location. In Germany, groundwater temperature appears most vulnerable to human activity. While population density has only a minor effect, the anthropogenic heat intensity grows with increasing nighttime lights and declines with increasing vegetation. At the surface of Germany, the highest anthropogenic heat intensity of 4.5 K is found at an open-pit lignite mine near Jülich, followed by the cities Munich, Düsseldorf and Nuremberg with anthropogenic heat intensities of more than 4 K. Overall, surface anthropogenic heat intensities greater zero and thus urban heat islands are observed in communities down to a population of 5,000.

Third, subsurface urban heat islands (SUHI) are investigated more thoroughly. The objective of this part of the study is to quantify the anthropogenic heat fluxes into the subsurface (AHF<sub>S</sub>) and the heat flow they generate in two German cities, Karlsruhe and Cologne. Thus, statistical and spatial analytical heat flux models were developed for both cities. The models include the spatial representation of various sources of AHF<sub>S</sub>: (1) elevated ground surface temperatures, (2) basements, (3) sewage systems, (4) sewage leakage, (5) subway tunnels, and (6) district heating networks. The results show that the district heating networks induce the largest AHF<sub>S</sub> with values greater than 60 W/m<sup>2</sup> and one order of magnitude higher than fluxes from other sources. A covariance analysis indicates that the spatial distribution of the total flux depends mainly on the thermal gradient in the unsaturated zone. On a citywide scale, basements and elevated ground surface temperatures are the dominant sources of heat flow. Overall, 2.1 PJ/a and 1.0 PJ/a of heat are accumulated on average in Karlsruhe and the western part of Cologne, respectively. Extracting this anthropogenically originated energy could sustainably supply significant parts of the urban heating demand. Furthermore, using this heat could also keep groundwater temperatures from rising further.

In the last part of this study, the spatial properties of SUHI and surface UHI are compared in four German cities and correlations of up to 80 % are found. The best correlation is found in older, mature cities such as Cologne and Berlin. However, in 95 % of the analyzed areas, groundwater temperatures are higher than land surface temperatures due to additional subsurface heat sources such as buildings and their basements. Local groundwater hot spots under city centers and under industrial areas are not revealed by satellite-derived land surface temperatures. Hence, an estimation method is proposed that relates groundwater temperatures to mean annual land-surface temperatures, building density, and elevated basement temperatures.

Using this method, regional GWTs in Karlsruhe, Cologne and Berlin are accurately estimated with a root mean square error (RMSE) of 1.4 K. If the previously established influence of evapotranspiration and snow are also taken into account, this RMSE can further be reduced to 0.9 K.

## Kurzfassung

Nachhaltige Energiegewinnung sowie nachhaltige Wassernutzung sind zwei der bedeutendsten Aufgaben unserer Zeit. Oberflächennahe Temperaturen im Untergrund beeinflussen beide Themen stark, vor allem in dicht besiedelten urbanen Regionen. Trotzdem ist nur wenig über den Einfluss der modernen Zivilisation auf Grundwassertemperaturen bekannt.

Menschliche Aktivitäten beeinflussen die Umgebungstemperaturen in der Luft, an der Oberfläche und im Grundwasser. Am bekanntesten ist das Phänomen der urbanen Wärmeinsel, welches vielfach in großen und dicht besiedelten Städten untersucht wurde: Temperaturen innerhalb des urbanen Einflussgebiets sind gegenüber dem ländlichen Umland deutlich erhöht. Im Untergrund wird diese Temperaturanomalie durch anthropogenen Wärmefluss in den Grundwasserleiter verursacht. Eine der dominantesten Wärmequellen ist die erhöhte Oberflächentemperatur – urbane Wärmeinseln an der Oberfläche und im Untergrund sind durch konduktive Wärmetransportprozesse miteinander verbunden. Allerdings ist der genaue Zusammenhang bisher unzureichend erforscht.

Im ersten Teil dieser Arbeit werden oberflächennahe Grundwassertemperaturen diskutiert, die nicht durch den Menschen beeinflusst werden. Auf Grund des limitierten Zugangs zum Grundwasserleiter können Temperaturen nur vereinzelt gemessen werden und sind daher größtenteils unbekannt. Sie werden daher oft abgeschätzt, meistens durch Addition eines konstanten Offsets zu Jahresmittelwerten der Lufttemperatur. Allerdings ist der genaue Wert dieses Offsets nicht klar definiert und wird daher oft frei gewählt und unzureichend geprüft. In dieser Arbeit wird nun die Verwendung von Landesoberflächentemperaturen statt Lufttemperaturen vorgeschlagen, da die von Satelliten erfassten Landesoberflächentemperaturen weltweit und flächendeckend verfügbar sind. Anhand von 2.548 Grundwassermessstellen in 29 Ländern wird das Offset zwischen LST und Grundwassertemperatur bestimmt und charakteristische Trends werden erforscht. Evapotranspiration und Schnee steuern dieses Offset global durch latenten Wärmefluss bzw. durch Wärmedämmung. Unter Beachtung dieser Prozesse können globale, oberflächennahe Grundwassertemperaturen mit einem Fehler (root mean square error) von 1.4 K abgeschätzt werden.

Im zweiten Teil dieser Arbeit wird der anthropogene Einfluss auf Temperaturen erforscht. Anhand von drei Temperaturdatensätzen in Deutschland (gemessene Lufttemperaturen, gemessene Grundwassertemperaturen und satellitenerfasste Landesoberflächentemperaturen) wird die sogenannte anthropogene Wärmeintensität eingeführt. Es handelt sich dabei um die Differenz zwischen lokalen Temperaturen und gemittelten ländlichen Hintergrundtemperaturen. Satellitenerfasstes Nachtlicht dient dabei als Indikator für ländliche Gebiete. Das Konzept ist analog zur etablierten Intensität der urbanen Wärmeinseln, kann aber auf alle Temperaturmessungen unabhängig von

Landnutzung und Lage angewendet werden. Die Ergebnisse zeigen, dass die gemessenen Grundwassertemperaturen am stärksten auf menschliche Aktivität reagieren. Während die Bevölkerungsdichte nur einen geringen Effekt auf die anthropogene Wärmeintensität hat, steigt diese mit zunehmendem Nachtlicht und sinkt mit zunehmender Vegetation. An der Oberfläche Deutschlands findet sich die höchste anthropogene Wärmeintensität (4,5 K) bei einem zur Förderung von Braunkohle betriebenen Tagebau bei Jülich. Intensitäten von mehr als 4 K werden außerdem in München, Düsseldorf und Nürnberg gefunden. Positive anthropogene Wärmeintensitäten finden sich auch in kleineren Gemeinden ab 5.000 Einwohnern.

Als Drittes werden urbane Wärmeinseln im Untergrund genauer untersucht. Das Ziel dieses Teils der Arbeit ist es, die anthropogene Wärmeflussdichte in den Untergrund sowie den gesamten daraus resultierenden Wärmestrom für Karlsruhe und Köln zu quantifizieren. Für beide Städte wurden hierfür räumlich aufgelöstes, statistisch analytisches Wärmetransportmodelle entwickelt, die folgende anthropogene Wärmequellen implementiert: (1) erhöhte Oberflächentemperaturen, (2) Gebäudekeller, (3) Abwassersysteme, (4) Abwasserleckagen, (5) U-Bahntunnel und (6) Fernwärmenetze. Die Ergebnisse zeigen, dass das Fernwärmenetz die höchste Wärmestromdichte mit Werten über  $60 \text{ W/m}^2$  verursacht. Alle anderen untersuchten Wärmequellen verursachen Wärmestromdichten von etwa einem Zehntel dieser Größe. Eine Analyse der Kovarianz zeigt, dass die räumliche Verteilung der gesamten Wärmestromdichte aller Wärmequellen hauptsächlich auf den thermalen Gradienten der ungesättigten Zone beruht. Für das gesamte Untersuchungsgebiet sind Gebäudekeller und erhöhte Oberflächentemperaturen die dominantesten Wärmeflussquellen. Insgesamt werden durchschnittlich 2,1 PJ/a bzw. 1,0 PJ/a Wärme aus anthropogenen Quellen in den urbanen Untergrund von Karlsruhe bzw. dem linksrheinischen Teil Kölns eingetragen. Diese Wärmemenge würde ausreichen, um einen signifikanten Teil des urbanen Heizwärmebedarfs zu decken. Gleichzeitig würde die Nutzung dieser Energie auch ein weiteres Erwärmen der urbanen Grundwassertemperaturen verhindern.

Im letzten Teil dieser Arbeit werden die urbanen Wärmeinseln an der Oberfläche und im Untergrund anhand von vier deutschen Städten miteinander verglichen; Dabei werden räumlich Korrelationen von bis zu 80 % festgestellt. Die besten Korrelationen finden sich in alten etablierten Städten wie z.B. Köln und Berlin. In 95 % der analysierten Fläche sind die Grundwassertemperaturen wärmer als die Landesoberflächentemperaturen. Dieser Unterschied wird durch unterirdische Wärmequellen wie etwa Gebäudekeller hervorgerufen. Dementsprechend werden lokale Temperaturanomalien unter dem Stadtzentrum sowie unter Industriegebieten nicht von den satellitenerfassten Landesoberflächentemperaturen aufgezeigt. Um diese lokalen Wärmeinseln besser abschätzen zu können, wurde daher eine neue Abschätzungsmethode entwickelt, die Grundwassertemperaturen anhand von jahresmittleren Landesoberflächentemperaturen, Gebäudedichte und Kellertemperaturen bestimmt.

Mit dieser Methode können regionale Grundwassertemperaturen in Karlsruhe, Köln und

Berlin mit einem Fehler (root mean square error) von 1,4 K abgeschätzt werden. Wird die im ersten Teil der Arbeit eingeführte Abschätzung durch Evapotranspiration und Schnee ebenfalls beachtet, kann die Genauigkeit weiter erhöht werden. Ein Fehler (root mean square error) von lediglich 0.9 K zwischen geschätzter und gemessener Grundwassertemperatur wird erreicht.



# Contents

Abstract .....	i
Kurzfassung .....	iii
Contents .....	vii
Abbreviations .....	ix
1. Introduction .....	1
1.1. Scientific background .....	1
1.2. Objectives .....	6
1.3. Structure of the Thesis .....	7
2. Global Patterns of Shallow Groundwater Temperatures .....	9
Graphical Abstract .....	9
Abstract .....	10
2.1. Introduction .....	11
2.2. Material and Methods .....	13
2.3. Results and Discussion .....	16
2.4. Conclusion .....	21
Acknowledgements .....	22
Supplementary Material .....	23
3. Identifying Anthropogenic Anomalies in Air, Surface and Groundwater Temperatures in Germany .....	35
Graphical Abstract .....	35
Abstract .....	36
3.1. Introduction .....	37
3.2. Material and Methods .....	39
3.3. Results and Discussion .....	45
3.4. Summary and Conclusion .....	51
Acknowledgment .....	52
Supplementary Material .....	53
4. Spatial Resolution of Anthropogenic Heat Fluxes into Urban Aquifers .....	61
Graphical Abstract .....	61
Abstract .....	62
4.1. Introduction .....	63

4.2.	Material and Methods .....	65
4.3.	Results and Discussion .....	79
4.4.	Conclusions.....	88
	Acknowledgments.....	89
	Supplementary Material .....	90
5.	Linking Surface Urban Heat Islands with Groundwater Temperatures .....	93
	Graphical Abstract .....	93
	Abstract .....	94
5.1.	Introduction.....	95
5.2.	Materials and Methods.....	97
5.3.	Results.....	102
	Acknowledgements .....	109
	Supplementary Material .....	110
6.	Synthesis.....	115
6.1.	Estimating Urban Groundwater Temperatures .....	115
6.2.	Summary and Conclusion .....	120
6.3.	Perspective .....	122
	Acknowledgements .....	125
	Declaration of Authorship.....	127
	References .....	129
	Curriculum Vitae.....	153



## Abbreviations

AHF <sub>s</sub>	anthropogenic heat flux into the subsurface
AHI	anthropogenic heat intensity
eGWT	estimated groundwater temperature
ET	evapotranspiration
GST	ground surface temperature
GWT	groundwater temperature
LST	land surface temperature
SAT	surface air temperature
SUHI	subsurface urban heat island
UHI	urban heat island
UHII	urban heat island intensity



# 1. Introduction

## 1.1. Scientific background

Only meters below our feet, shallow aquifers are habitat (1), provide freshwater storage (2), and serve as sustainable energy source (3) all in one. They are elementary in geosciences and hydrology, and gain attention in ecology and climate science. Yet we know only little about their thermal conditions, their link to land surface temperatures, and the impact man-made climate change (4) has on them.

### 1.1.1. The Thermal Regime of Shallow Aquifers

Assuming local thermodynamic equilibrium between solid and fluid, groundwater temperatures (GWT) and subsurface temperatures are considered equal (5). They are governed by heat flow from the Earth's interior and heat flow from temperature variations at the ground surface. The temperature  $T(z, t)$  as a function of time and depth can best be described as a superposition of the mean surface temperature  $T_0$ , an increase in temperature  $\Gamma(z)$  governed by geothermal heat flow, and a temperature variation  $\Delta T(z, t)$  resulting from surface temperature variations (6).

$$T(z, t) = T_0 + \Gamma(z) + \Delta T(z, t) \quad (1.1)$$

Geothermal heat flux, which receives its energy from naturally occurring radioactive decay, has a global average of 86 mW/m<sup>2</sup> and a continental average of approximately 65 mW/m<sup>2</sup> (7). Depending on the local geothermal heat flux and thermal conductivity this results in a temperature increase of 1 K per 20 to 40 m (8). Near the surface geothermal temperature increase lessens ( $\lim_{z \rightarrow 0} \Gamma(z) = 0$ ) and can thus be neglected.

Heat from the ground surface is transported by two distinct processes: conductive heat transport by way of thermal diffusion and heat transport in form of infiltration or seepage. As advective heat transport processes in porous media occur mainly in horizontal direction (9), they can be disregarded when discussing subsurface temperature as a function of depth. Hence, shallow groundwater temperature (GWT) profiles are often described by a 1-D vertical diffusion equation with the following solution (9):

$$\begin{aligned} T(z, t) &= T_0 + \Delta T(z, t) \\ &= T_0 + \Delta T_0 \cdot \exp\left(-2\pi \frac{z}{\Lambda}\right) \cdot \cos\left(2\pi \left(\frac{t}{t_0} - \frac{z}{\Lambda}\right)\right) \end{aligned} \quad (1.2)$$

with

$$\Lambda = 2\sqrt{\pi\alpha t_0} \quad (1.3)$$

where  $\Delta T$  is the amplitude of the temperature fluctuation at the ground surface,  $t_0$  is the period of the temperature fluctuation and  $\alpha$  is the thermal diffusivity of the subsurface. Figure 1.1. displays the temperature distribution for shallow depth determined via equation 1.2. The two major components when describing shallow GWT as a function of time and depth are the time lag  $\lambda = \frac{z}{\Lambda}$  and the damping factor  $\delta = \exp\left(-2\pi\frac{z}{\Lambda}\right)$  of the surface temperature signal, both of which increase with depth. Hence annual temperature variations are only observed down to approximately 20 m (10), depending on the thermal properties of the underground. Additionally annual mean temperatures of all depth can be considered constant and equal to annual mean ground surface temperatures ( $z = 0$ ).

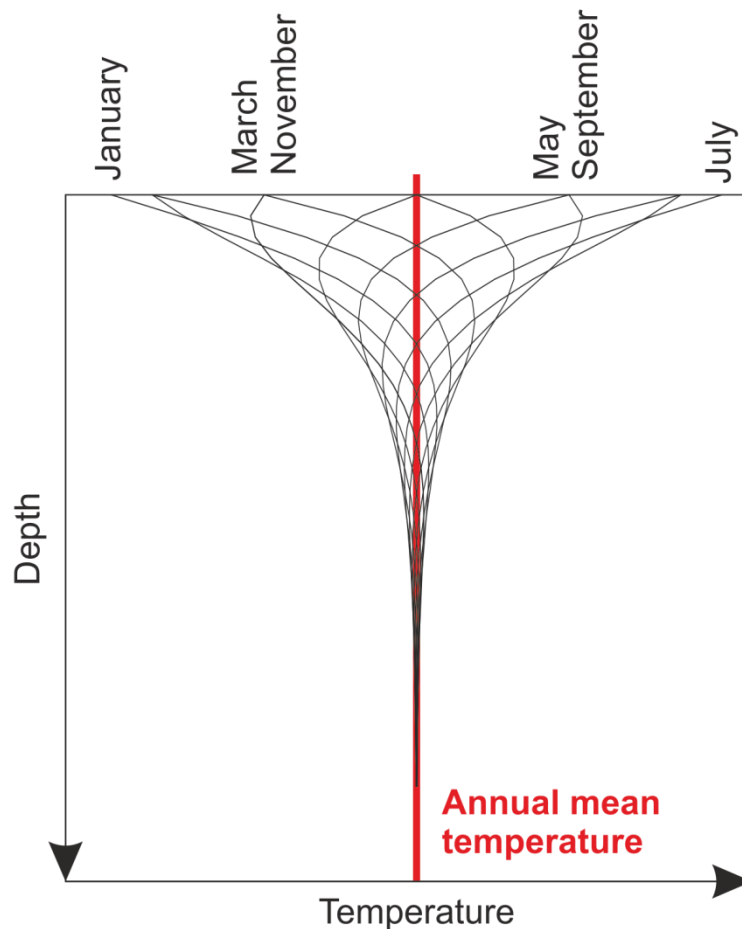


Figure 1.1. Seasonal variation in shallow-depth groundwater temperatures.

### 1.1.2. Land Surface Temperatures

In recent years a new surface temperature measurement has been established: land surface temperature (LST), the radiative skin temperature of the ground as seen from above, gives a unique insight into Earth's surface energy balance (11).

Depending on its skin temperature each body emits electromagnetic radiations. For a perfect black body – an object that absorbs all incident electromagnetic radiation – the spectral radiance at a given temperature  $T$  is provided by Placks's law. Hence black body temperature can be obtained by measuring thermal radiation at a fixed wavelength. Real objects however do not absorb all incident electromagnetic radiation. Thus, due to the conservation of energy, they also have a lower thermal emission than a black body. Hence, the emissivity, the ratio between radiance of an object and of a black body at the same temperature, needs to be taken into account. If the emissivity is known or can be estimated, skin temperatures of any given object can be derived from its remotely sensed electromagnetic radiation, most commonly at infrared wavelengths (12).

Land surface temperatures (LST) of Earth can thus be derived via satellite. Most used data are either LST retrieved from the LADSAT thermal channel (13) or LST received from Moderate Resolution Imaging Spectroradiometer (MODIS) data (14). MODIS is aboard the Terra and Aqua Satellites, both of which provide two observations daily, one at nighttime and one at daytime. LST is retrieved for all land pixels under clear sky conditions in a resolution of approximately  $1 \text{ km} \times 1 \text{ km}$ , using a generalized split-window algorithm (15). MODIS LST has been validated by several studies: By comparing MODIS LST to in situ LST measurements Wan et al (2002) found an agreement of  $\pm 1 \text{ K}$  (16). By 2006 the algorithm (Version 5) had been improved and the root mean square error between MODIS and in situ LST time series measurements was found to be less than  $0.7 \text{ K}$  (17).

The difference in satellite derived LST and directly measured ground surface temperatures (GST, 3-5 cm below ground) has been analyzed for permafrost regions in Alaska and Canada by Hachem et al. (2012). They found a good correlation (Pearson correlation coefficient  $R = 0.90$ ) for a yearlong time-series with LSTs being on average  $5.4 \text{ K}$  colder than GSTs. However, for snow free periods LST was on average  $2.2 \text{ K}$  warmer than GST due to missing insulation from snow cover (18). A comparison of LST and near surface air temperatures (1 to 3 m above ground) at the same measurement locations found LST to be on average  $1.8 \text{ K}$  colder than air temperatures for the whole year comparison. Again, during snow free periods LST is  $0.6 \text{ K}$  warmer than air temperatures (18). A comparison of MODIS LST with air temperatures over the continental USA found a correlation of  $R^2 = 0.88$  for data observed with the Terra satellite and  $R^2 = 0.93$  for data observed with the Aqua satellite (19). When analyzing the different biomes (forest, grass, desert and mediterranean) of the US, Zhan et al (2014) found correlations  $R^2 > 0.80$  for all biomes but the mediterranean one, primarily located in California ( $R^2$  of approximately 0.3 to 0.8). When comparing average temperatures of seasonal air temperatures and MODIS LST, differences ranging from  $-7.5 \text{ K}$  to  $+7.5 \text{ K}$  were found (19).

### 1.1.3. Man-made Climate Change

Climate and temperature are strongly affected by humans (4). Over the 20<sup>th</sup> century Earth's temperature has increased by 0.6 K with two main periods of warming from 1910 to 1945 and from 1976 onwards (20). While this trend is most commonly observed at the surface (21,22) or air (23,24), it has also been linked to groundwater temperatures (25). Consequences for earth ecology are severe: on the basis of mid-range climate-warming scenarios it has been predicted that 15 – 37 % of species will be 'committed to extinction' by 2050 (26).

The main cause of this global climate change is greenhouse gas emission that alters the Earth's atmospheric composition (27). However, land use change has a profound impact on regional climate as well (27,28). Simulations show a significant increase in temperature and a significant decrease in evapotranspiration over the Amazon basin in response to deforestation (29).

#### Urban Heat Islands

The most drastic change in temperature caused by humans can be found within cities. Here temperatures are typically increased compared to their rural surrounding (30). This temperature anomaly is thus called urban heat island (UHI). It exists in all diverse layers of a city, from atmosphere (31-33) to surface (34,35) to groundwater (36), and is most often quantified by the so called urban heat island intensity (UHII), the difference in maximal urban temperatures and rural background temperatures (30). Above ground UHIs vary greatly throughout the year (37,38) and day (32,39). Maximal UHIIs are commonly observed during nighttime and in summer (40). However, depending on location, UHIs display major differences, especially during daytime (34). When comparing the properties of UHIs for different biomes within the USA, Imhoff et al. found that cities in desert and xeric shrublands commonly display urban cooling during summer days. At the same time cities in temperate broadleaf and mixed forest (northern group) had UHIIs of more than 9 K (41).

Above ground UHIs have a tremendous impact on human life, energy consumption and the urban ecosystem (42). They increase vulnerability to heat-related morbidity and mortality (43,44): In France, for example, most consequences of the heat wave in August 2003 occurred in Paris, where an increase of 130 % in expected mortality was observed (45). Furthermore, the cooling demand of buildings within a city center is approximately 13 % higher than in similar buildings in rural areas (46). Watkins et al. (2002) determined a 22% reduction in heating load and a 25 % cooling load increase for central London (47). UHIs also change urban phenology: plants tend to develop up to a few weeks earlier in cities compared to their rural surrounding (48). In colder climates, UHIs are further linked to an increase in soft scale insect pests (49) and arthropods (50).

Subsurface urban heat islands (SUHI) have been observed in various cities worldwide such as Virginia Beach, USA (51), Winnipeg, Canada (52), London, UK (53), Oberhausen, Germany (54), Istanbul, Turkey (55), Jakarta, Indonesia (56), Osaka, Japan, and Bangkok, Thailand (57). While various unfavorable issues originate from the UHI in the atmosphere, the SUHIs provide economic and ecological advantages for the use of shallow geothermal energy systems (58). Arola and Korkka-Niemi (2014) showed that in southern Finland about 50 - 60 % more peak heating power could be utilized from urban areas in contrast to rural areas (59). Furthermore, the geothermal potential of SUHI exceeds the annual residential heating demand in many urban areas (60). Extracting this energy efficiently could reduce emission of CO<sub>2</sub> and other greenhouse gases (61,62).

## 1.2. Objectives

The first aim of this study is to contribute to a better understanding of global shallow groundwater temperatures (GWT) by establishing a link between satellite-derived land surface temperature (LST) and measured GWT. In addition the influence evapotranspiration and snow cover have on this link will be quantified and used to estimate shallow groundwater temperatures on a global scale.

Further aims of this study are related to the human impact on local temperatures. One focus is to quantify said impact for larger, countrywide areas and to study the impact smaller settlements and industrial sites have on temperatures in air, surface and groundwater. Subsequent to the identification of non-urban anthropogenic heat anomalies, another aim is to better understand the spatial properties and sources of subsurface urban heat islands (SUHI). In addition, the question of SUHIs as a sustainable source of geothermal heating will be addressed.

Finally, this study aims to answer the question whether above and below ground urban heat islands are linked and to develop a method to estimate urban GWT from satellite-derived data utilizing the findings from the before mentioned aims.



### 1.3. Structure of the Thesis

The presented work is a cumulative dissertation that consists of four individual studies enclosed in Chapters 2 - 5. In Chapter 6 the individual results of these studies will be connected followed by a summary and conclusion. All studies were submitted to ISI-listed journals. Two of them are already published, one is in press, and one is currently under review.

Chapter 2 contains the third study “*Global Patterns of Shallow Groundwater Temperatures*”. It is currently under review at *Environmental Research Letters* and discusses the offset between shallow groundwater temperatures and land surface temperatures on a global scale. On the basis of 2,584 groundwater temperature measurement points in 29 countries this offset is linked to evapotranspiration and snow cover through latent heat flow and insulation. Considering these two processes, a global map of estimated shallow groundwater temperatures is presented.

In Chapter 3 the fourth study of this dissertation is given. It is entitled “*Identifying anthropogenic anomalies in air, surface and groundwater temperatures in Germany*” and has been accepted by *Science of the Total Environment*. This study explores the anthropogenic influence on the thermal regime of Germany for surface air temperature, land surface temperature and shallow groundwater temperatures alike. A novel parameter, the anthropogenic heat intensity, is introduced that quantifies the human impact on temperatures for each measurement point (for surface air temperature and shallow groundwater temperature) or pixel (for land surface temperature) individually, regardless of land cover and land use. Using this parameter the human impact on air, surface and groundwater is compared, and main instances of anthropogenic temperature anomalies are identified. Furthermore the impact of smaller settlements and industrial sites on temperature is studied.

Chapter 4 gives the first study entitled “*Spatial Resolution of Anthropogenic Heat Flux into Urban Aquifers*”, published in *Science of the Total Environment*. It quantifies the main drivers and potential of subsurface urban heat islands for Karlsruhe and Cologne, Germany. A statistical analytical heat flux model is developed which determines the spatial variability of the anthropogenic heat flux into the subsurface for six dominant heat sources: elevated surface temperatures, buildings, sewage systems, sewage leakage, subway tunnels, and district heating networks. To account for the uncertainty of all input parameters a Monte Carlo approach is integrated into the model. Furthermore the determined annual anthropogenic heat flow into the urban underground is compared to the annual heating demand in order to find the sustainable geothermal potential of both cities.

Chapter 5 is the second publication, “*Linking Surface Urban Heat Islands with Groundwater Temperatures*”. It was previously published in *Environmental Science &*

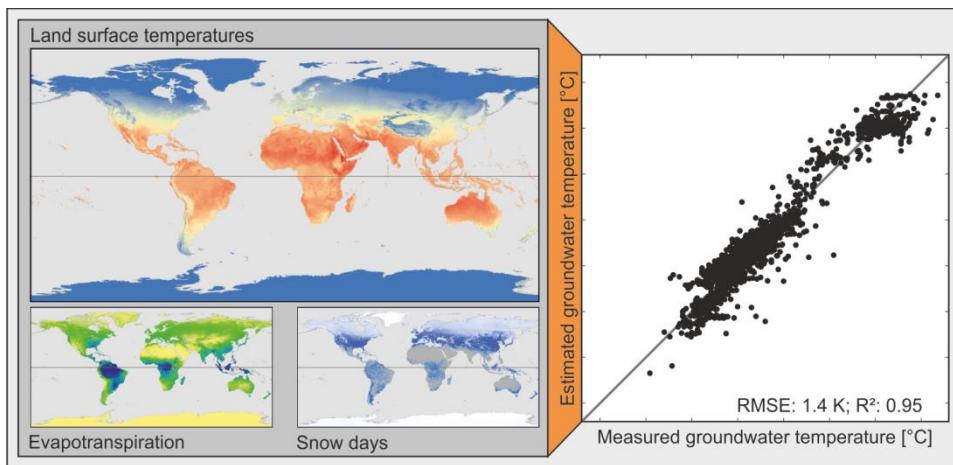
*Technology.* Using satellite-derived land surface temperatures and interpolated groundwater temperature measurements, the spatial properties of surface and subsurface urban heat islands are compared. Main differences are linked to the anthropogenic heat flux determined in Chapter 4. At the example of four German cities a novel estimation technique is introduced that relates urban groundwater temperatures to mean annual land surface temperatures, building density and elevated basement temperatures. Additionally the influence of groundwater flow on temperature is taken into account for Karlsruhe and Cologne.

Finally, Chapter 6 combines findings from Chapter 2 and Chapter 5 and illustrates a method to estimated shallow urban groundwater temperatures that considers all relevant parameters mentioned above: land surface temperature, evapotranspiration, snow cover, building density, and elevated basement temperatures.

## 2. Global Patterns of Shallow Groundwater Temperatures

*Reproduced from: Benz, S. A.; Bayer, P.; Blum, P., Global patterns of shallow groundwater temperatures, Environmental Research Letters, under review.*

### Graphical Abstract



## **Abstract**

Below our feet, shallow aquifers are habitat, provide drinking water, and serve as sustainable energy source, all of which are crucially impacted by the thermal regime of the subsurface. Due to the limited accessibility of aquifers however, temperature measurements are scarce. Most commonly, shallow groundwater temperatures are approximated by adding an offset to annual mean surface air temperatures. Yet, the value of this offset is not well defined, often arbitrarily set, and rarely validated. Here, we propose the usage of satellite-derived land surface temperatures instead of surface air temperatures. 2,548 measurement points in 29 countries are compiled, revealing characteristic trends in the offset between shallow groundwater temperatures and land surface temperatures. Here it is shown that evapotranspiration and snow govern this offset globally through latent heat flow and insulation. Considering these two processes only, global shallow groundwater temperatures are estimated in a resolution of approximately  $1 \text{ km} \times 1 \text{ km}$ . When comparing these estimated groundwater temperatures with measured ones a coefficient of determination of 0.95 and a root mean square error of 1.4 K is found.

## 2.1. Introduction

Sustainable water resources and energy supply are two of the main challenges in today's society (e.g. (63-67)). Shallow groundwater temperatures play a crucial role in both of these challenges. For example, they affect microbial activity in aquifers thus, giving a unique insight into oxygen depletion in huge quantities of the Earth's water supply (68), and are the key factor to determining the usability and the potential of shallow geothermal energy (60,69,70). Additionally, the temperatures of the surface and subsurface are closely linked. The coupling between both is utilized to reconstruct ground surface temperature histories using both borehole temperature data (71,72) and noble gas temperatures (73), and to analyze the impact of climate change on the subsurface (25,74,75). There is growing interest in understanding the effect of the thermal and hydrogeological regime of the subsurface on climate (76). A main hurdle, however, is the uncertainty of shallow groundwater temperature (GWT) distribution. Since direct measurements are scarce and measurement points are limited, GWT is typically estimated by adding an offset to annual mean surface air temperatures. While the existence of this offset has long been discussed (77), its value has yet to be validated on a larger scale.

In a closed system without latent heat, the surface energy balance predicts near surface temperatures and shallow subsurface temperatures to be in equilibrium. Accordingly, studies set in warm or moderate climate find the offset between both close to zero (78). On a global scale, however, it is highly variable. Latent heat caused by evapotranspiration (ET) plays a key role in the surface energy balance. Its effects on surface climate have been thoroughly discussed (79) and it has been determined that an increase in ET will decrease measured surface temperatures (80). Additionally, ET is closely linked to natural precipitation and recharge (81). This effect is most often discussed in regards to groundwater availability in changing climates (82,83); however recharge also affects shallow GWTs directly (8). Still, the effect of ET on the offset between land surface temperature (LST) and GWT is unknown.

In higher and colder latitudes the offset is often dominated by snow. Here, with its low thermal conductivity, the snow cover functions as an insulator and prevents the conduction of cold surface temperatures into the subsurface layer (84). Studies set in northern regions found subsurface temperatures to be significantly warmer than surface temperatures (18,85).

On a regional scale, shallow GWT is also influenced by a multitude of factors such as anthropogenic heat flux (86), geothermal hot spots, groundwater flow, and groundwater depth (87) since temperature typically increases with depth.

Here, we focus on the global scale offset between the 10-year mean groundwater temperatures (GWT) and surface temperatures. Since annual mean surface air temperatures are only available in areas where long-term monitoring stations are installed,

we propose the use of satellite-derived land surface temperatures (LST) instead. By comparing a global dataset of measured GWT with decadal mean LST, we determine and analyze the offset  $\Delta T = GWT - LST$  and quantify the influence from ET and snow cover. Other more regional influences cannot be addressed globally. Finally, the offset and therefore GWTs are estimated on a global scale using only satellite-derived data.

## 2.2. Material and Methods

### 2.2.1. Groundwater Temperatures

Overall, 2,548 shallow measurement points in 29 countries and two overseas territories were compiled that provide (multi)-annual mean groundwater temperatures (GWT) without a seasonal bias (Table S2.1). The distribution of GWT data is uneven and has a bias towards the northern hemisphere, with only 14 % of all measurement points being located south of the equator. However, this is not considered crucial since the offset between GWT and land surface temperature (LST) in both hemispheres show similar behavior for equal latitudes (Fig. S2.1). Because all measurement points are south of 61° latitude, GWTs closer to the polar regions are not addressed.

All measurements were performed in a depth of less than 60 m, including springs, since this is the minimum depth that a temperature signal penetrates in 10 years (9,88). However, the majority of the points correspond to measurements in a depth of no less than 30 m. At each measurement point, GWTs were read at least once in the time frame of 01/Jan/2005 to 31/Dec/2014. While temperatures measured in a depth of more than 20 m generally do not indicate any seasonal influences (10), temperatures measured above this depth do (9). Hence, the temperatures have to be measured uniformly over the span of the various seasons to generate a bias-free mean. To estimate whether the mean temperature of a measurement location is biased by seasonal temperature variations, a variable called seasonal radius  $r$  is introduced. It determines whether measurements were taken uniformly over the span of the seasons ( $r = 0$ ) or if all measurements were taken in the same month ( $r = 1$ ). To determine  $r$ , every measurement of a time series is first converted to a vector with a length of 1.0 and a direction corresponding to the month of measurements. Next, the mean of all measurement-vectors of a single measurement point is determined. The length of the resulting mean vector is the seasonal radius. Figure S2.2a gives an example of a well that was measured twice, once in November and once in June. Figure S2.2b depicts the seasonal radii of all analyzed measurement points with a measurement depth of less than 20 m located in France and its overseas territories (Table S2.1). The influence of this seasonal radius on GWTs was analyzed (Fig. S2.3) and it was found that measurement points with a seasonal radius  $\leq 0.25$  can be considered bias free. Hence, the following rules for measurement point selection were determined:

- The maximum measurement depth is 60 m.
- If the measurement depth is  $\leq 20$  m, only points that have a seasonal radius of  $\leq 0.25$  were considered.
- If the measurement depth is not known, only points that have a well depth  $\leq 60$  m and a seasonal radius  $\leq 0.25$  were considered.

- If neither measurement depth nor well depth are known but the raw data shows seasonal variations of more than 1 K, points with a seasonal radius  $\leq 0.25$  were considered.
- If temperatures were taken after pumping, only points with a well depth between 20 m and 60 m were considered.

### **2.2.2. Land Surface Temperatures**

To determine the 10-year arithmetic mean (01/2005 – 12/2014) of land surface temperatures (LST) we used MODIS daily products MOD11A1 and MYD11A1 (15,89), as obtained from NASA's TERRA and AQUA satellites, courtesy of the NASA Land Processes Distributed Active Archive Center (LP DAAC), USGS/Earth Resources Observation and Science (EROS) Center, Sioux Falls, South Dakota, <https://lpdaac.usgs.gov>. Each satellite views the entire planet twice daily giving four LST measurements a day. MODIS-derived LSTs have been previously validated by several studies (16,90-92). Because LSTs are only retrieved for clear sky observations, they have a bias towards non cloudy days. To correct for this bias in regards to the seasonal variations of cloud cover, the 10-year mean was determined in three steps. First, the mean temperature of each month was determined for the years 2005 to 2014. Out of these, the 10-year mean for each month was determined before combining this data to a single 10-year mean map. This was performed using Google Earth Engine (93) and was exported in a resolution of approximately  $1 \text{ km} \times 1 \text{ km}$  ( $0.009^\circ \times 0.009^\circ$ ).

Over the analyzed 10-year time period no significant change in global LST is observed (Fig. S2.4). Hence, climate change was not consider when comparing 10-year mean LSTs with GWTs that were often measured only towards the end of the late analyzed 10-year time period.

### **2.2.3. Evapotranspiration**

Evapotranspiration data was gathered from the Noah 2.7.1 model in the Global Land Data Assimilation System (GLDAS) data products Version 1 (94) (spatial resolution:  $0.24^\circ$ ). These evapotranspiration data have previously been validated by several studies (95-98). In this study, the decadal mean (01/2005 – 12/2014) evapotranspiration (ET) was determined using the Google Earth Engine (93) and was exported in a resolution of approximately  $1 \text{ km} \times 1 \text{ km}$ .

### **2.2.4. Snow Days**

Information on snow days was derived from MODIS Terra and Aqua Snow Cover Daily L3 Global 500 m Grid, Version 5 (99), products MOD10A1 and MYD10A1, courtesy of the National Snow and Ice Data Center (NSIDC). The data has previously



been validated by several studies (100-102). Using Google Earth Engine (93), the percentage of snow days in the 10 years from 01/2005 to 12/2014 was determined by dividing the number of days classified as “snow” by the sum of the days classified as either “no snow” or “snow”. The data was exported in a resolution of approximately 1 km  $\times$  1 km.

### 2.2.5. Estimating Groundwater Temperatures

In this study GWTs are estimated using satellite-derived data only. Two distinct effects on the offset between GWT and LST are quantified: snow cover insulates warm groundwater temperatures and latent heat flux, caused by evapotranspiration, factors into the surface energy balance, thus decreasing LSTs. The total offset,  $\Delta T_{Total} = \Delta T_{ET} + \Delta T_S$  can be described as the superposition of the offsets caused by evapotranspiration ( $\Delta T_{ET}$ ) and the offsets caused by the duration of snow cover ( $\Delta T_S$ ). The latter is quantified as the percentage of snow days during the analyzed 10 years. Because both pairs (ET and latent heat, and snow days and insulation) are linearly dependent, a linear fit  $\Delta T_{Total} = \Delta T_{ET} + \Delta T_S = (a \cdot ET) + (b \cdot snow\ days)$  is used to estimate the global offset. Fitting was performed in MATLAB R2013a with the function “nlinfit” for nonlinear regression. The coefficients are estimated using iterative least squares estimation. Initial values are  $a = 10^4 \text{ K } \frac{\text{s} \cdot \text{m}^2}{\text{kg}}$  and  $b = 7 \text{ K}$ . The 95 % prediction interval half-width for a new observation was determined using the function “nlpredci”.

### 2.3. Results and Discussion

The compiled ten year mean land surface temperatures (LST) and (multi)-annual mean groundwater temperatures (GWT) are displayed in Figure 2.1. For 83 % of all measurement points, GWTs are warmer than LST. The average offset  $\Delta T = GWT - LST$  is  $1.2 \pm 1.5$  K (Fig. S2.6). The influence of GWT measurement depth on the offset was analyzed for all measurement points with a known measurement depth (Austria, France and its overseas territories, Table S2.1). It revealed an increase in temperature by only 0.02 K/m (Fig. S2.5). Consequently, the impact of depth on mean groundwater temperature (GWT) was disregarded.

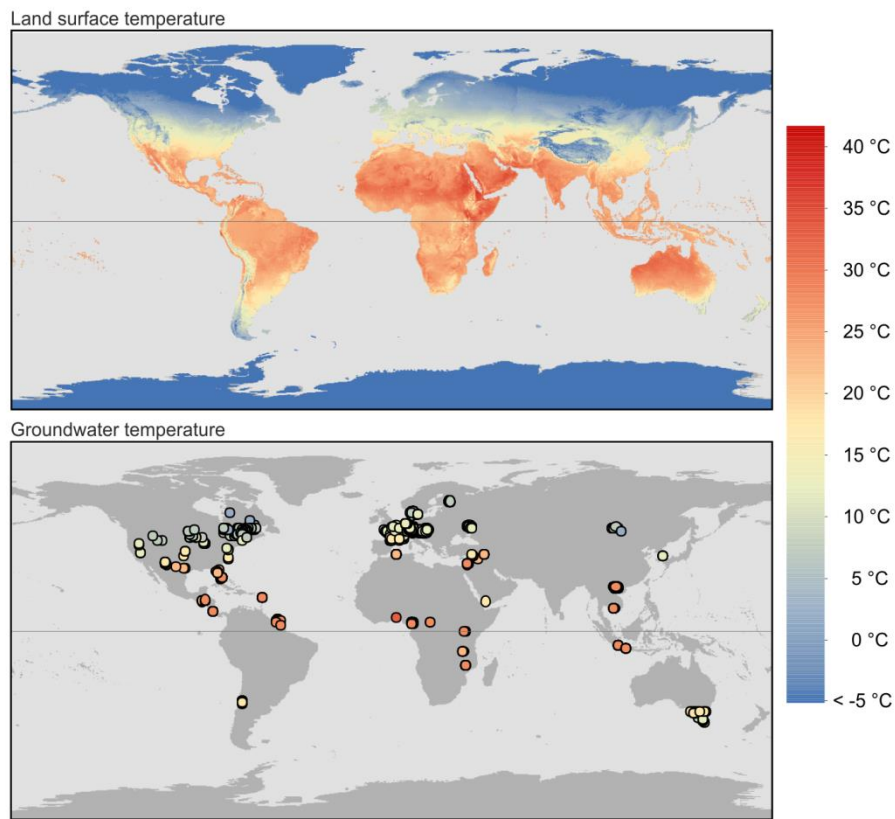


**Figure 2.1.** Global map of land surface temperature (LST) and shallow groundwater temperature (GWT). LST is given as the 10-year mean (01/2005-12/2014) of daily MODIS products MOD11A1 and MYD11A1. The bias towards cloud free days was corrected in respect to seasonal cloud cover variations. (Multi)-annual mean GWTs were collected during the same time period in a depth of down to 60 m below ground.

Overall the lowest offset is -6.1 K (LST:  $16.5^{\circ}\text{C}$ ; GWT:  $10.5^{\circ}\text{C}$ , daily measurements from 01/2013 to 05/2014) in a spring in the Black Rock Desert - High Rock Canyon Emigrant Trails National Conservation Area, Nevada, USA (Fig. S2.7b, Table S2.1). The highest offset of 11.0 K (LST:  $2.0^{\circ}\text{C}$ ; GWT:  $13^{\circ}\text{C}$ , one measurement in 06/2005 at a depth in between 21 and 40 m below ground) is measured in Erdenet, Mongolia

(Fig. S2.7c, Table S2.1). It is plausible that the high GWT is caused by the subsurface urban heat island phenomenon (36), where GWTs are raised by anthropogenically induced heat flow (86) from underground structures such as buildings or, in this specific case, the local copper-molybdenum mine (103).

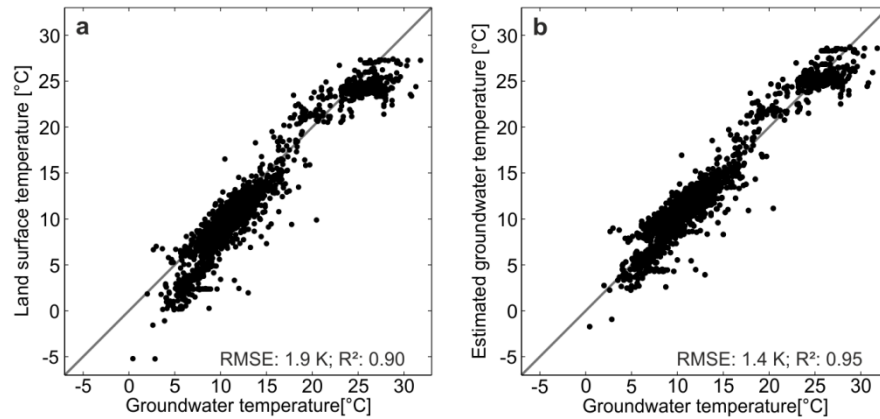


**Figure 2.2.** Relationship between a) groundwater temperature (GWT) and land surface temperature (LST) and b) estimated and measured GWT. The line of equality is given in dark grey.

Despite these extreme examples, global GWT and LST values correlate well, with a Pearson correlation coefficient of 0.97, a coefficient of determination ( $R^2$ ) of 0.90 and a root mean square error (RMSE) of 1.9 K (Fig. 2.2a). As expected, the data indicates that GWTs are elevated compared to LSTs for the coldest and warmest temperatures. These differences are caused by the two distinct effects discussed previously: in areas with lower temperatures snow cover insulates warm groundwater temperatures during the winter month raising the annual mean; in warmer and more humid areas latent heat flux caused by evapotranspiration (ET) factors into the surface energy balance, thus decreasing LSTs. Several measurement points located in moderate climate regions are affected by both factors (Fig. S2.8). Hence, the offset between GWT and LST is discussed as a superposition of an offset caused by ET and an offset caused by snow cover ( $\Delta T_{Total} = \Delta T_{ET} + \Delta T_S$ ).

### 2.3.1. Estimating Groundwater Temperatures

The influence of evapotranspiration (ET) on the offset is displayed in Fig. 2.3a. As expected, an increase in ET raises  $\Delta T_{ET}$ . However, measurement points in arid regions such as Chile, the western USA, and the Arabian Peninsula with a low ET have a negative offset, indicating colder GWTs than LSTs (Fig. S2.8a). Since the surface energy balance predicts equilibrium between the surface and subsurface temperatures in the absence of latent heat, additional local causes such as irrigation must be at play here. However, additional local studies are required to fully understand the offset between GWT and LST in these arid regions.

Fig. 2.3c and Fig. S2.8b depict the influence of surface snow cover on the offset between GWT and LST. The data shows that the percentage of snow days increases annual mean GWTs and therefore raises the offset  $\Delta T_S$ .

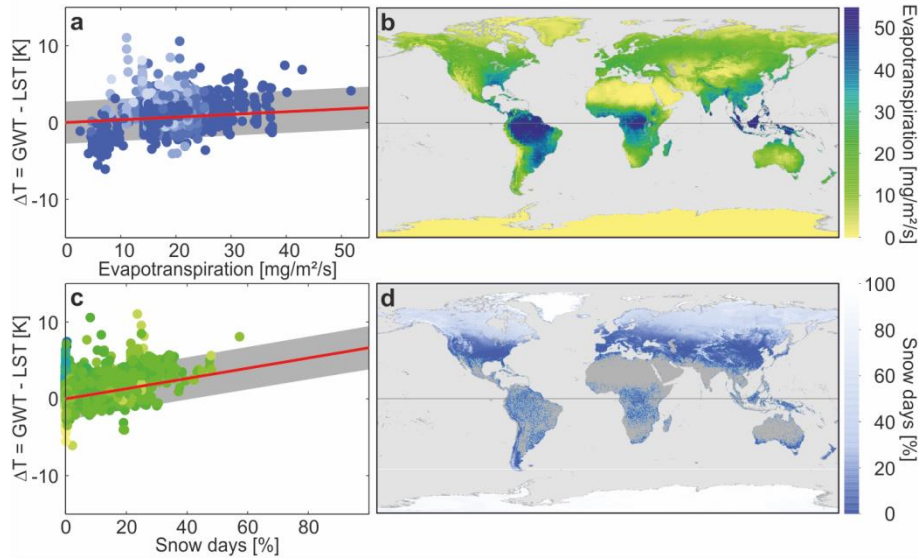


**Figure 2.3.** Evapotranspiration (ET) and snow influence the offset  $\Delta T$  between groundwater temperature (GWT) and land surface temperature (LST). a) The influence of ET on  $\Delta T$ . Color coding shows the percentage of snow days at each measurement point. The red line gives the fitted offset  $\Delta T_{ET}$ . The 95% prediction interval (for 0 % snow days) is given in grey. b) Global map of ET. c) The influence of snow on  $\Delta T$ . Color coding shows the corresponding ET. The red line gives the fitted offset  $\Delta T_S$ , in grey the 95% prediction interval (for 0 mg/m<sup>2</sup>/s ET). d) Global map of the percentage of snow days.

The best fit is obtained by the following solution:

$$\begin{aligned}
 \Delta T_{Total} &= \Delta T_{ET} + \Delta T_S \\
 &= (a \cdot ET) + (b \cdot \text{snow days}) \\
 &= (3.5 \pm 0.2) \cdot 10^4 \text{ K} \frac{\text{m}^2 \cdot \text{s}}{\text{kg}} \cdot ET \\
 &\quad + (6.6 \pm 0.3) \text{ K} \cdot \text{snow days}
 \end{aligned} \tag{1}$$

The half width of the confidence interval is given as the uncertainty. The RMSE of the fit is 1.4 K. Figs. 2.3a and 2.3c display  $\Delta T_{ET}$  and  $\Delta T_S$  separately, and a surface plot of  $\Delta T_{Total}$  is given in Fig. S2.9. This fit implies an increase in the offset of  $0.035 \pm 0.002$  K per mg/m<sup>2</sup>/s of ET and an increase of  $0.066 \pm 0.003$  K for each percent in snow days. The determined  $\Delta T_{Total}$  is added to LST to estimate GWTs for all analyzed measurement points (Fig. 2.2b, Fig. S2.10). As expected, GWTs from urban areas such as the data from Mikkeli, Finland (Table S2.1, Fig S2.11e) are severely underestimated, on average by 3.8 K, as heat flux from buildings has to be considered as well (104) for an accurate estimation. Additionally, measured GWTs in (semi-)arid regions with only minor ET,

such as the Lower Jordan Valley (Fig. S2.11b), are on average 2.3 K lower than estimated GWTs. Here irrigation is assumed to be the main source of recharge (105). In spite of these local discrepancies, estimated and measured GWT agree well. While they correlate the same as LST and GWT (Pearson correlation coefficient: 0.97),  $R^2$  increases by 0.05 to 0.95, and the RMSE (1.4 K) is improved by 0.5 K compared to the one between GWT and LST.

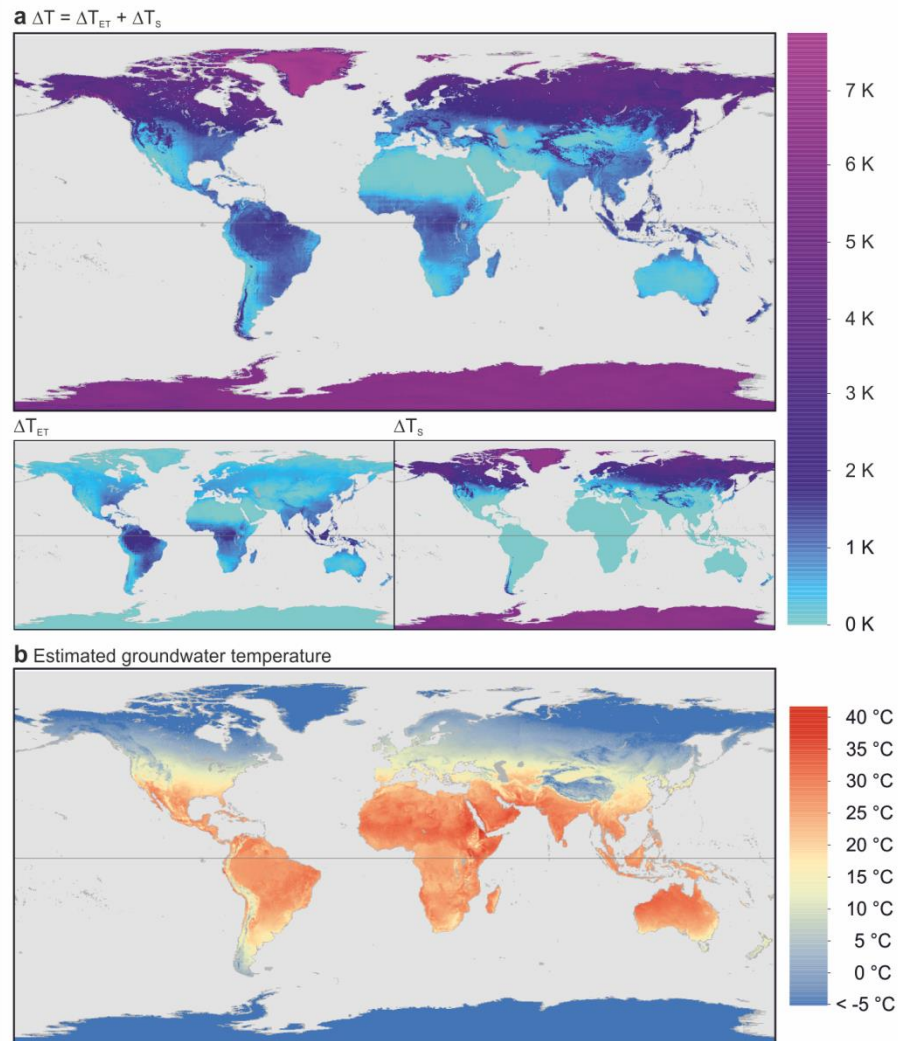


**Figure 2.4.** a) Estimated offset between land surface temperatures (LST) and shallow groundwater temperatures (GWT). b) Estimated shallow GWTs.

By applying this method to global datasets of decadal mean evapotranspiration and snow days (Figs. 2.3b and 2.3d), a global map of the expected offset was created (Fig. 2.4a). It ranges from 0 K in the arid regions such as Northern Africa, the Arabian Peninsula and central Australia to more than 6 K in the polar regions. However, with no available measurement points in such high latitudes, further research is needed to validate these findings. The average half-width of the 95 % prediction interval is  $2.76 \pm 0.03$  K

(Fig. S2.12). By adding the estimated offset to the measured LSTs, shallow global groundwater temperature is estimated (Fig. 2.4b).

## 2.4. Conclusion

The main focus of this study was on the global scale offset between 10-year mean groundwater temperatures (GWT) and satellite-derived land surface temperatures (LST). A total of 2,548 shallow GWT measurement points in 29 countries and two overseas territories are utilized to analyze the offset  $\Delta T = GWT - LST$ . We find that GWTs are warmer than LST in 83 % of all measurement points. The average offset is  $1.2 \pm 1.5$  K with highest differences between GWT and LST in both the warmest and coldest areas of Earth. These high offsets are linked to evapotranspiration, which alters the latent heat flow and therefore surface energy balance, and snow cover, which insulates warm GWTs during the winter. We are able to quantify the influence from ET and snow cover and to describe the global offset between GWT and LST as a superposition of both effects. Hence, global shallow groundwater temperatures can be estimated using only satellite-derived data. However, it is important to note that groundwater flow is not yet considered. A previous study by Benz et al. (2016) found that, on a city scale, the Pearson correlation coefficient between GWT and LST can be increased by 6 % to 10 %, if groundwater flow is scrutinized (104). Additionally, GWT anomalies caused by other regional effects such as geothermal hotspots, fossil groundwater and subsurface urban heat islands cannot be resolved with the presented method. Still, the proposed estimation technique provides shallow global GWTs with a RMSE of only 1.4 K and a coefficient of determination  $R^2$  of 0.95.

## Acknowledgements

The financial support for S. A. Benz from the German Research Foundation (DFG) under grant number BL 1015/4-1 and the Swiss National Science Foundation (SNSF) under grant number 200021L 144288 is gratefully acknowledged. Additionally we would like to thank Tanja Liesch, Anna Ender, Moritz Zemann, Julian Xanke, Tobias Kling, and Elisabeth Eiche (KIT), Erich Fischer (BMLFUW, Austria), Susanne Reimer (Tiefbauamt Karlsruhe), Michael Kramel (Geo\_t, Germany), Stefan Terzer (IAEA), Jean Michel Lemieux (Université Laval), Dr. Hussein Abed Jassas (GEOSURV, Iraq), Teppo Arola (Golder), Harold Wilson Tumwitike Mapoma (China University of Geosciences; University of Malawi), Mauricio Muñoz (Andean Geothermal Centre of Excellence, Chile), Yuliya Vystavna (O.M. Beketov National University of Urban Economy at Kharkiv, Ukraine), and Martina Maisch (LUBW, Germany) for their information and groundwater temperature data.

Input data and results (3.4 GB) are made available at <https://bwsyncandshare.kit.edu/getlink/fi8kpoehE3m5bT6ufuKY9Zh8/>.

An extensive list of all GWT sources can be found in Table S1. All Code written for Google Earth Engine is available and can be run to generate all data under the following URLs (google account needed):

LST: <https://code.earthengine.google.com/4a1bc64dbc3351a1e364490758d4cf2d>

ET: <https://code.earthengine.google.com/cf262aa371c68704c5b059d574498510>

Snow days: <https://code.earthengine.google.com/82cca1edb8f025027ef1e7b7573f16e3>



## Supplementary Material

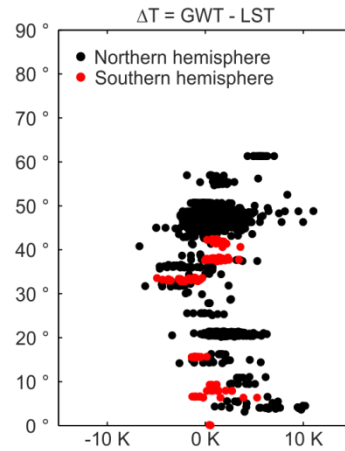


**Figure S2.1.** Offset  $\Delta T = \text{GWT} - \text{LST}$  between groundwater temperatures (GWT) and land surface temperatures (LST) depending on the latitude.

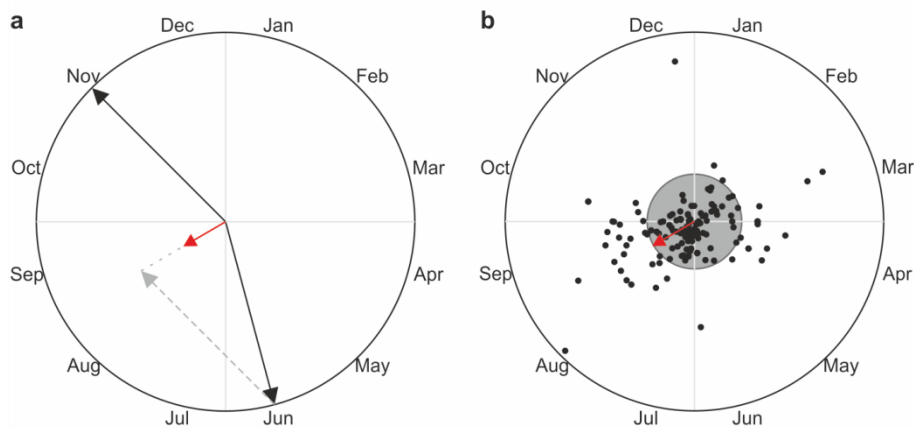


**Figure S2.2.** Determination of the seasonal radius. a) Exemplarily determination of the seasonal radius (length of the red arrow) of a single measurement point measured once in June and once in November. In this case, the seasonal radius  $r = 0.26$ . b) Seasonal radius of all analyzed measurement points in France and its overseas territories (Table S2.1) with a depth of less than 20 m. Only points within the grey circle (radius = 0.25) are considered to be bias-free regarding seasonal temperature fluctuations.

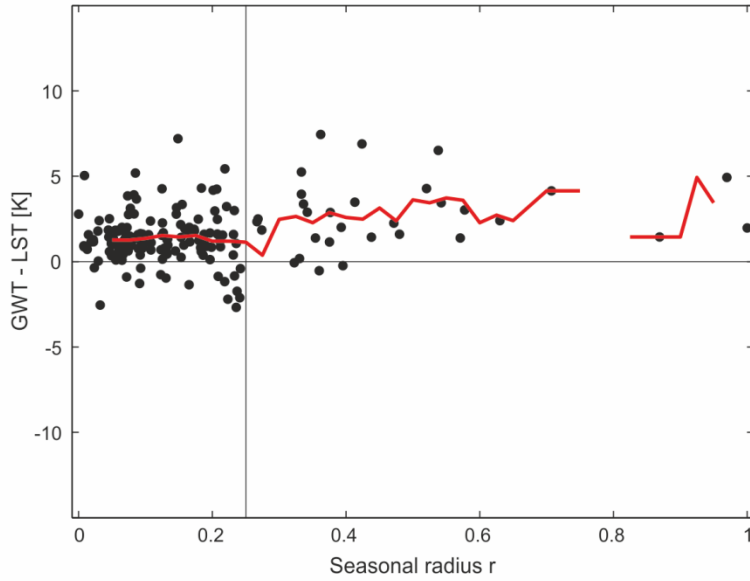


**Figure S2.3.** Influence of the seasonal radius  $r$  on the offset between groundwater temperature (GWT) and land surface temperature (LST). In black all measurement points in France and its overseas territories (Table S2.1) with a measurement depth < 20 m. The red line gives the moving average (0.05). At  $r = 0.25$  the offset is 1.1 K. In the next step to  $r = 0.275$  it jumps by more than half a Kelvin to an offset of 0.4 K. Thus, we considered all measurement points with  $r \leq 0.25$  to be bias free regarding seasonal temperature fluctuations.

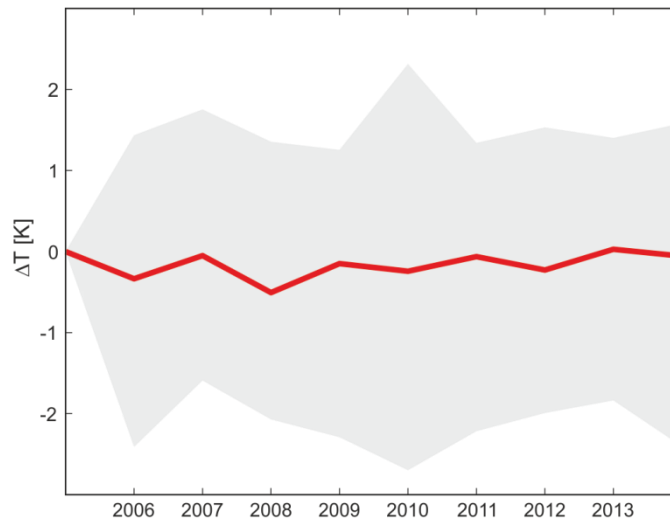


**Figure S2.4.** Change  $\Delta T$  of annual mean land surface temperature for all available MODIS pixels during the analyzed time period 2005 to 2014. Shown is in red the median temperature change (from the reference year 2005) of all analyzed pixels. The inner 90 percentiles are given in light grey. As 2005 was a particular warm year, no significant change in annual mean temperatures can be observed in this time period.

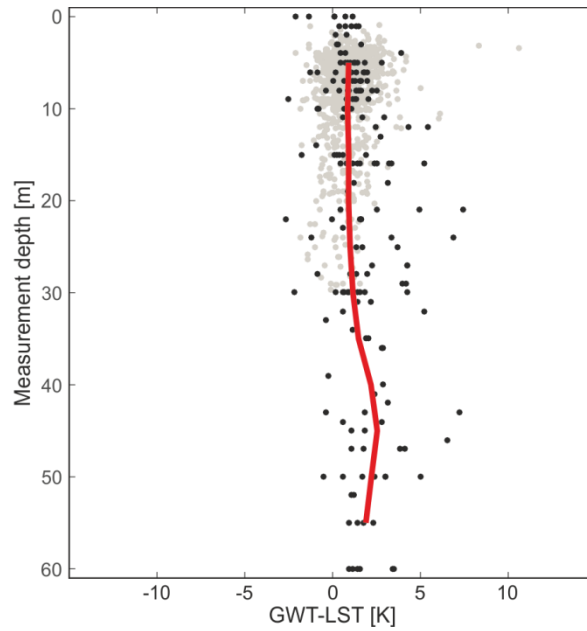


**Figure S2.5.** Influence of measurement depth on the offset between groundwater temperature (GWT) and land surface temperature (LST). All measurement points with a known measurement depth are shown. Measurement locations in France and its overseas territories are given in black, measurement locations in Austria in grey (Table S1). The red line gives the moving average (11 m). The most shallow (corresponding to 0 m - 10 m) average offset is 0.9 K, the deepest (corresponding to 50 - 60 m) average offset is 1.9 K implying a minor geothermal gradient of approximately 0.02 K/m.

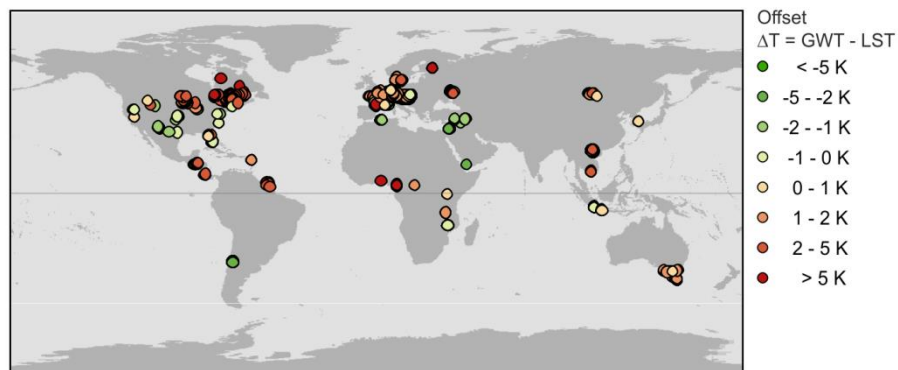


**Figure S2.6.** Offset  $\Delta T = \text{GWT} - \text{LST}$  between groundwater temperatures (GWT) and land surface temperatures (LST).

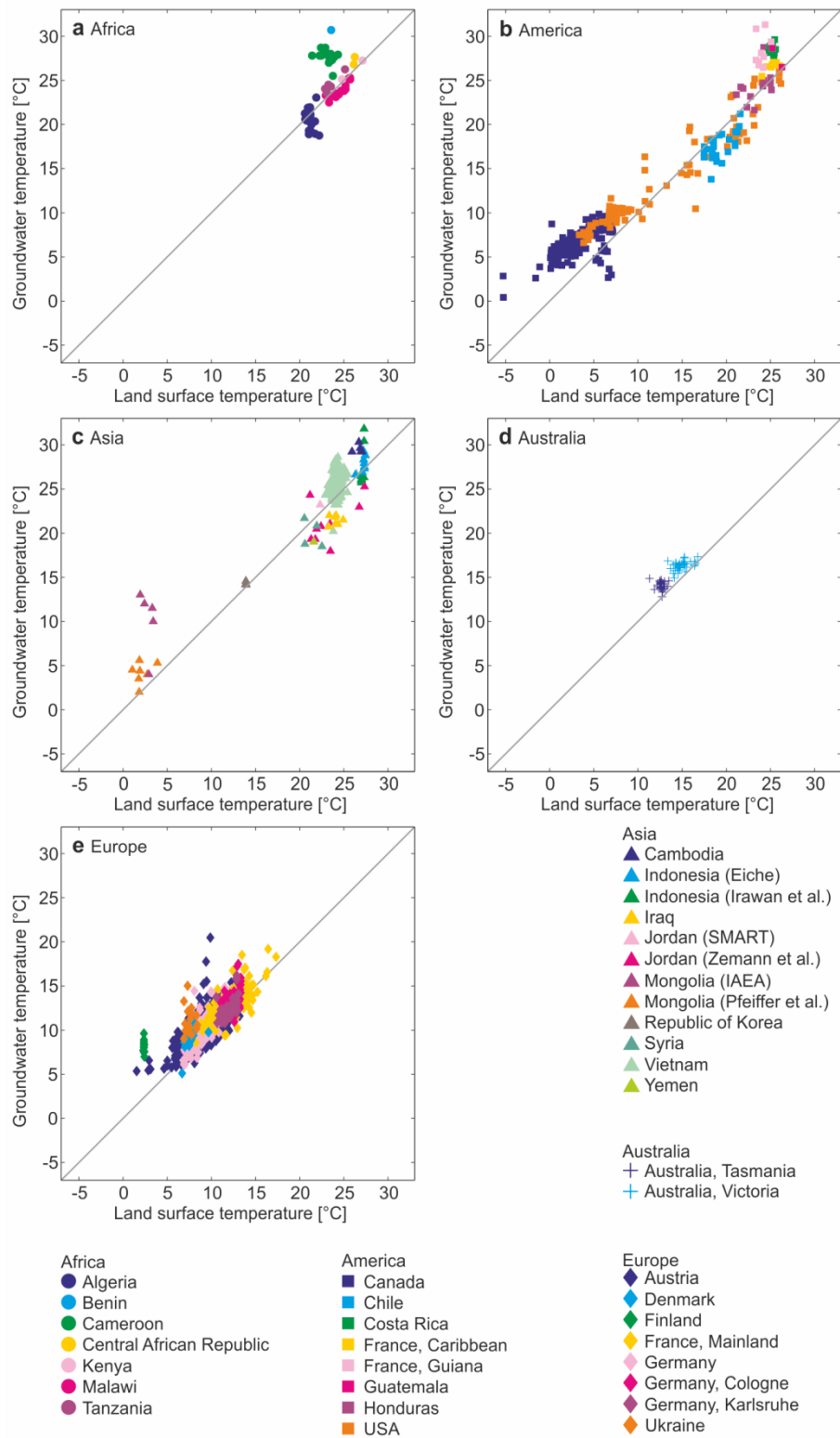


**Figure S2.7.** Relationship between land surface temperature (LST) and groundwater temperature (GWT) color coded according to the origin of the measurement points.

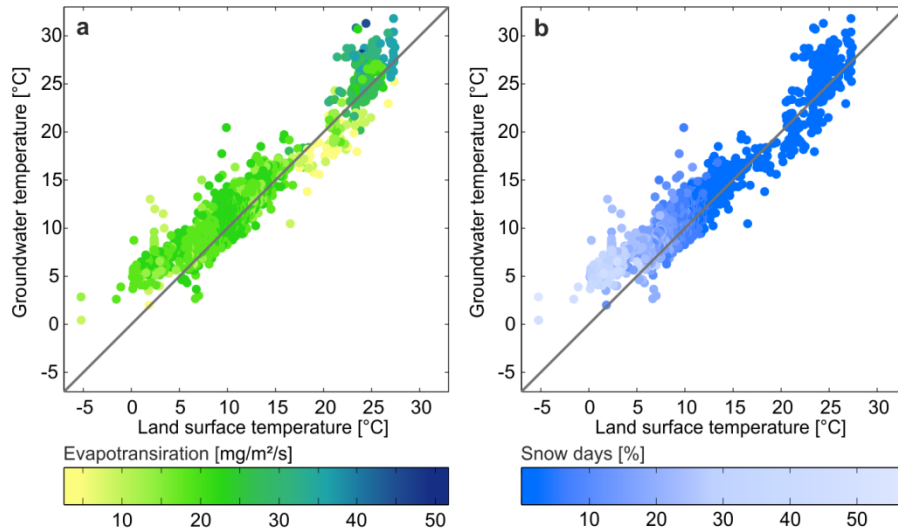


**Figure S2.8.** Relationship between land surface temperature (LST) and groundwater temperature (GWT) color coded according to a) evapotranspiration and b) snow days.

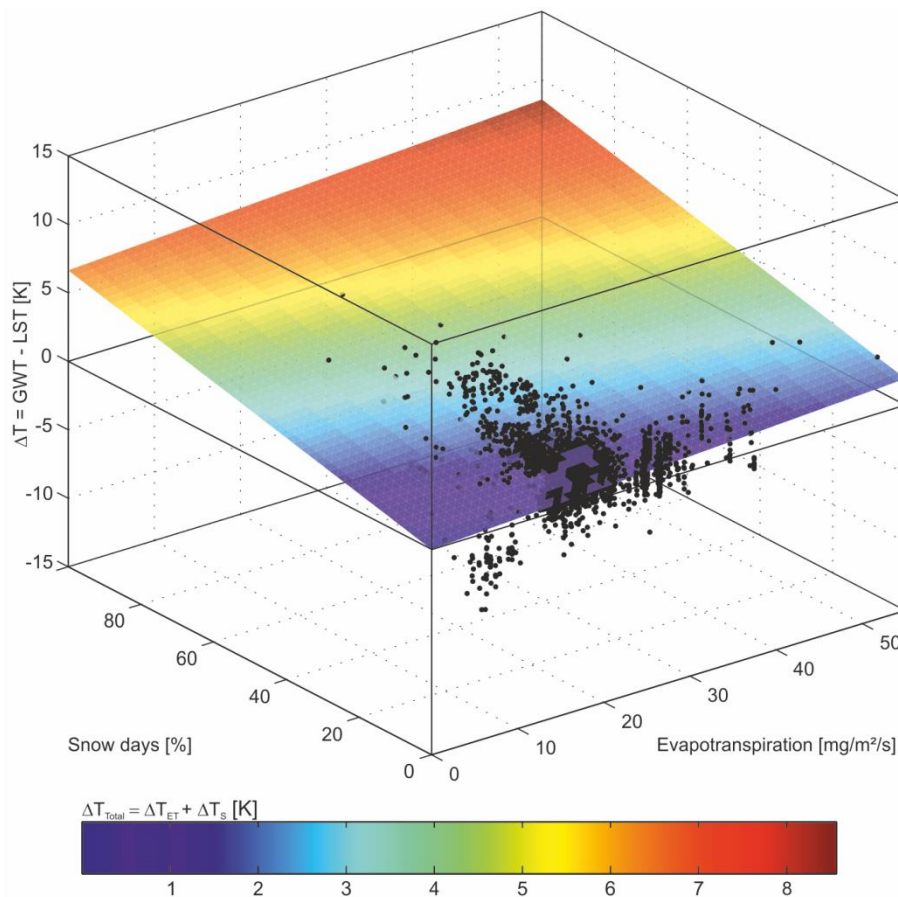


**Figure S2.9.** The influence of evapotranspiration (ET) and snow on the offset  $\Delta T$  between groundwater temperatures (GWT) and land surface temperatures (LST). The best fit  $\Delta T_{total} = \Delta T_{ET} + \Delta T_S$  is given as a surface.

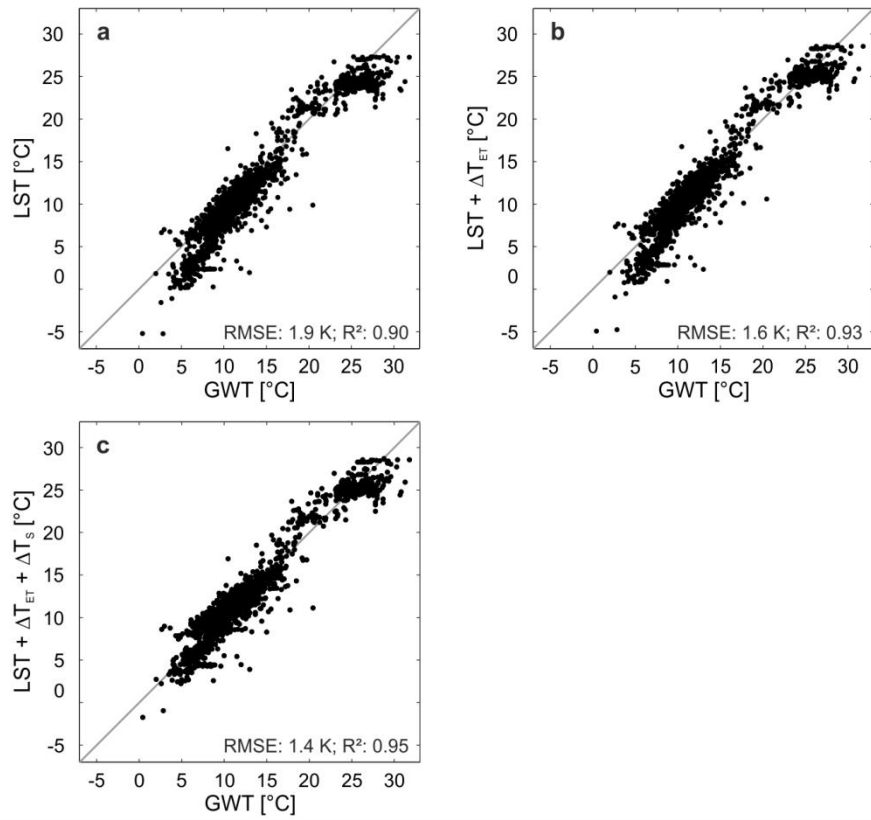


**Figure S2.10.** Comparison of a) land surface temperature (LST) and groundwater temperature (GWT), b)  $LST + \Delta T_{ET}$  and GWT, and c)  $LST + \Delta T_{ET} + \Delta T_s$  and GWT.

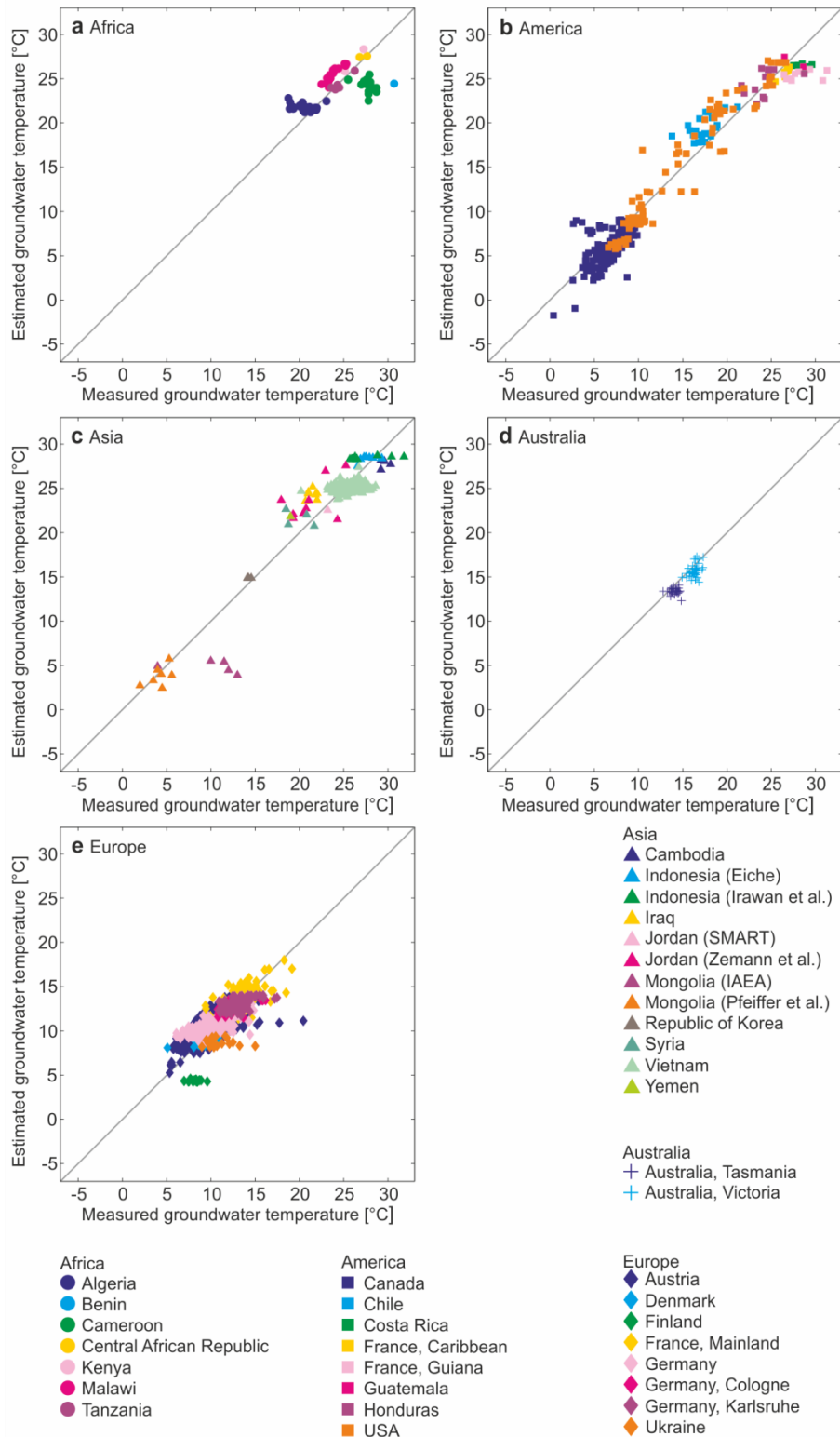


**Figure S2.11.** Comparison of estimated and measured groundwater temperatures (GWT) color coded according to the origin of the measurement points.

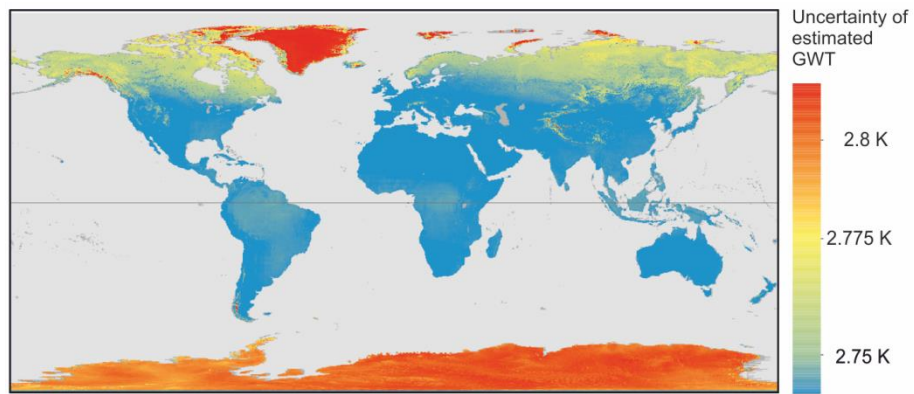


**Figure S2.12.** Uncertainty of the estimated groundwater temperature (GWT). The uncertainty is given as the half-width of the 95 % prediction interval for new observations.



**Table S2.1.** Groundwater data used in this study.

	Measurement points	Well depth	Measurement depth	Seasonal radius	Year	Source	Comment
Algeria	19	-	-	0.0	2008	Touhari et al. (2014) (106)	Raw data shows seasonal variation
Australia	25	< 30 m	-	< 0.1	2008 - 2015	Department of Primary Industries, Parks, Water and Environment (DPIPWE) (107)	Measuring interval: 15 min; measurement points in Tasmania
	35	< 30 m	-	< 0.25	2005 - 2015	Department of Environment, Land, Water & Planning (DELWP) (108)	Measurement points in Victoria
Austria	1063	-	0 - 30 m	< 0.25	2005 - 2013	Abteilung Wasserhaushalt im BMLFUW (109)	Monthly means
Benin	1	-	-	0.2	2005 - 2009	Isotope Hydrology Atlas of Africa, IAEA (110)	Raw data shows seasonal variation
Cambodia	5	< 42 m	-	1.0	2005	Buschmann et al. (2007) (111)	Water was pumped from well
Cameroon	15	21 - 59 m	-	1.0	2007	Isotope Hydrology Atlas of Africa, IAEA (110)	-
Canada, Quebec	179	-	-	< 0.2	2005 - 2015	Ministre du Développement durable, de l'Environnement et de la Lutte contre les changements climatiques (112)	Daily measurements; Temperature from top of the aquifer (0 - 45 m);
Central African Republic	2	-	-	0.0	2011 - 2012	Isotope Hydrology Atlas of Africa, IAEA (110)	Raw data shows seasonal variation
Chile	25	-	-	1.0	2014	Munoz et al. (2015) (113)	Temperature from top of the aquifer (20 - 60 m); some water was pumped from well
Costa Rica	10	-	-	0.1	2008 - 2009	Isotope Hydrology Atlas of the Americas, IAEA(110)	Raw data shows seasonal variation

	Measurement points	Well depth	Measurement depth	Seasonal radius	Year	Source	Comment
Denmark	45	< 60 m	-	-	2005 - 2015	GEUS (114)	Only median temperature given - minimum of 5 measurements
Finland	14	20-60 m	-	< 1.0	2005 - 2011	Britschgi et al.(115)	Measurement points in Mikkeli
France	127	-	0 - 60 m	< 1.0	2005 - 2015	BRGM (116)	Measurement points in Metropolitan France
	9	-	4 - 60 m	< 0.6	2005 - 2015	BRGM (116)	Measurement points in Caribbean
	9	-	20 - 60 m	0.3 - 0.7	2005 - 2015	BRGM (116)	Measurement points in French Guiana
Germany	330	0 - 30 m	0-30 m	< 0.25	2005 - 2015	LUBW (117)	Includes springs; measurement points in Baden-Württemberg
	45	-	20 m	1.0	2012	Benz et al. (2015) (86)	Measurement points in Cologne
	90	-	5 - 15 m	0.0	2011-2012	Benz et al. (2015) (86)	Daily measurements; measurement points in Karlsruhe
Guatemala	2	-	-	0.25	2007	Isotope Hydrology Atlas of the Americas, IAEA (110)	Raw data shows seasonal variation
Honduras	13	-	-	< 0.2	2005 - 2007	Isotope Hydrology Atlas of the Americas, IAEA (110)	Raw data shows seasonal variation
Indonesia	11	-	ca. 20 - 30 m	1.0	2006	Irawan et al (2015) (118)	Depth only as difference to river water level given
	9	-	0 - 30 m	< 1.0	2009-2010	Eiche (unpublished)	Includes springs
Iraq	7	-	-	1.0	2010	Jassas et al. (2015) (119,120)	Temperature from top of the aquifer (20 - 60 m)

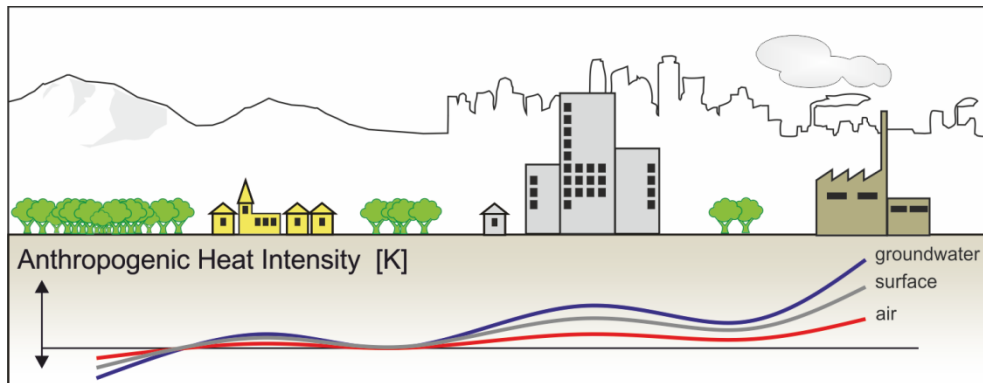
	Measurement points	Well depth	Measurement depth	Seasonal radius	Year	Source	Comment
Jordan	1	-	-	0.1	2007 - 2009	DAISY-Harvester (121)	Raw data shows seasonal variation, measuring interval: 15 min
	9	-	-	0.0	2011	Zemann et al. (2014, 2015) (105,122)	Raw data shows seasonal variations, includes springs
Kenya	2	-	-	0.2	2011 - 2013	Isotope Hydrology Atlas of Africa, IAEA (110)	Raw data shows seasonal variation
Malawi	21	< 60 m	-	1.0	2013	Mapoma et al. (2016) (123)	Water was pumped from well
Mongolia	7	< 60 m	-	1.0	2007 - 2012	Pfeiffer et al (2015) (124)	Water was pumped from well
	5	22 - 47 m	-	1.0	2005 - 2006	Isotope Hydrology Atlas of Asia, IAEA (110)	-
South Korea	4	31 - 60 m	-	1.0	2005	Isotope Hydrology Atlas of Asia, IAEA (110)	-
Syria	4	-	-	< 0.2	2005	Isotope Hydrology Atlas of Asia, IAEA (110)	Raw data shows seasonal variation
Tanzania	5	-	0 m	0.0	2005-2006	Delalande (2008) (125)	Springs
Ukraine	17	-	-	0.0	2014	Vystavna et al. (2015) (126); Yakovlev et al. (2015) (127)	Raw data shows seasonal variation
USA	95	< 30 m	-	<.25	2005 - 2015	USGS (128)	Daily mean, includes springs
Vietnam	287	< 60 m	-	1.0	2005 & 2007	Winkel et al (2010) (129)	Water was pumped from well
Yemen	1	20 m	-	1.0	2008	Alderwish et al (2011) (130)	Water was pumped from well
SUM/ AVERAGE	2,548	32 ± 16 m	11 ± 9 m	0.2 ± 0.4	2005 - 2015	-	-



### 3. Identifying Anthropogenic Anomalies in Air, Surface and Groundwater Temperatures in Germany

*Reproduced from: Benz, S. A., Bayer, P., Blum, P., Identifying anthropogenic anomalies in air, surface and groundwater temperatures in Germany. Sci. Total Environ., in press.*

#### Graphical Abstract



## Abstract

Human activity directly influences ambient air, surface and groundwater temperatures. The most prominent phenomenon is the urban heat island effect, which has been investigated particularly in large and densely populated cities. This study explores the anthropogenic impact on the thermal regime not only in selected urban areas, but on a countrywide scale for mean annual temperature datasets in Germany in three different compartments: measured surface air temperature, measured groundwater temperature, and satellite-derived land surface temperature. Taking nighttime lights as an indicator of rural areas, the anthropogenic heat intensity is introduced. It is applicable to each data set and provides the difference between measured local temperature and median rural background temperature. This concept is analogous to the well-established urban heat island intensity, but applicable to each measurement point or pixel of a large, even global, study area. For all three analyzed temperature datasets, anthropogenic heat intensity grows with increasing nighttime lights and declines with increasing vegetation, whereas population density has only minor effects. While surface anthropogenic heat intensity cannot be linked to specific land cover types in the studied resolution (1 km × 1 km) and classification system, both air and groundwater show increased heat intensities for artificial surfaces. Overall, groundwater temperature appears most vulnerable to human activity, albeit the different compartments are partially influenced through unrelated processes; unlike land surface temperature and surface air temperature, groundwater temperatures are elevated in cultivated areas as well. At the surface of Germany, the highest anthropogenic heat intensity with 4.5 K is found at an open-pit lignite mine near Jülich, followed by three large cities (Munich, Düsseldorf and Nuremberg) with annual mean anthropogenic heat intensities > 4 K. Overall, surface anthropogenic heat intensities > 0 K and therefore urban heat islands are observed in communities down to a population of 5,000.

### 3.1. Introduction

Climate and temperature are strongly affected by humans (4). The main cause of global climate change is additional greenhouse gas emission that alters the Earth's atmospheric composition (27). However, human activity also affects temperatures on a smaller, local scale. Alterations of surface cover and land use influence the ambient thermal regime (131-133), and, in most cases, cause spatial heat anomalies. These local temperature anomalies are primarily described within the bounds of large urban settlements, where urban temperatures are elevated compared to their rural surrounding and form so-called urban heat islands (UHI) (34,134). These UHIs have a tremendous impact on human life, energy consumption and the urban ecosystem (42). In France, for example, most consequences of the heat wave in August 2003 occurred in Paris, where an increase of 130% in expected mortality was observed (45). Furthermore, the cooling demand of buildings within a city center is approximately 13% higher than in similar buildings in rural areas (46). UHIs also change urban phenology: plants tend to develop up to a few weeks earlier in cities compared to their rural surrounding (48). However, with the current research mainly focusing on large city clusters, only little is known about the impact smaller communities and industrial sites have on ambient temperatures (135,136) and thus on phenology, energy consumption, and human health.

Urban heat islands can be detected in the atmosphere (37,137) (e.g. surface air temperature, SAT), at the surface (138) (land surface temperature, LST) and in the subsurface (36) (groundwater temperature, GWT). However, the interplay between these different layers is not yet fully understood. A comparison of surface and subsurface UHIs in four German cities showed that, while surface and subsurface temperatures correlate, GWTs are elevated compared to LSTs (104). This is due to multiple sources of anthropogenic heat flux into the subsurface, such as the thermal energy release from buildings and reinjection of thermal wastewater (86). UHIs in the surface and atmosphere were compared for the city of Leipzig, Germany by Schwarz et al. (2012) (139). They revealed that air temperature and LSTs are related, even so, the UHI in the air was less pronounced.

Urban heat islands are often quantified using the urban heat island intensity (UHII), which is the difference between rural background temperatures and highest urban temperatures (30). A critical component is the rural background temperature, which is not well defined yet and hence differs among presented studies (140,141). Both the MODIS Land Cover Product (34) and the ASTER land use land cover data (142) are currently used to differentiate rural areas. Some studies include elevation as an additional parameter for deriving rural background temperatures (138). In a study by Weber et al. (2014) the distance to the city center was additionally considered (143). While all of these approaches generally result in an improved understanding of urban heat islands, the variabilities of these results also prevent the comparability. Furthermore, use of non-

standard measuring equipment can significantly increase the observed urban heat island magnitudes (144) and assessing UHIs becomes rather ambiguous.

The key drivers of urban heat island intensity (UHII) are comprehensively studied (35,145,146). However, the results of these studies do not always agree. Oke (1973), for example, found that a cities' atmospheric UHII increases with its population,  $P$ . In Europe, this dependency is expressed with the following fit:  $UHII = 2.10 K \cdot \log P - 4.06 K$  ( $R^2 = 0.74$ ) (30). In contrast, Peng et al. (2012) found no evidence of population density driven surface UHII (34). They also showed only a modest correlation ( $R^2$  of 0.0 to 0.18) between surface UHII and nighttime lights. Only recently though, Zhang et al. (2014) published results indicating a correlation  $R^2$  of 0.83 to 0.85 between summer daytime surface urban heat islands and nighttime light anomalies (147). Most studies however agree on the effects of vegetation on UHII: within a park or green area, the average temperature difference to the urban surrounding is -0.94 K at the ground level (31).

In this study, the human impact on ambient temperatures is quantified for three different compartments in Germany: Air, surface and groundwater. Because above- and below-ground temperatures are influenced differently by seasonal temperature variations (148,149), we chose to analyze annual mean temperatures to ensure comparability. As a universal parameter to quantify anthropogenic heat anomalies, the anthropogenic heat intensity (AHI) is introduced. It is closely related to the UHII, but determined for each pixel (for satellite-derived LST) or measurement point (for SAT and GWT) individually, regardless of land use and location. Hence, it provides the unique and novel opportunity to a) compare the anthropogenic impact on temperatures in air, surface and subsurface, b) to find main instances of anthropogenic temperature anomalies in Germany, and c) to study the impact of smaller settlements or industrial sites on ambient temperatures.



## 3.2. Material and Methods

### 3.2.1. Material

#### Surface Air Temperature

Annual mean (2015) surface air temperature (SAT), measured 2 m above ground, was determined in 464 measurement points by taking the arithmetic mean of monthly mean values provided by the German Weather Service (Deutscher Wetter Dienst, DWD) through their Climate data center (150) (Fig. 3.1a). SAT is on average 0.26 K colder than land surface temperatures at the same location. The Pearson correlation coefficient between the two is 0.81 (Fig. S3.1).

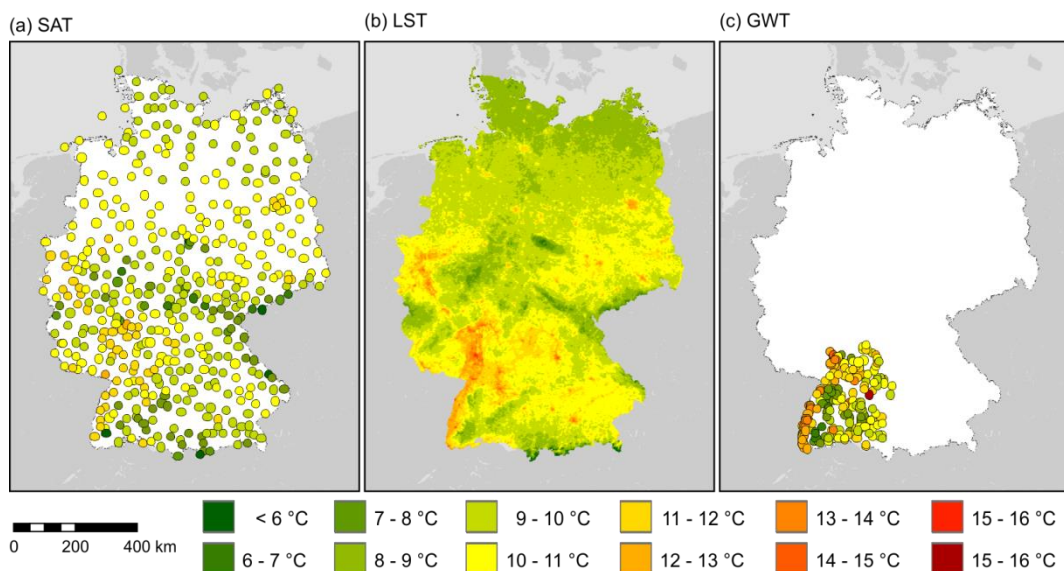


**Figure 3.1.** Mean a) surface air temperature (SAT), b) land surface temperature (LST), and c) shallow (depth  $\leq 30$  m) groundwater temperature (GWT) of Germany in 2015.

#### Land Surface Temperature

Annual mean (2015) land surface temperature (LST) was determined from level-5 MODIS daily products MOD11A1 and MYD11A1 (15), as obtained from NASA's TERRA and AQUA satellites, courtesy of the NASA Land Processes Distributed Active Archive Center (LP DAAC), USGS/Earth Resources Observation and Science (EROS) Center, Sioux Falls, South Dakota, <https://lpdaac.usgs.gov>. LST can only be determined for cloud-free days. As Germany has significantly less cloud-cover in summer than in winter, there is more LST data available for this period of the year. Following the approach by Benz et al., the annual mean was determined from monthly mean temperatures to eliminate this seasonal bias (151). This calculation was performed in

Google Earth Engine (93). The results were then exported at a resolution of approximately  $1 \text{ km} \times 1 \text{ km}$  ( $0.009^\circ \times 0.009^\circ$ ) (Fig. 3.1b).

### **Groundwater Temperature**

Groundwater temperature (GWT) data are only available for the province of Baden-Württemberg in the southwest of Germany. We determined annual mean shallow (<30 m depth) GWT in 251 measurement points (MP) for the year 2015 using data provided by the LUBW annual catalogue (Fig. 3.1c and Fig. S3.2a) (117). To ensure reliable annual mean data for each measurement point, only measurement points with a so-called seasonal radius  $r < 0.25$  were used:  $r$  is 1.0 if all measurements at the location were conducted in the same month and 0.0 if measurements were uniformly made throughout the year. A seasonal radius that is smaller than 0.25 indicates an unbiased annual mean (151). The determined GWTs are on average 0.22 K colder than LST at the same location and the Pearson correlation coefficient is 0.82 (Fig. S3.1).

### **Nighttime Lights**

Nighttime lights were compiled from Version 4 of the DMSP-OLS Nighttime Lights Time Series, Image and Data processing by NOAA's National Geophysical Data Center, and DMSP data collection by the US Air Force Weather Agency. Data were only available up to January 2014, hence 10-year mean (01/2004 – 12/2013) nighttime lights were chosen. The results were again exported at a resolution of approximately  $1 \text{ km} \times 1 \text{ km}$  (Fig. 3.2a) using Google Earth Engine (93). For Germany, the spatial median nighttime light is at DN 8 (on a scale from DN 0 to DN 63); a histogram of all data is displayed in Fig. S3.3. Fig. 3.2b shows the relationship between nighttime lights and temperatures. LST and nighttime lights correlate and show a Pearson correlation coefficient of 0.55.

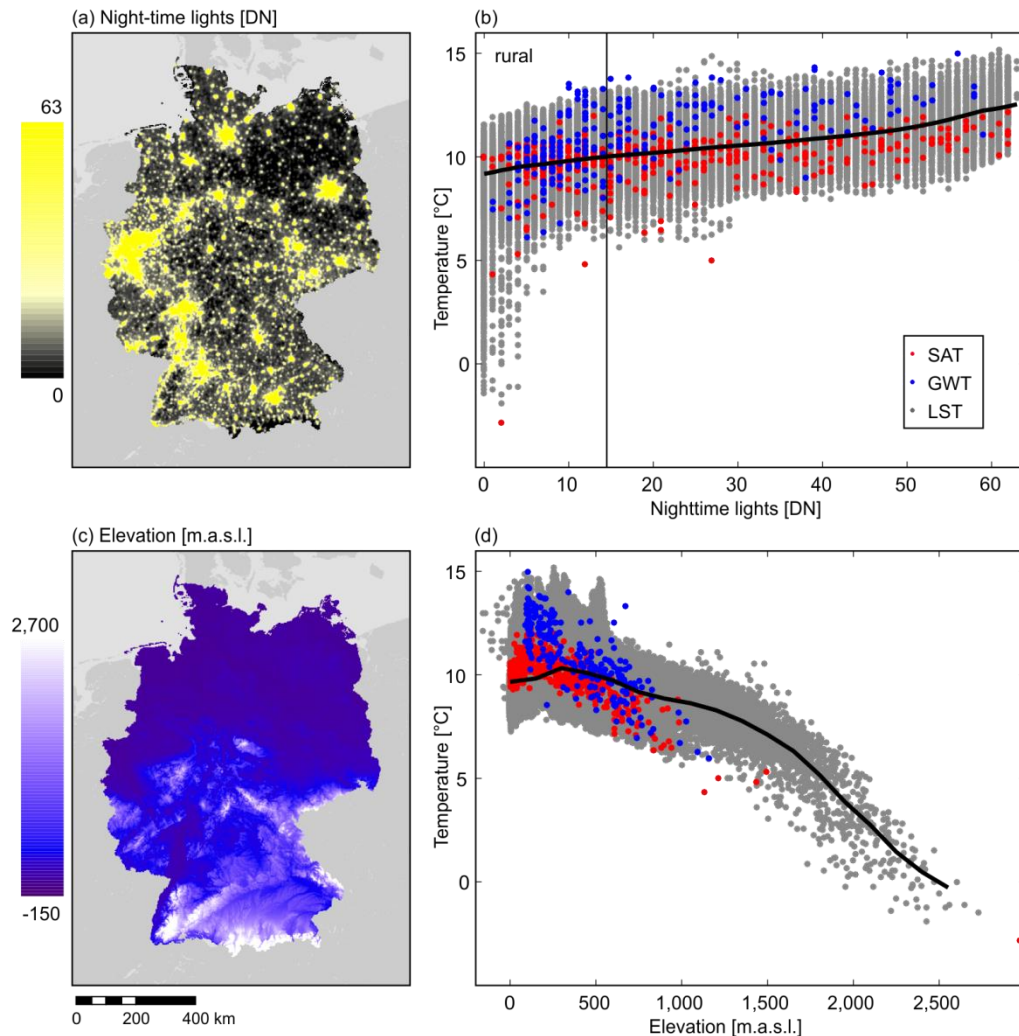
### **Elevation**

Fig. 3.2c is an elevation map of Germany. Elevation data were derived from the Global 30 Arc-Second Elevation (GTOPO30) available from the U.S. Geological Survey and downloaded using Google Earth Engine (93) with a resolution of approximately  $1 \text{ km} \times 1 \text{ km}$ . Fig. 3.2d displays the relationship between elevation and temperatures; the moving ( $\pm 150 \text{ m}$ ) average LST is given as a black line. The Pearson correlation coefficient between moving average LST and the corresponding elevation is -0.96.

### **Land Cover**

Land cover classification for entire Germany was extracted from the GlobCover (2009) Project (Fig. S3.4) (152). In this study only the three most frequent entries of the land cover classification system (LCCS) are considered: A11 - Cultivated terrestrial areas and

managed lands; A12 - Natural and semi-natural terrestrial vegetation; and B15 - Artificial surfaces. Together they cover more than 98% of the entire analyzed area. Figure S3.5 shows the influence of land cover on temperatures. Only minor differences (approximately 0.1 K) in mean LST are observed for the different LCCS entries.



**Figure 3.2.** Influence of anthropogenic nighttime lights and elevation on land surface temperature (LST), surface air temperature (SAT), and groundwater temperature (GWT). The moving average LST is depicted in black in b) and d).

### Enhanced Vegetation Index

The enhanced vegetation index (EVI) is taken from MODIS product Version-5 MYD13A1 by courtesy of the NASA Land Processes Distributed Active Archive Center (LP DAAC), USGS/Earth Resources Observation and Science (EROS) Center, Sioux Falls, South Dakota. The annual mean (2015) EVI was determined in Google Earth Engine (93) and exported with a resolution of approximately 1 km × 1 km (Fig. S3.6a). The Pearson correlation coefficient between LST and EVI is -0.22 (Fig. S3.6b).

## Population Data

Population data were provided by the Federal Statistical Office of Germany and represents numbers acquired via a census conducted in 2011. In this study, we used both the spatial distribution of population density provided as a  $1 \text{ km} \times 1 \text{ km}$  dataset by the census database (Statistisches Bundesamt, Zensusdatenbank) (153) (Fig. S3.6c), and the total population of local communities available through Germany's Regional Database (Statistisches Bundesamt, Regionaldatenbank) (154). No correlation between population density and LST exists (Pearson correlation coefficient: 0.02, Fig. S3.6d).

### 3.2.2. Method

To analyze the anthropogenic influence on temperature, we introduce the anthropogenic heat intensity (AHI). It can be applied to a broad variety of different temperature measurements such as GWT, LST, and SAT. Following the commonly used definition of urban heat island intensity (UHII: max. urban temperature - rural background temperature) (30), AHI is determined by subtracting median rural background temperatures ( $T_r$ ) from individual temperatures ( $T$ ) recorded at each measurement point (GWT and SAT) or pixel (LST):

$$AHI = T - \text{median}(T_r) \quad (1)$$

While urban land cover and land use classifications are often used to analyze the spatial properties of city-scale urban heat islands (155,156), they are not commonly available for such large-scale studies such as this one. Hence, nighttime light was used as an indicator for rural areas, while elevation and distance to the analyzed pixel or measurement point were considered to find appropriate background measurement locations.

### Rural Background Temperature

Nighttime lights have been intensively discussed as an indicator of urban activity (41,157,158). In general, the higher the recorded digital number (DN), the more urban activity is present. This dependency is also visible in the correlation between nighttime lights and temperature (Fig. 3.2b). To define the area used for the determination of  $T_r$ , an upper limit of 'rural' nighttime light has to be set. The method itself is not sensitive regarding the precise value of this upper limit (Fig. S3.7). The difference in median land surface AHI calculated with an upper limit at  $DN < 10$  and  $DN < 20$  is merely 0.04 K and can therefore be disregarded. Subsequently DN 15 was chosen as the upper limit of allowed nighttime light, because it is both the 75<sup>th</sup> percentile for nighttime light (Fig. S3.3) and the first inflection point in the nighttime light – temperature plot (Fig. 3.2b). Hence, only areas with  $DN < 15$  were considered rural and used to determine  $T_r$ . At this number,

average LST has increased by 0.8 K from the temperatures at DN 0. In comparison, the difference in average LST between minimal and maximal nighttime lights is 3.4 K.

As temperature decreases significantly with elevation (Fig. 3.2d), this parameter has to be considered for delineating the background area. As LST increases by 0.8 K from rural nighttime light at DN 0 to DN 15, this value was also chosen as the endorsed change in temperature due to elevation change. Fig. 3.2d shows the moving ( $\pm 150$  m) average LST. On average, it decreases by 0.004 K/m with a maximal decrease of 0.009 K/m at 1,800 m above sea level. Thus, a change in elevation of  $\pm 90$  m will result in a temperature change of 0.8 K at most. Hence, we only consider data with an elevation  $\pm 90$  m compared to the analyzed measurement point or pixel.

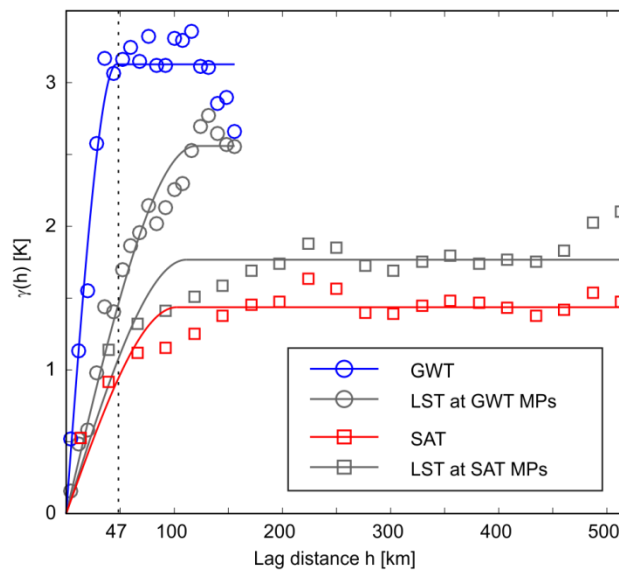


**Figure 3.3.** (Semi-)Variogram of all analyzed temperatures. Sill and range are displayed in Table S1. MPs: measurement points.

Variograms of SAT, GWT and LST were set up to determine an appropriate distance between background temperature and analyzed location (Fig. 3.3). Fitting of the theoretical variograms was performed in MATLAB R2016a using a least square fit with the spherical model, without a nugget. Resulting values for sill and range are shown in Table S3.1. Since two variograms for LST data (one created from LST at GWT measurement locations and one created from LST at SAT measurement locations) are analyzed, it becomes apparent that sill values depend on the measurement point location. The fitted range, however, is not influenced by measurement point location. It is lowest for GWTs with 47 km. Hence, we chose 47 km as the maximal distance between the analyzed location and the background temperature measurements.

In summary, for the determination of the median rural background temperature  $T_r$  of a specific location, only temperature measurements are considered, which a) are within 47

km of the analyzed location, b) have a nighttime light lower than DN 15, and c) are elevated  $\pm 90$  m compared to the analyzed location. To ensure a statistically meaningful median  $T_r$ , AHI was only determined for measurements with five or more rural background measurement points for SAT and GWT, or 50 or more valid rural background pixels for satellite-derived LST.

The introduced method can be applied to any available temperature datasets, from city-scale to global-scale, regardless of the studied compartment (e.g. air, surface or groundwater). To determine whether measurement point location influences the AHI results, we compared surface AHI derived from all pixels with those derived using only data at the GWT and SAT measurement locations (Fig. S3.8). For both, GWT and SAT measurement points, the RMSE between pixel based and measurement point based AHI is 0.3 K and neglected within this study. Thus, AHIs in different compartments are compared without considering any sampling bias.

### 3.3. Results and Discussion

Figure 3.4 shows the anthropogenic heat intensity (AHI) of Germany in air and surface and the AHI of the province of Baden-Württemberg in groundwater. Results are also made available in the supplementary material. In the following, we briefly discuss the AHI values in air and groundwater and compare them to surface AHI results. As there is much more LST data (~440,000 Pixels) examined than SAT (195 analyzed measurement points) and GWT (186 analyzed measurement points) data, only surface AHI is discussed in detail.

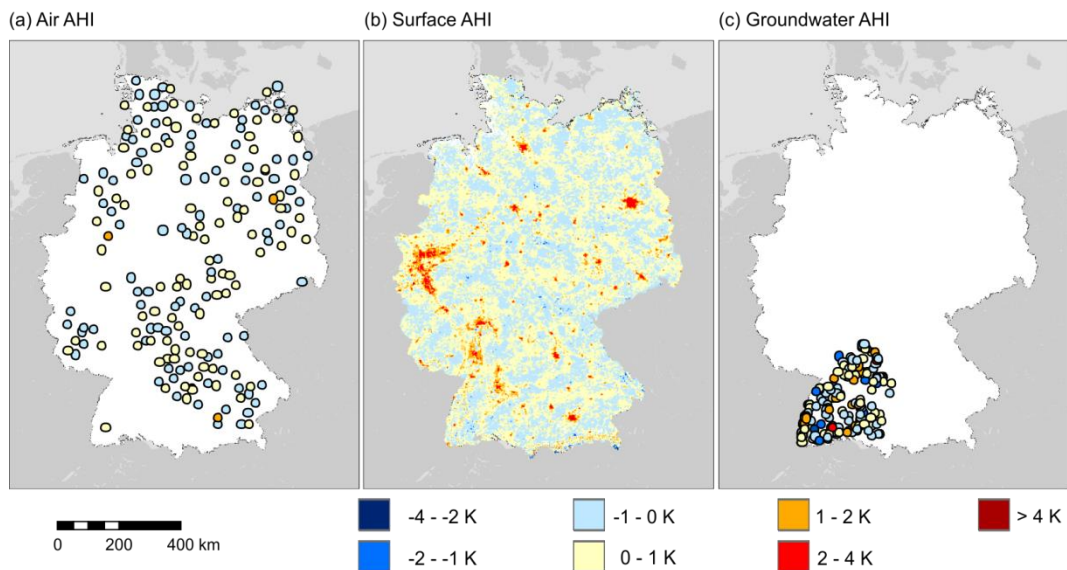


**Figure 3.4.** Anthropogenic heat intensities (AHI) of Germany in (a) air, (b) surface and (c) groundwater.

#### 3.3.1. Air Anthropogenic Heat Intensity

The air AHI ranges from -0.7 K next to a forest in a low mountain range (Swabian Jura) to more than 1.1 K in three weather stations near Berlin, near Munich, and near the Ruhr city cluster (Fig. 3.4a, histogram in Fig. S3.9a). The Pearson correlation coefficient between air and surface AHI is 0.63. The RMSE is 0.5 K and therefore only slightly larger than the expected sampling-location bias of 0.3 K (Fig. 3.5). Still, the comparison indicates that air temperature shows less anthropogenic warming than surface temperature and therefore confirms the results by Schwarz et al. (2012) (139). However, no definite conclusion can be made with the limited number of measurement points. The influence of land cover on the AHI in the air is displayed in Fig. 3.6. As expected measurement points in areas classified as ‘Artificial surfaces’ show the highest heat anomaly with a mean air AHI of  $0.5 \pm 0.5$  K (uncertainties are given in form of the standard deviation).



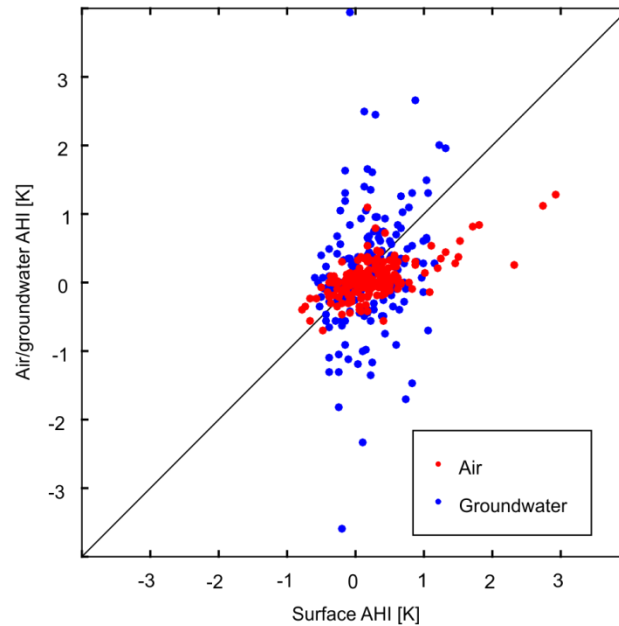


**Figure 3.5.** Comparison of the anthropogenic heat intensities (AHI) of GWT and LST and of SAT and LST.

### 3.3.2. Groundwater Anthropogenic Heat Intensity

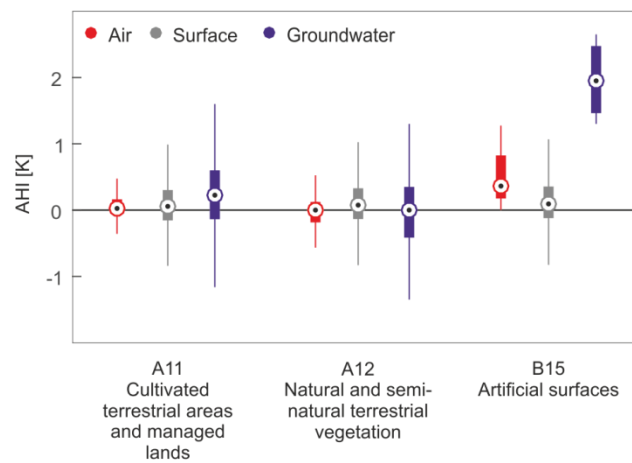
Groundwater AHIs are displayed in Fig. 3.4c and Fig. S3.2b, a histogram is given in Fig. S3.9c. As expected from the high sill and low range in the (semi-)variogram (Fig. 3.3), AHI in the groundwater has a much broader range than at the surface (Fig. 3.5). While the RMSE between surface and subsurface AHI is 0.8 K, differences between these two range from -3 to 4 K and both parameters do not correlate (Pearson correlation coefficient: 0.27). Because temperatures themselves correlate well (Fig. S3.1), this indicates that humans impact groundwater and surface partially through unrelated processes. GWT, for example, is significantly altered by the use of shallow geothermal energy systems such as groundwater heat pumps (69) as well as reinjection of thermal waste water and subsurface infrastructure such as basements, district heating networks, sewage systems and buried cable systems (36,86,159)).

Fig. 3.6 shows the influence of land cover on GWT anomalies. Groundwater under artificial surfaces displays the highest anthropogenic heat intensity with a mean value of  $2.0 \pm 0.7$  K. Again, the human impact on temperatures appears to be more prominent in GWT than in LST, verifying previous observations for UHIs (104,160). In contrast to SAT and LST, GWTs under cultivated terrestrial areas and managed lands appear to be slightly elevated, on average by  $0.2 \pm 0.8$  K. While the main cause of these anomalies has to be validated yet, they are possibly linked to irrigation with warmer surface water causing advective heat transport into the aquifer.



### 3.3.3. Surface Anthropogenic Heat Intensity

Surface AHI is shown in Fig. 3.4b. Mean AHI is  $0.1 \pm 0.5$  K; minimum AHI is  $-4.3$  K found in a mountain range of the Northern Limestone Alps within the Berchtesgaden National Park. A histogram is provided in Figure S3.9b. The locations of the top 50 maximum surface AHI of Germany are displayed in Table S3.2. The pixel with the highest annual mean surface AHI (4.5 K) is not found in a city, but over an open-pit lignite mine near Jülich. This extreme temperature anomaly is possibly caused by the immense land cover changes resulting in an open-pit with a depth of approximately 370 m and without vegetation. However, further research is necessary to fully understand temperature anomalies at open pit mines. Pixels with the next highest surface AHIs are located in large cities, namely Munich, Düsseldorf, and Nuremberg, with AHIs of more than 4 K. The UHI of Munich was studied in 1982, when Brundl and Hoppe (1984) (161) determined a 17% higher consumption of heating energy for the outskirts of the city compared to the city center. The surface UHI was quantified by Pongracz et al. (2010) (138). They found an annual mean nighttime UHII of approximately 1.7 K, while daytime UHII spanned from 0 K in December to 5 K in June. These comparably low values are due to the chosen background temperature: A large part of the background area used by Pongracz et al. (2010) is classified as non-rural in our analysis and therefore not used here



**Figure 3.6.** Influence of land cover on the anthropogenic heat intensity (AHI) in air, surface and groundwater. The dots in the boxplot indicate median values, the bars correspond to the inner quartile range (IQR) ranging from the 25<sup>th</sup> percentile ( $p_{25}$ ) to the 75<sup>th</sup> percentile ( $p_{75}$ ). Whiskers span from the lowest value higher than  $p_{25} - 1.5 \cdot IQR$  to the highest value lower than  $p_{75} + 1.5 \cdot IQR$ .

The top 15 surface AHI locations also include pixels in smaller cities (e.g. Wolfsburg: surface AHI of 3.7 K, 120,000 residents; Saarlouis: surface AHI of 3.4 K, 40,000 residents) known for their industrial sites. This indicates that not only urban heat islands exist, but also industrial heat islands. Furthermore, as our method is applied to all areas including rural ones, we find naturally occurring heat islands as well: there are four

locations in the alpine mountains among the top 50 surface AHI locations. Here, the south facing slopes of the high altitude mountain ranges receive more solar radiation and are considerably warmer ( $> 2$  K) than the north-facing slopes.

Unlike AHI in groundwater and air, surface AHI cannot solely be linked to artificial surfaces (Fig. 3.6) using the analyzed classification system (GlobCover, 2009) (152) and resolution (approximately  $1 \text{ km} \times 1 \text{ km}$ ). However, a more detailed case study of the surface UHI of Shanghai revealed differences in temperature of up to 1.6 K between different urban land use and land cover categories (162).

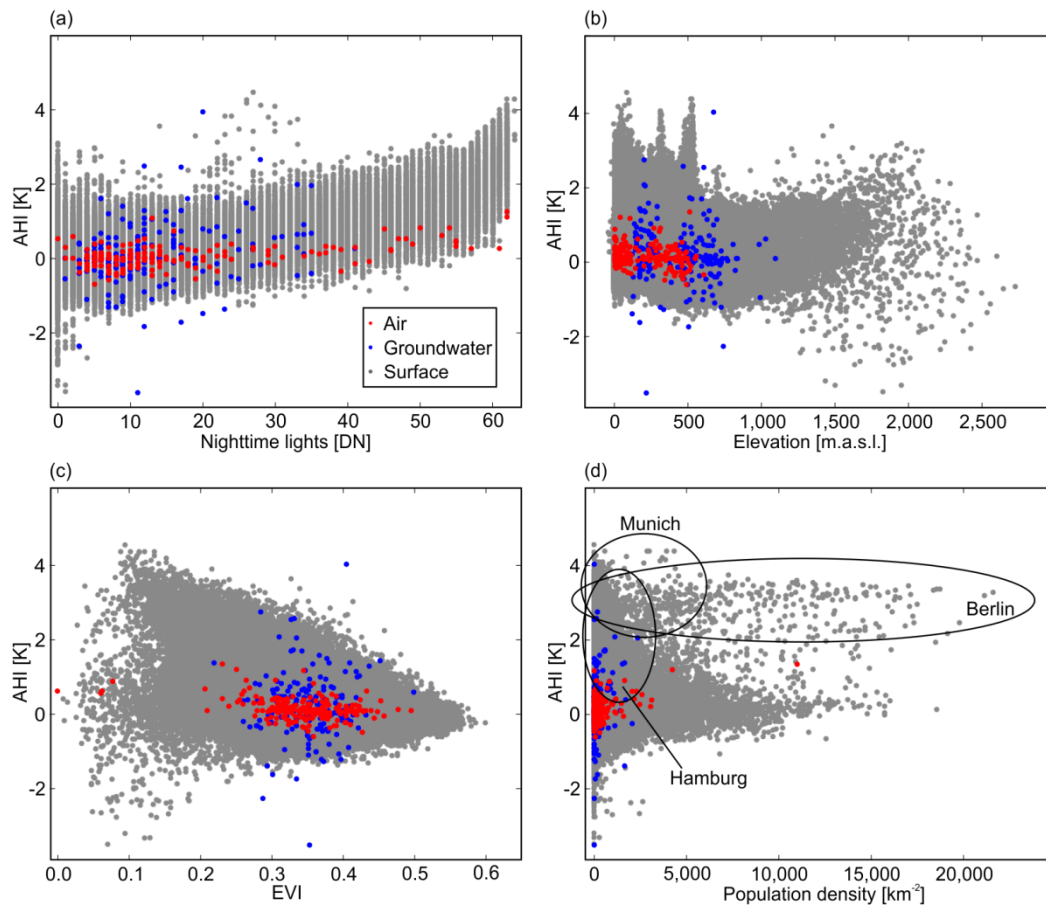


**Figure 3.7.** Influence of nighttime lights, elevation, enhanced vegetation index (EVI), and population density on the anthropogenic heat intensity (AHI) in air, surface and groundwater.

### Main Drivers of Surface AHI

To determine the main drivers of surface AHI, nighttime lights, elevation, vegetation (enhanced vegetation index, EVI), and population density were analyzed (Fig. 3.7). Following the trend observed in temperatures (Fig. 3.2b), AHI rises with increasing nighttime lights (Fig. 3.7a). The Pearson correlation coefficient  $\rho$  between surface AHI and nighttime lights is 0.71. Fig. 3.7b displays the correlation between elevation and surface AHI ( $\rho = -0.12$ ). Because our method considers elevation for the determination of

the median rural background temperatures, no clear trend is visible in contrast to the temperature/elevation plot (Fig. 3.2d). However, highest AHI are still observed in lower altitudes, where cities are commonly located. For higher altitudes, AHI variance increases; this is mainly due to the difference in solar radiation on opposite facing slopes of a single mountain range.

In Fig. 3.7c the enhanced vegetation index (EVI) and surface AHI are compared. While no clear linear correlation is observed (Pearson correlation coefficient: -0.36, Fig. 3.7c), our results indicate that vegetation decreases the upper limit of surface AHI. This further validates the observations made by several studies on the cooling effect of vegetation on urban temperatures (163-165).

Pearson correlation coefficient of 0.06 illustrates that the population density per pixel is no indication for AHI (Fig. 3.7d). While pixels in large cities such as Berlin (3.3 million residents), Hamburg (1.7 million residents), and Munich (1.3 million residents) show increased AHI, highest heat intensities are not necessarily found in areas with a high population density. Thus, the established correlation between city population and urban heat island intensity by Oke (1973) (30) cannot be transferred to a pixel-based analysis. However, the maximum AHI ( $AHI_{max}$ ) within a city can be linked to its urban heat island intensity (UHII) and is thus expected to depend on the total population of each city.

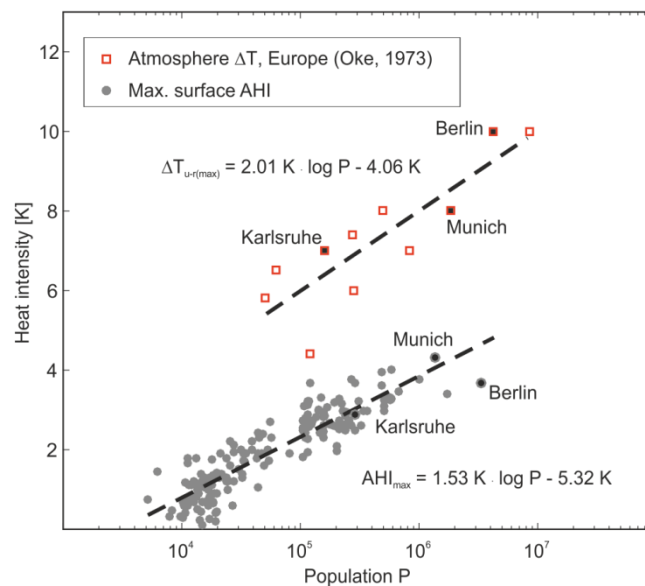


**Figure 3.8.** Influence of population on the maximum surface AHI of a settlement.

To test this hypothesis, the  $AHI_{max}$  of all German cities with a population of more than 100,000, as well as 100 randomly chosen smaller communities (> 5,000 residents), were compared to the population of the corresponding municipality (Fig. 3.8). Since Oke (1973)

(30) analyzed single summer temperature measurements during the day, when UHII is warmest (40), our annual mean temperatures result in lower heat intensities. For the three cities analyzed in both studies, this difference is on average 4.4 K (Berlin: summer day UHII of 10.0 K, annual mean surface AHI 3.7 K; Munich: summer day UHII of 7.0 K, annual mean surface AHI 4.3 K; Karlsruhe: summer day UHII of 7.0 K, annual mean surface AHI 2.9 K).

Still, our results confirm that  $AHI_{max}$  similar to UHII can be related to population ( $P$ ) and follows the model predicted by Oke even for smaller city sizes with a RMSE of 0.4 K:

$$AHI_{max} = 1.53 K \cdot \log(P) - 5.32 K \quad (2)$$

By extrapolating the fit, we can further assume that  $AHI_{max}$  remains positive for communities with a population of more than 3,000. The smallest studied community, Amöneburg located in the region of Middle Hesse, has a population of 5,010 and an observed  $AHI_{max}$  of 0.74 K.

### 3.4. Summary and Conclusion

This study analyzes the anthropogenic impact on recorded annual mean temperatures of three different compartments: surface air temperatures (SAT), land surface temperatures (LST), and groundwater temperatures (GWT). The anthropogenic heat intensity (AHI) is introduced as a universal parameter that represents the difference between local temperature  $T$  and median rural background temperature  $T_r$  for each analyzed measurement location (GWT and SAT) or pixel (LST), on a large, in this case countrywide, scale.

Comparing AHIs in air, surface and subsurface for the case of Germany, we found that GWTs are impacted the most by human activity. Although no measurements within cities were analyzed, determined groundwater AHI ranges from -4 K to +4 K. At the same locations, surface AHI ranges from -1 K to +1 K. However, further research is necessary to fully understand the main causes of elevated GWTs under non-urban, cultivated lands.

At the surface, main instances of anthropogenic temperature anomalies were identified. While most of the top 50 pixels with the highest AHIs in Germany are located within cities, maximum surface AHI is found over an open-pit lignite mine. Additionally, many of these top 50 pixels are located in smaller cities known for their industrial sites, hinting to the industrial sector as a significant driver of urban heat islands. Accordingly no correlation between population density and AHI could be found.

The impact of smaller settlements on temperatures was analyzed at the example of 100 randomly chosen communities (5,000 to 100,000 residents). Our results indicate AHI of approximately 0.3 K for the smallest analyzed communities. However, further studies using different timescales and spatial resolutions are necessary to scrutinize the impact that smaller settlements have on ambient air, ground and groundwater temperatures.

Finally, AHIs of other regions or countries must be compared to determine spatial consistency and to reveal large scale trends. As LST is available for the whole planet, future work should also analyze a global dataset. Studying the differences in daytime and nighttime surface AHI as well as its annual variation will help to classify surface urban heat islands and thus contribute to the development of appropriate mitigation strategies.

## **Acknowledgment**

The financial support for S. Benz from the German Research Foundation (DFG) under grant number BL 1015/4-1 and the Swiss National Science Foundation (SNF) under grant number 200021L 144288 is gratefully acknowledged. Furthermore, we would like to thank Tanja Liesch (KIT) and Martina Maisch (LUBW) for sharing information on groundwater temperature data, and Anja Hardel and Sven Bäumer (Statistisches Bundesamt, Zensus 2011) for sharing information on the population density of Germany. Finally, we would like to thank the two anonymous reviewers for their comments.

## Supplementary Material

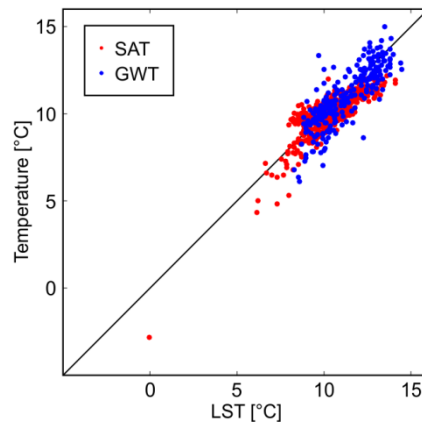


**Figure S3.1.** Relationship of land surface temperature (LST) and both surface air temperature (SAT) and groundwater temperature (GWT).

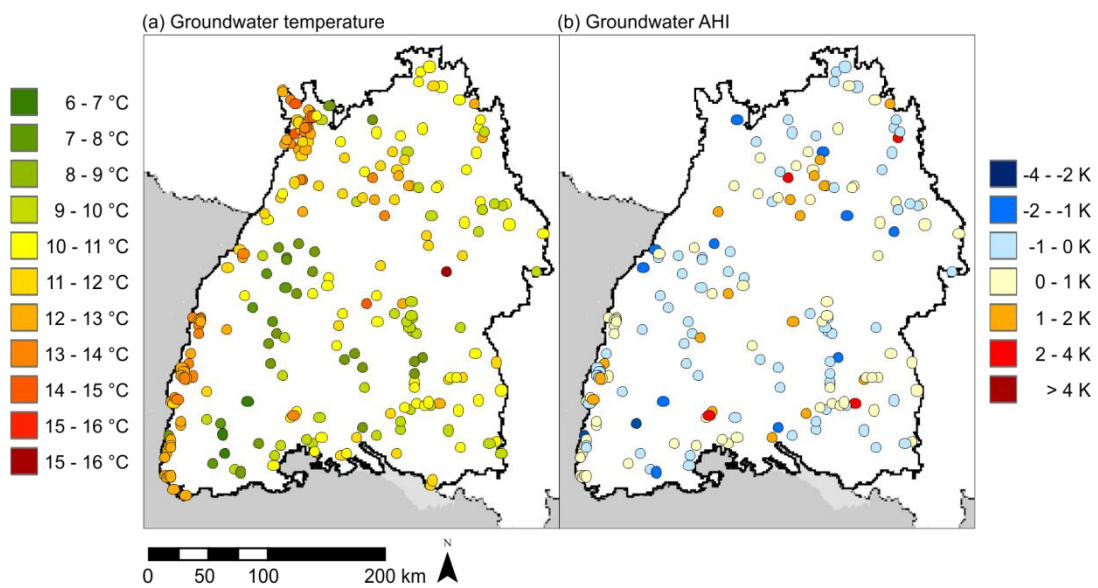


**Figure S3.2.** (a) Annual mean groundwater temperature and (b) annual mean groundwater anthropogenic heat intensity (AHI) of Baden-Württemberg, Germany, 2015.

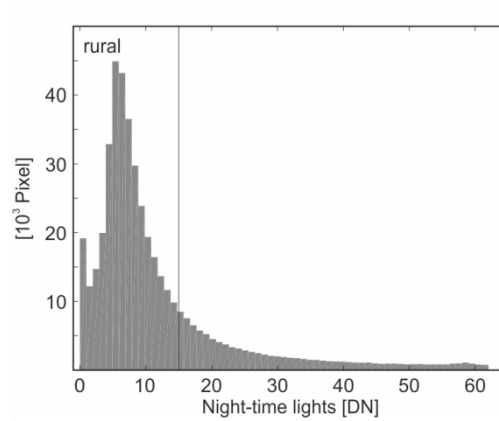


**Figure S3.3.** Histogram of nighttime lights in Germany. All areas with a nighttime light of less than DN15 were considered rural.

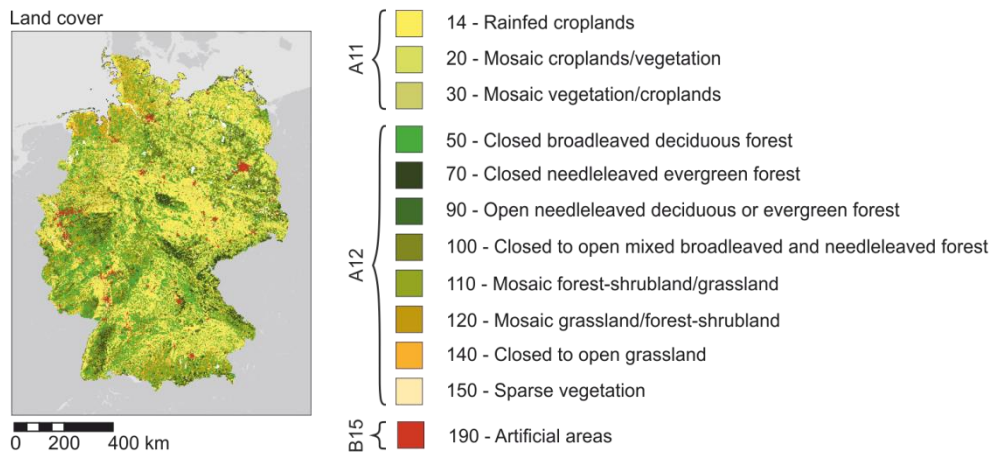


**Figure S3.4.** Land cover map of Germany. The shown data is extracted from the GlobCover 2009 global land cover map processed by ESA and the Université Catholique de Louvain. All data is made available at [http://due.esrin.esa.int/page\\_globcover.php](http://due.esrin.esa.int/page_globcover.php).



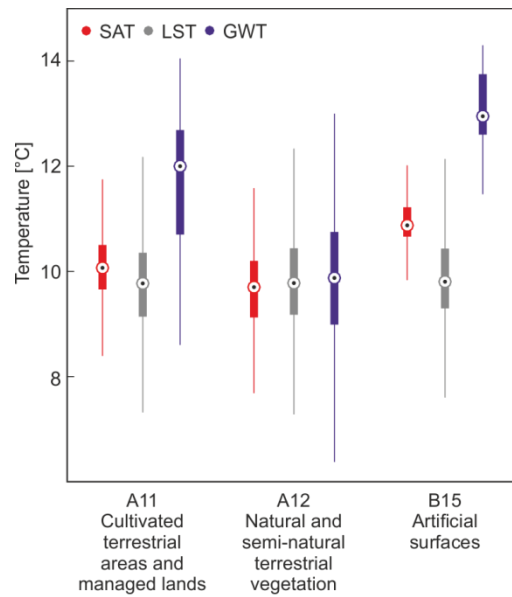


**Figure S3.5.** Influence of land cover on land surface temperature (LST), surface air temperature (SAT), and groundwater temperature (GWT).

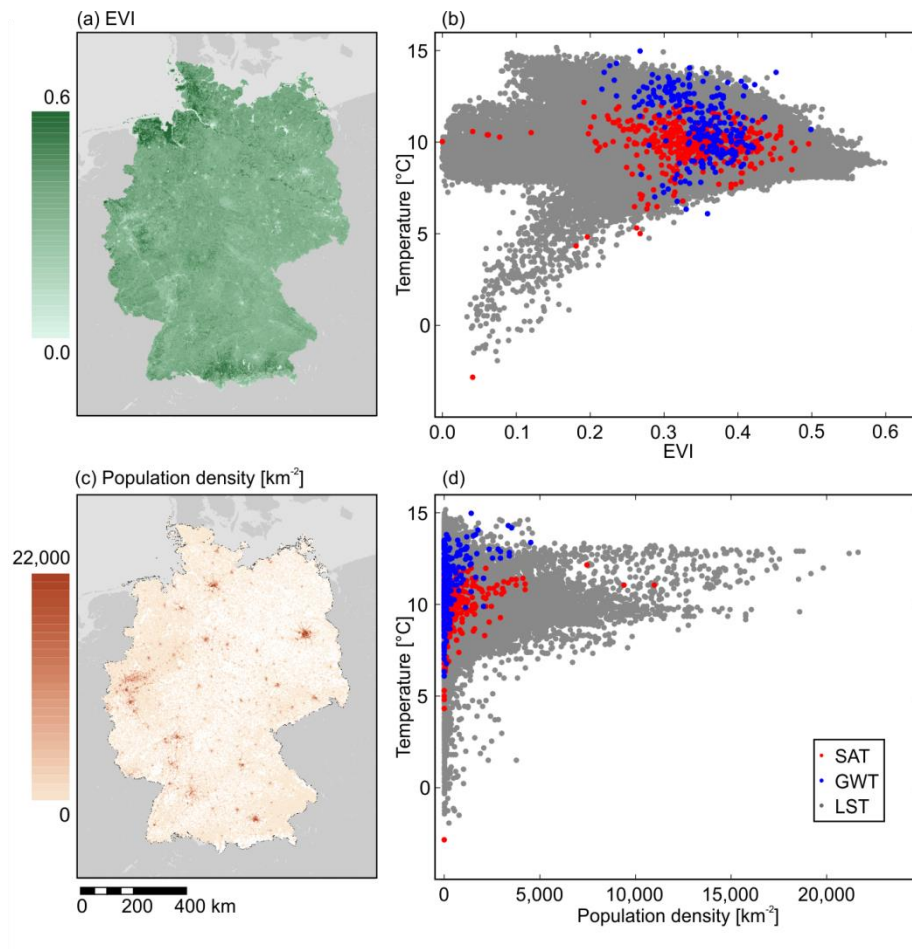


**Figure S3.6.** Influence of vegetation (in form of the enhanced vegetation index EVI) and population on land surface temperature (LST), surface air temperature (SAT), and groundwater temperature (GWT).

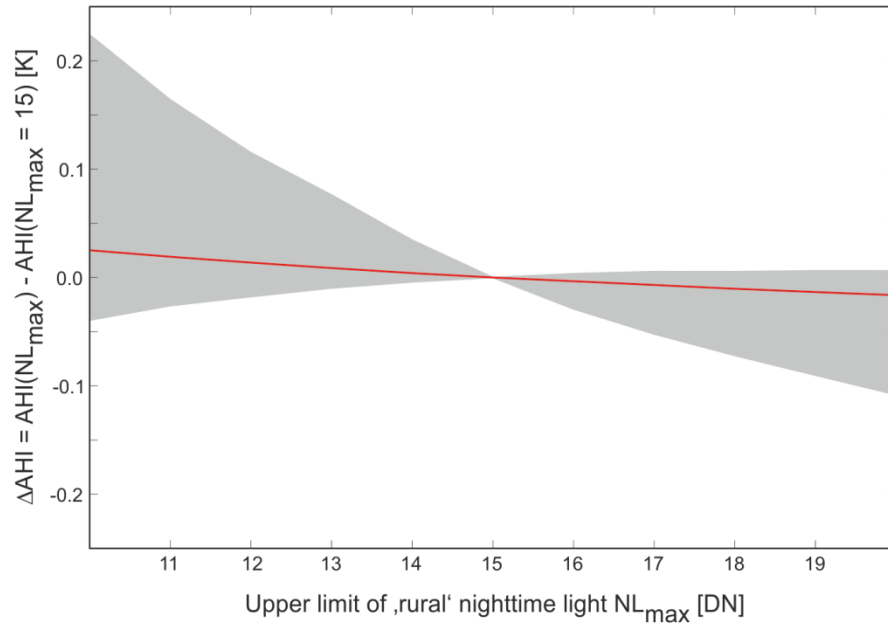


**Figure S3.7.** Influence of the upper limit of nighttime light ( $NL_{max}$ ) used to define the area analyzed for the determination of the rural background temperature  $T_r$  (meaning: allowed nighttime light of  $DN < NL_{max}$ ). Shown is  $\Delta AHI$  for LST, the difference between AHI with a limit of  $NL_{max}$  and AHI with a limit of DN 15. The spatial median for  $\Delta AHI$  is given as a red line. The inner 90 percentiles are colored in grey.

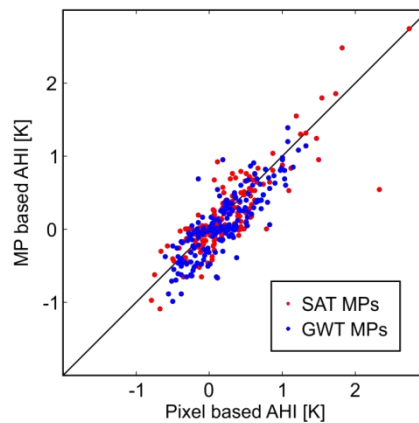


**Figure S3.8.** Influence of measurement point (MP) location on the determined AHI. Comparison of Surface AHI determined using all available pixels vs. determined using only data at MPs of SAT or rather GWT.

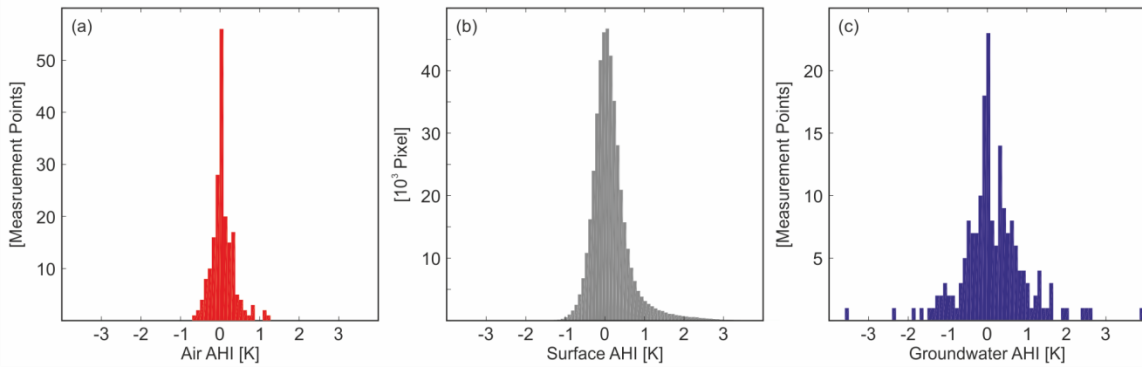


**Figure S3.9.** Histogram of all determined AHIs in Germany for a) air, b) surface and c) groundwater.

**Table S3.1.** Determined sill and range of the (Semi-)Variogram displayed in Fig. 3.2.

	SAT	LST at SAT MPs	GWT	LST at GWT MPs
Sill [K]	1.43	1.77	3.13	2.56
Range [km]	102	111	47	120

MP: Measurement point

**Table S3.2.** Location of the 50 highest surface anthropogenic heat intensities (AHI) in Germany. Only the maximum pixel per heat island is counted.

	Lon	Lat	Surface AHI [K]	Location
1	6.54	50.91	4.5	Open-pit lignite mine, Jülich
2	11.57	48.14	4.3	Munich
3	6.79	51.21	4.0	Düsseldorf
4	11.09	49.44	4.0	Nuremberg
5	7.00	50.93	3.8	Cologne, Deutz
6	10.90	48.37	3.8	Augsburg
7	10.78	52.43	3.7	Wolfsburg
8	13.31	52.50	3.7	Berlin, Wilmersdorf
9	8.48	49.48	3.7	Mannheim
10	6.73	51.48	3.6	Duisburg, Beeckerwert
11	12.85	47.75	3.6	Hochstaufen (Mountain)
12	13.41	52.49	3.5	Berlin, Kreuzberg
13	8.70	50.12	3.5	Frankfurt (Main)
14	10.03	53.54	3.4	Hamburg
15	6.76	49.35	3.4	Saarlouis
16	7.02	51.44	3.3	Essen
17	8.69	53.13	3.3	Bremen
18	6.69	51.20	3.3	Neuss
19	9.20	48.78	3.3	Stuttgart
20	6.87	51.46	3.3	Oberhausen

Identifying Anthropogenic Anomalies in Air, Surface and Groundwater Temperatures  
in Germany

---

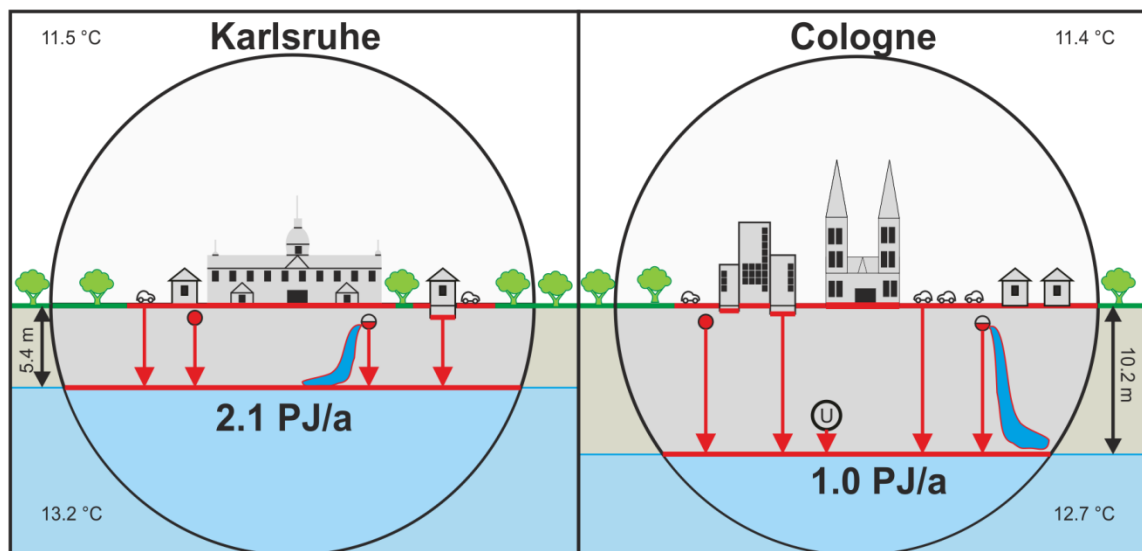
	Lon	Lat	Surface AHI [K]	Location
21	10.41	52.15	3.3	Salzgitter
22	9.74	52.37	3.3	Hannover
23	7.48	51.52	3.3	Dortmund
24	7.14	50.74	3.2	Bonn
25	7.80	48.57	3.2	Kehl
26	8.56	50.04	3.2	Frankfurt Airport
27	10.02	48.39	3.2	Ulm
28	9.54	51.30	3.2	Kassel
29	6.58	51.32	3.2	Krefeld
30	9.23	49.14	3.1	Heilbronn
31	13.51	52.51	3.1	Berlin, Friedrichsfelde
32	13.75	51.06	3.1	Dresden
33	6.90	50.95	3.1	Cologne, Ehrenfeld
34	10.37	47.40	3.1	Schochen (Mountain)
35	7.59	50.37	3.1	Koblenz
36	7.47	50.42	3.1	Neuwied
37	7.02	50.82	3.1	Niederkassel
38	10.47	47.46	3.0	Älpelekopf (Mountain)
39	10.91	49.90	3.0	Bamberg
40	14.63	52.16	3.0	Eisenhüttenstadt
41	12.84	47.61	3.0	Edelweißlahnerkopf(Mountain)
42	12.13	47.85	3.0	Rosenheim
43	8.65	49.87	3.0	Darmstadt
44	7.23	51.28	3.0	Wuppertal
45	9.93	53.56	3.0	Hamburg, Altona
46	12.41	51.34	3.0	Leipzig
47	12.00	51.47	3.0	Halle (Saale)
48	7.19	51.47	3.0	Bochum
49	8.76	51.71	3.0	Paderborn
50	11.59	49.94	3.0	Bayreuth



## 4. Spatial Resolution of Anthropogenic Heat Fluxes into Urban Aquifers

Reproduced from: Benz, S. A.; Bayer, P.; Menberg, K.; Jung, S.; Blum, P. Spatial resolution of anthropogenic heat fluxes into urban aquifers. *Sci. Total Environ.* 2015, 524–525, 427–39.

### Graphical Abstract



## Abstract

Urban heat islands in the subsurface contain large quantities of energy in the form of elevated groundwater temperatures caused by anthropogenic heat fluxes into the subsurface (AHF<sub>S</sub>). The objective of this study is to quantify these AHF<sub>S</sub> and the heat flow they generate in two German cities, Karlsruhe and Cologne. Thus, statistical and spatial analytical heat flux models were developed for both cities. The models include the spatial representation of various sources of AHF<sub>S</sub>: (1) elevated ground surface temperatures, (2) basements, (3) sewage systems, (4) sewage leakage, (5) subway tunnels, and (6) district heating networks. The results show that the district heating networks induce the largest AHF<sub>S</sub> with values greater than 60 W/m<sup>2</sup> and one order of magnitude higher than fluxes from other sources. A covariance analysis indicates that the spatial distribution of the total flux depends mainly on the thermal gradient in the unsaturated zone. On a citywide scale, basements and elevated ground surface temperatures are the dominant sources of heat flow. Overall, 2.1 PJ/a and 1.0 PJ/a of heat are accumulated on average in Karlsruhe and Cologne, respectively. Extracting this anthropogenically originated energy could sustainably supply significant parts of the urban heating demand. Furthermore, using this heat could also keep groundwater temperatures from rising further.



## 4.1. Introduction

A warming of urban areas can be observed worldwide (30). The Urban Heat Island (UHI) phenomenon, as it is called, exists in all diverse layers of a city: from atmosphere (31-33) to surface (34,166) to groundwater (36,145,167,168). While various unfavorable issues such as increased mortality rates during heat waves (169) and regional atmospheric pollution (170) originate from the UHI in the atmosphere, the urban heat island in the subsurface (SUHI) can be beneficial. The increased groundwater and subsurface temperatures provide economic and ecological advantages for the use of shallow geothermal energy systems located in SUHI (58). Arola and Korkka-Niemi (2014) showed that in southern Finland about 50-60% more peak heating power could be utilized from urban areas in contrast to rural areas (59). Furthermore, the geothermal potential of SUHI exceeds the annual residential heating demand in many urban areas (60). Extracting this energy efficiently could save or even reduce CO<sub>2</sub> emissions and other greenhouse gases (61,62). Hähnlein et al. (2013) concludes that a shallow geothermal system is only sustainable, if the generated energy is mainly renewable energy (3). Hence, energy sources of the SUHI should be evaluated and anthropogenic heat fluxes into the subsurface (AHF<sub>S</sub>) of urban areas should be quantified.

Anthropogenic heat has long been discussed regarding the above ground UHI, where it describes the waste heat of human activities such as intense energy use, power generation and vehicular traffic (171). The anthropogenic heat flux in the atmosphere, for example, was simulated from global to city scale by Allen et al. (2011) (172). Its impact on Tokyo was modeled by Ichinose et al. (1999) (173), who found a 1 K temperature increase. For Chicago, San Francisco, Los Angeles, and Philadelphia, Sailor and Lu (2004) showed that the anthropogenic heat flux in the atmosphere on a citywide scale is between 10 and 80 W/m<sup>2</sup> (174).

Urban heat islands in the subsurface (SUHI) have been observed in various cities worldwide such as Virginia Beach, USA (51), Winnipeg, Canada (52), London, UK (53), Oberhausen, Germany (54), Istanbul, Turkey (55), Jakarta, Indonesia (56), Osaka, Japan, and Bangkok, Thailand (57). Some studies focus on the influence of rain and hydrological transport of heat on these thermal anomalies (175,176). In Cologne, Zhu et al. (2015) used a numerical flow and heat transport model to generate various groundwater temperature depth-profiles and compared them with measured profiles (177). It shows mechanisms such as vertical conductive heat input, horizontal advection and transverse dispersion to be the main thermal transport mechanisms. Overall, the consensus view is that anthropogenic heat is the dominant source of the SUHI.

Menberg et al. (2013) define the anthropogenic heat flux into the subsurface (AHF<sub>S</sub>) as the heat input into shallow urban aquifers caused by various anthropogenic heat sources (145). Previously they identified the following main anthropogenic heat sources: increased ground surface temperature (GST), buildings and basements, road tunnels,

sewage networks, sewage leakages, district heating systems, subway systems, reinjections of thermal waste water and other geothermal energy systems such as ground source heat pump and groundwater heat pump systems (36).

In contrast, Hötzl and Makurat (1981) developed a first approach to quantify the heat flow balance of the SUHI in Karlsruhe (178). They identified solar irradiation, the geothermal heat flow, sewage and district heating networks, reinjection of thermal wastewater, and basements as possible heat sources. Furthermore, they estimated the amount of heat transported into the entire urban subsurface for each of these sources, identifying solar insolation and the sewage system to be the dominant heat sources. The revised model by Menberg et al. (2013) includes elevated GST, buildings, reinjection of thermal wastewater, sewage network, sewage leakage, and district heating network as a source of anthropogenic heat (145). A regionalized anthropogenic heat flux model was introduced to account for the uncertainty of all parameters needed for an analytical solution. They performed one Monte Carlo simulation over the entire study area in which groundwater temperatures (GWT), groundwater depth, building density, and basement depth were linked to their spatial distribution. Thus, they were able to estimate the city-scale mean of all individual heat fluxes and the total amount of energy entering the aquifer. For both studied years, 1977 and 2011, elevated ground surface temperatures (GST) were the dominant heat source. Furthermore, a spatial analysis of heat fluxes from buildings was introduced, exhibiting a considerable range between  $-0.1$  and  $>10$  W/m<sup>2</sup>. In Basel, Switzerland, Epting et al. (2013) used a numerical heat transport model to compare the cumulative heat fluxes in 2010 from natural and anthropogenic boundaries (179). They defined these anthropogenic boundaries as reinjection of thermal wastewater as well as small, large, and deep buildings. The absolute heat flux from these different types of buildings was determined to be  $1.8 \times 10^{-1}$  W/m<sup>2</sup>,  $3.0 \times 10^{-11}$  W/m<sup>2</sup> and  $16$  W/m<sup>2</sup> respectively.

Although several previous studies analyzed various AHF<sub>s</sub>, currently, there is no method available that gives a complete and detailed picture of the spatial distribution of AHF<sub>s</sub>. However, in combination with aquifer scale models (e.g. central London, (180)), the detailed spatial distribution of AHF<sub>s</sub> is a crucial requirement for the development of a sustainable thermal energy management tool. The objective of the present study is therefore to introduce a method that quantifies the vertical AHFs from various heat sources through the unsaturated zone into the groundwater and displays their spatial distribution. This two-dimensional approach builds up on the model framework developed by Menberg et al. (2013)(145), however it separates spatial variability and uncertainty of the input parameters. Hence, a more accurate determination of heat fluxes is obtained. In addition, the heat flux model is applied in two German cities, Karlsruhe and Cologne, providing a comparison of the determined AHF<sub>s</sub>. Finally, we investigate the possible implications of the AHFs on thermal groundwater use by comparing the annual thermal recharge of AHFs with the residential space heating demand to evaluate the potential of the SUHI as a sustainable source of thermal energy.

## 4.2. Material and Methods

### 4.2.1. Study Sites

The chosen study areas cover major parts of two German cities: Karlsruhe, located in the south-west of Germany close to the Rhine, and Cologne, located in the west of Germany next to the Rhine (Figure 4.1). Both study sites are limited to areas dominated by urban land-use, i.e. mostly built-up areas, within the city districts. Large green spaces, such as woodlands and agricultural areas, at the borders of the city districts are not included in the investigations. In the following, the geology, hydrogeology, groundwater temperatures (GWT), and urban infrastructures of these cities are described. An overview and general statistics of both study areas can be found in Table 4.1.

**Table 4.1.** General statistical information on both study areas.

Study site	Karlsruhe	Cologne
Year of measurements	2011	2009
Area [km <sup>2</sup> ]	61.9	81.3
Building density [%]	21.0	21.6
Population	286,000 <sup>a</sup>	485,000 <sup>b</sup>
Mean air temperature [°C]	11.5 <sup>c</sup>	11.4 <sup>c</sup>
Mean ground surface temperature [°C]	14.4 <sup>d</sup>	14.7 <sup>d</sup>
Number of groundwater wells	82	73
Mean groundwater temperature [°C]	13.2	12.7
Mean groundwater depth [m]	5.4	10.2
Groundwater measurement depth [m below groundwater]	2-3	1

<sup>a</sup>Office for urban development, Karlsruhe (Stadt Karlsruhe, Amt für Stadtentwicklung) (181); <sup>b</sup>Office for urban development and statistics, Cologne (Stadt Köln, Amt für Stadtentwicklung und Statistik) (182); <sup>c</sup>German Weather Service (Deutscher Wetterdienst, DWD) (183); <sup>d</sup>own calculations (see section 4.2.2).

#### Karlsruhe

Karlsruhe is in the state of Baden-Württemberg at 49°00' N and 8°24' E, 115 m above sea level and is the smaller of the two cities in respect to size and population (Table 4.1).

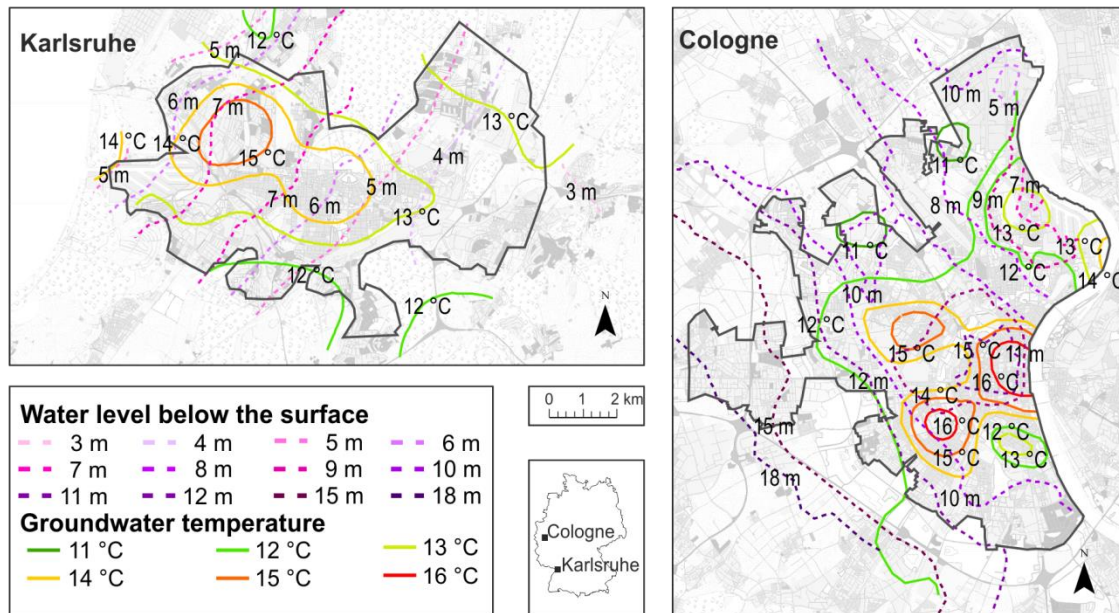


**Figure 4.1.** Location of the study areas with annual mean groundwater level maps and annual mean groundwater temperature maps. Groundwater temperature in Karlsruhe was measured daily at about 9 m below the surface in 2011. The groundwater temperature in Cologne was measured at about 11 m below surface in 2009. Specific well locations are shown in Figures S1 and S2 (supplementary material).

#### *Geology, Hydrogeology, and Groundwater Temperatures*

Karlsruhe is located in the Upper Rhine Graben, a Cenozoic continental rift valley filled by Quaternary and Tertiary sediments. The Quaternary sediments with a varying thickness of around 150 m are dominated by sands and gravels showing minor contents of silts, clays and stones. The unsaturated zone of the study site consists mostly of sands and gravels (184).

The upper aquifer has a thickness of up to 20 m, and the general groundwater flow direction is northwest towards the Rhine. In total, 82 groundwater monitoring wells in the study area are equipped with Ackermann WPS05 data loggers. These wells are continuously monitored by the Public Works Service Karlsruhe. Measurements of groundwater temperatures (GWT) and hydraulic heads are daily recorded (accuracy: 0.1°C) at 7 AM at 2 to 3 m below the water surface. Well locations, weather station, and seasonal variability of GWT for three selected wells are exemplary shown in Figure S4.1 (supporting information). To disregard the inter-annual variations in GWT and groundwater depth, the mean annual GWT and groundwater levels of the annual cycle between March 2011 and 2012 are used in this study. Both GWT and groundwater level were interpolated by Menberg et al. (2013) (36,145) using kriging in GIS (ESRI® ArcInfo™ 10.0) and are shown in Figure 4.1 with a resolution of 15 m × 15 m. The arithmetic mean of the GWT is  $13.2 \pm 1.3^\circ\text{C}$ . Its maximum is located northwest of the

city center, where it reaches more than 16°C. A second minor hot spot is located directly under the city center, where temperatures up to 15°C were measured. The inner quantile range urban heat island intensity (UHII<sub>90-10</sub>) that cuts the lowest and highest 10% of the temperatures before calculating the urban heat island intensity is 1.9 K (36).

The average groundwater depth is  $5.4 \pm 2.1$  m below the surface. At its deepest points in the western part, the water table reaches 10.4 m below the surface, while the eastern area exhibits shallow groundwater at around 3 m below the surface.

### *Urban Infrastructures*

According to the GMES Urban Atlas, 83% of the study area in Karlsruhe is shaped by urban land use and consists of residential, commercial, and industrial units, roads and rail networks, etc. The overall building density is 21.0%, with the highest densities in the city center (Figure 4.2).

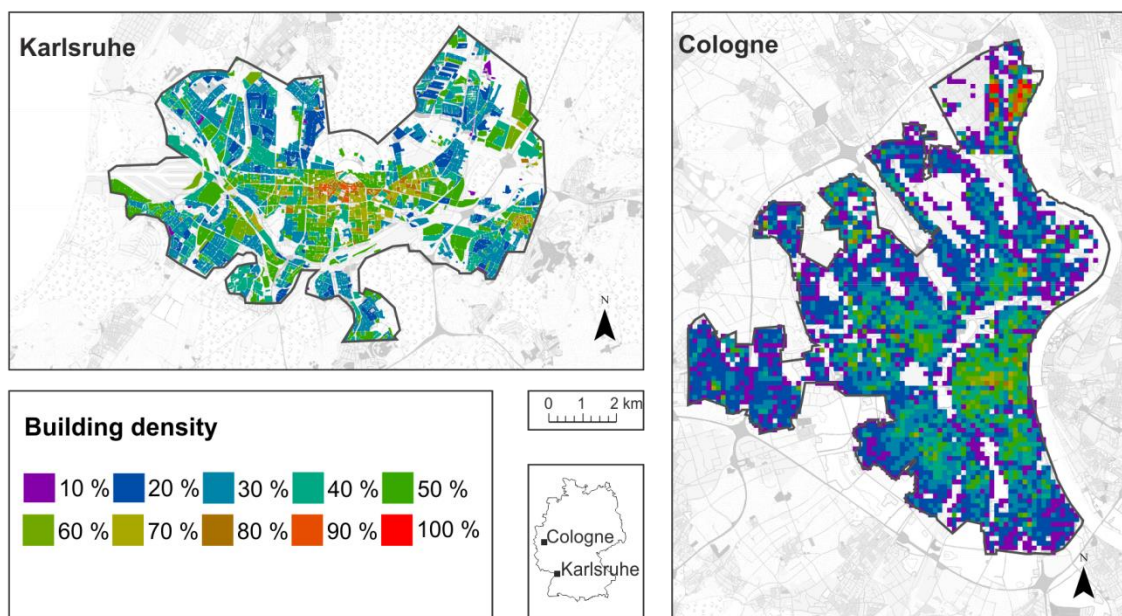


**Figure 4.2.** Building density of Karlsruhe and Cologne.

Figure 4.3 shows the sewage system and the district-heating network of Karlsruhe. The sewage system is a combined (rainwater and sanitary) system in the city center and a separate sewage system in the suburbs. The district heating network has been used since the early 19th century. Today, it is about 90 km long and connected to 23,500 households with an available power output of 25PJ/a. In 2001, a survey performed by the newspaper for local economy (*Zeitung für kommunale Wirtschaft, Zfk*) showed that the heat loss is about 10%.



Geothermal applications, such as reinjection wells for industrial thermal wastewater, are also operating in Karlsruhe (Figure 4.3). The current maximum licensed reinjection temperature is 20°C (185). In Karlsruhe about 4.5 Million m<sup>3</sup> of thermal wastewater are reinjected each year in 29 wells, altogether transporting slightly less than 0.1 PJ into the groundwater (145).

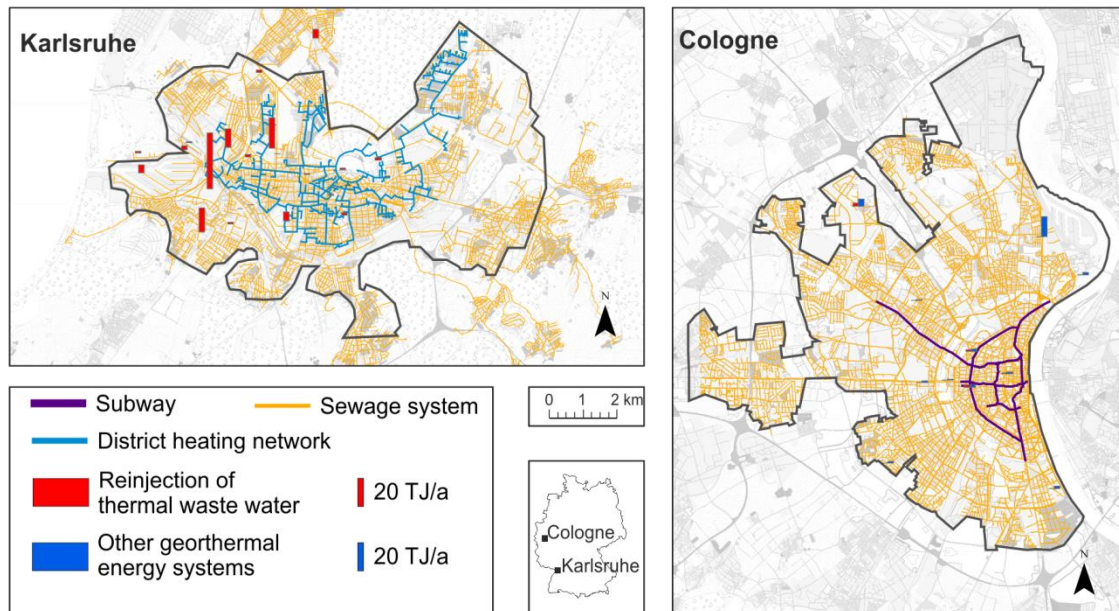


**Figure 4.3.** Location of sewage-, district heating-, and subway systems in the study area as well as the location of industrial reinjection wells of thermal wastewater and other geothermal energy systems such as ground source heat pump and groundwater heat pump systems. As of 2011 Karlsruhe does not have a subway system. The location of the district heating network in Cologne was not available.

## Cologne

Cologne is located in the state of North Rhine-Westphalia about 300 km further downstream along the Rhine. The city lies at 50°56' N and 6°57' E at 53 m above sea level. Due to the large number of observation wells needed for the spatial assessment of groundwater characteristics in this study, the study area is limited to the urban area on the western bank of the Rhine. It thus covers only about a quarter of the total city area.

### *Geology, Hydrogeology, and Groundwater Temperatures*

Cologne is located in the south of the Lower Rhine Basin. Above the Paleozoic bedrock are Tertiary and Quaternary layers. The shallow subsurface is composed of 15 to 25 m thick Pleistocene terrace deposits that, like in Karlsruhe, predominantly consist of gravels and sands (186).

The uppermost aquifer has a thickness of about 30 m and the general flow direction is northeast towards the receiving stream, the Rhine. GWT and groundwater levels (accuracy of 0.01 m) were measured in 73 groundwater wells between September and October 2009 using SEBA KLL-T logging equipment. GWTs were measured at 1 m below the water table (approximately 11 m under the surface). At this depth the annual temperature variations are insignificant compared to the accuracy of 0.1°C in most wells (187). The mean GWT is  $12.7 \pm 1.3^\circ\text{C}$  and the average observed groundwater level is  $10.2 \pm 6.1$  m below the surface. GWT and depth were interpolated by Jung (2013) and Menberg et al. (2013) using kriging (Table 4.1; Figure 4.1)(36,187). GWT in Cologne reaches a maximum of  $16.2^\circ\text{C}$  in the city center under the main railway station. The  $\text{UHII}_{10-90}$  is 2.1 K (36). The groundwater level in the northeast, close to the Rhine, is reaching up to 2 m below the surface, whereas it is 20 m below surface in the southwest of the city.

### *Urban Infrastructures*

In Cologne, 97 % of the study area is shaped by urban land use (188). Using the estate map of Cologne, the building density is estimated with 21.6 % (Table 4.1). Again, the highest densities are found primarily in the city center, but also in industrial areas (Figure 4.2). A subway system exists with about 19 km of underground rail inside the study area (Figure 4.3). Although Cologne has a district heating network, no utility plan was accessible. However, its power output inside the study area (western bank) is 0.8 PJ/a with a heat loss of around 6 % (189).

While both reinjections of thermal wastewater and other geothermal energy systems, such as ground source heat pump and groundwater heat pump systems, exist in Cologne, the latter are more frequent. Overall 33 TJ/a are extracted for heating inside the study area, while the cooling load only accounts for 6 TJ/a (Figure 4.3).

## **4.2.2. Ground Surface Temperatures**

Ground surface temperatures (GST) in both cities are determined according to the different surface materials within the urban environment and the characteristic deviation of the GST of these individual surfaces types from the ambient air temperature. Dědeček et al. (2012) measured the difference  $\Delta T$  between ambient air temperature and GST for several surface types, such as grass surfaces (0.2 - 0.8 °C), sand and bare soil (1.5 - 2.0 °C), and asphalt (4.0 - 5.0 °C) (190). We estimate the GST by adding these temperature differences to the air temperature according to the land use types within each city. The share of the different surface types in each individual land use type is adopted from the land use categorization of the Global Monitoring for Environment and Security (GMES)

**Table 4.2.** Assumed ground surface temperatures for different land uses.

Landuse description	Surface types <sup>a</sup> [%]			$\Delta T^b$ [K]			Area covered [%]	
	sand and bare soil	grass	asphalt	min	median	max	Karlsruhe	Cologne
Forests	0	100	0	0.20	0.50	0.80	9.2	0.5
Green urban areas	0	100	0	0.20	0.50	0.80	7.9	7.6
Discontinuous very low density urban fabric (S.L. < 10%)	10	85	5	0.52	0.83	1.13	5.3	-
Agricultural + semi-natural areas + wetlands	50	50	0	0.85	1.13	1.40	0.0	3.2
Discontinuous low density urban fabric (S.L.: 10% - 30%)	10	70	20	1.09	1.43	1.76	0.2	0.2
Construction sites	100	0	0	1.50	1.75	2.00	7.6	4.8
Mineral extraction and dump sites	100	0	0	1.50	1.75	2.00	0.9	0.7
Water bodies	100	0	0	1.50	1.75	2.00	0.9	0.4
Land without current use	100	0	0	1.50	1.75	2.00	0.1	0.0
Sports and leisure facilities	25	50	25	1.48	1.81	2.15	1.5	0.9
Railways and associated land	90	0	10	1.75	2.03	2.30	2.9	2.8
Discontinuous medium density urban fabric (S.L.: 30% - 50%)	10	50	40	1.85	2.23	2.60	5.8	2.4
Discontinuous dense urban fabric (S.L.: 50% - 80%)	10	25	65	2.80	3.23	3.65	15.6	18.8
Port areas	25	0	75	3.38	3.81	4.25	2.2	7.3
Continuous urban fabric (S.L. > 80%)	5	10	85	3.50	3.96	4.43	10.4	19.8
Industrial, commercial, public, military and private units	5	0	95	3.88	4.36	4.85	19.9	20.1
Isolated structures	0	0	100	4.00	4.50	5.00	1.5	0.3
Fast transit roads and associated land	0	0	100	4.00	4.50	5.00	0.1	-
Other roads and associated land	0	0	100	4.00	4.50	5.00	7.9	10.4

<sup>a</sup>GMES Urban Atlas(188), <sup>b</sup>Dědeček et al. (2012) (190); S.L.: sealing layer.



Urban Atlas (Table 4.2). Annual mean air temperatures are measured by the German Weather Service (183). In both cities the meteorological stations are located at nearby airports (Figure S4.1 and S4.2, supplementary material). The average air temperature was 11.5°C in Karlsruhe and 11.4°C in Cologne. Unfortunately the spatial distribution of the air temperatures was not available and thus air temperature differences within the study areas had to be neglected. However, we believe them to be insignificant compared to the range of  $\Delta T$  (Table 4.2).

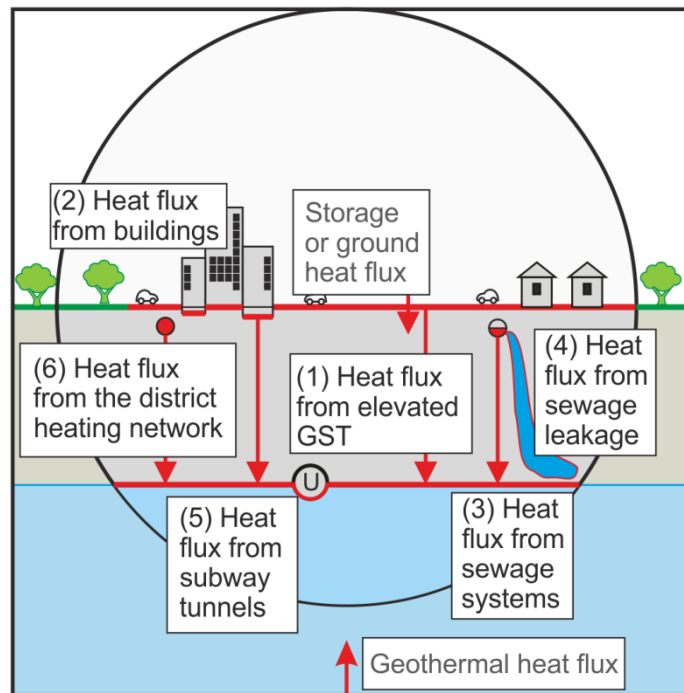


**Figure 4.4.** Overview of the different studied heat fluxes: (1) heat flux from elevated ground surface temperatures (GST), (2) heat flux from buildings (i.e. basements), (3) heat flux from sewage systems, (4) heat flux from sewage leakage, (5) heat flux from subway tunnels, and (6) heat flux from district heating networks. The sum of the heat fluxes (1)-(6) represent the total anthropogenic heat flux into the subsurface ( $q_{tot}$ ) determined in this study (Eq. 4.8).

### 4.2.3. Mathematical Modeling of the Anthropogenic Heat Flux into the Subsurface

#### Local Anthropogenic Heat Flux Model

Our heat flux model focuses on the unsaturated zone quantifying mean annual heat fluxes from the heat sources to the top and therefore into the aquifer. In the unsaturated zone, temperature gradients and heat fluxes in the vertical direction are dominant(9). Hence, only vertical anthropogenic heat fluxes through the unsaturated zone are quantified. Fluxes from geothermal energy systems that interact directly and horizontally with the groundwater are not considered, yielding six heat sources for AHF<sub>S</sub>: (1) elevated

ground surface temperatures (GST), (2) basements (i.e. buildings), (3) sewage systems, (4) sewage leakage, (5) subway tunnels, and (6) district heating networks (see Figure 4.4).

In this study, the regional anthropogenic heat flux model (145) was further developed. While still using a statistical and analytical approach, we introduce a local anthropogenic heat flux model, which analyzes all dominant heat fluxes spatially by determining them for each pixel  $ij$  of the study area (resolution:  $15\text{ m} \times 15\text{ m}$ ) individually. Thus, a spatially resolved heat flux map is obtained.

To account not only for the spatial variability, but also for uncertainties and the natural ranges of parameters, such as thermal conductivity and basement depth, a Monte Carlo approach with 800 iterations is employed to determine the fluxes in each pixel. The assumed parameter ranges used in the Monte Carlo simulation are shown in Table 4.3. In all cases, a triangular distribution is chosen, defined by a minimum, a maximum and mode value stating the value with the highest probability. Where applicable, the parameter ranges previously applied by Menberg et al. (2013) are also used here (145). In contrast to the previous work, we thus separate spatial variability (e.g. different groundwater temperatures in different pixels), from plain uncertainty (e.g. measurement accuracy), allowing a more accurate determination of heat fluxes and heat flow. In the following, both spatial variability and uncertainty will be expressed in form of a standard deviation.

The model comprises three steps. First, the heat flux of all individual AHF<sub>S</sub> sources in each pixel  $ij$  is determined using a Monte Carlo simulation. Second the anthropogenic heat flux per pixel  $ij$  is determined, which describes the average heat flux of the pixel. Third, the anthropogenic heat fluxes of all pixels are summed up to determine the heat flow, i.e. the energy amount transported into the aquifer over the whole study area in the span of one year.

**Table 4.3.** Assumed parameter range distribution for the Monte Carlo simulation. Triangular distribution was used as a standard.

Heat flux process	Parameter	Name	Unit	Karlsruhe			Cologne		
				Minimum	Mode	Maximum	Minimum	Mode	Maximum
Increased GST	$\lambda$	Thermal conductivity <sup>a</sup>	W/mK	0.3	1	1.8	0.3	1	1.8
	$T_{GS}^{ij}$	Ground surface temperature	°C	see Table 4.2 and Figure 4.5			see Table 4.2 and Figure 4.5		
	$T_{GW}^{ij}$	Groundwater temperature	°C	see Figure 4.1			see Figure 4.1		
	$\delta T_{GW}$	Accuracy groundwater temperature	°C	-0.1	0	0.1	-0.1	0	0.1
	$d_{GW}^{ij}$	Groundwater depth	m	see Figure 4.1			see Figure 4.1		
	$\delta d_{GW}$	Accuracy groundwater depth	m	-0.01	0	0.01	-0.01	0	0.01
	$bf^{ij}$	Building density	%	see Figure 4.2			see Figure 4.2		
	$\delta bf$	Uncertainty of building density	%	-5	0	5	-5	0	5
Buildings	$T_B$	Temperature of basement / ground floor <sup>b</sup>	°C	15	17.5	20	15	17.5	20
	$d_B$	Basement depth	m	0	2.5	6	0	2.5	6
Sewage system	$T_{SS}$	Sewage temperature <sup>c, d</sup>	°C	12	18.5	25	10.33	17.59	26.8
	$d_{SS}$	Depth of sewage drains <sup>e, d</sup>	m	1	2	5	1	2	5
	$D_{SS}$	Diameter of sewage drains <sup>f, d</sup>	m	0.1	0.4	2	0.08	0.3	4.6
	$l_{SS}$	Length of sewage network <sup>c, e, d</sup>	m	770,000	880,000	990,000	907,051.5	1,007,835	1,108,618.5
Sewage leakage	$c_{pSS}$	Heat capacity of wastewater <sup>c</sup>	J/kgK	3708	4120	4532	3708	4120	4532
	$\rho_{SS}$	Density of wastewater <sup>c</sup>	kg/m <sup>3</sup>	990	1100	1210	990	1100	1210
	$V_{SS}$	Annual wastewater volume <sup>c, d</sup>	m <sup>3</sup> /a	33,997,000	35,707,500	37,418,000	48,873,592	49,000,000	50,873,592
	$r_L$	Leakage rate <sup>f</sup>	%	5	15	25	5	15	25
District heating	$P_{DH}$	Heat loss from district heating pipes <sup>c, g</sup>	MW	7.99	9.13	10.27	1.25	1.39	1.53
	$r_d$	Percentage heat flux directed downwards	%	25	37.5	50	25	37.5	50
	$D_{DH}$	Diameter of district heating pipes <sup>f</sup>	m	0.1	0.4	2	-	-	-
	$l_{DH}$	Length of district heating network	m	85,500	90,000	94,500	-	-	-

Heat flux process	Parameter	Name	Unit	Karlsruhe			Cologne		
				Minimum	Mode	Maximum	Minimum	Mode	Maximum
Subway system	$T_{SW}$	Subway system temperature <sup>h</sup>	°C	-	-	-	10	18.6	25.5
	$l_{SW}$	Length of subway system <sup>h</sup>	m	-	-	-	19,000	20,000	21,000
	$D_{SW}$	Diameter of subway system <sup>h</sup>	m	-	-	-	6.9	7	7.3
	$t_{SW}$	Thickness of subway tunnel walls <sup>h</sup>	m	-	-	-	-	1.1	-

<sup>a</sup> Menberg et al. (2013) (145), VDI 4640 (2010) (191); <sup>b</sup> DIN EN ISO 13370 (2008) (192); <sup>c</sup> Makurat (1980) (193); <sup>d</sup> municipal drainage operator of Cologne (Köln, Stadtentwässerungsbetriebe) (194); <sup>e</sup> civil engineering department Karlsruhe (Stadt Karlsruhe, Tiefbauamt) (195); <sup>f</sup> Eiswirth et al. (2002) (196), Klinger (2007) (197); <sup>g</sup> Rheinenergie AG, 2012 (198); <sup>h</sup> Public transport company, Cologne (Kölner Verkehrsbetriebe, KVB) (199).

### Anthropogenic Heat Flux from Individual Sources

The anthropogenic heat flux from individual sources represents the energy per square meter and second that each AHF<sub>S</sub> source transports into the groundwater. Most of the energy is transferred by conductive heat transport processes and can be determined using Fourier's law  $|q| = \lambda \cdot \nabla T = \lambda \cdot \Delta T / \Delta d$ . Here  $\lambda$  is the thermal conductivity and  $\nabla T$  the thermal gradient that can be derived by dividing the difference in temperature  $\Delta T$  by the distance  $\Delta d$  between two points. For the anthropogenic heat fluxes from elevated ground surface temperatures ( $q_{GST}$ ) the temperature gradient depends on the difference between GST ( $T_{GS}$ ) and GWT ( $T_{GW}$ ) as well as on the depth  $d_{GW}$  of the water table (see Figure 4.4). It can be calculated as follows:

$$q_{GST}^{ij} = \lambda \cdot \frac{T_{GS} - (T_{GW}^{ij} + \delta T_{GW})}{d_{GW}^{ij} + \delta d_{GW}} \quad (4.1)$$

Here  $\delta T_{GW}$  and  $\delta d_{GW}$  are the uncertainties of the measured value. The index  $ij$  indicates different values for different pixels  $ij$ . The assumed ranges can be found in Table 4.3.  $q_{GST}$  is determined for every pixel with a building density of less than 100%.

Anthropogenic heat fluxes from buildings (see Figure 4.4) are calculated for each pixel  $ij$  with a building density of more than 0%. Here, the difference between the temperatures inside buildings/basements ( $T_B$ ) and GWT, as well as the vertical distance between building depth ( $d_B$ ) and groundwater depth, determine the thermal gradient, leading to the following equation:

$$q_{Bld}^{ij} = \lambda \cdot \frac{T_B - (T_{GW}^{ij} + \delta T_{GW})}{(d_{GW}^{ij} + \delta d_{GW}) - d_B} \quad (4.2)$$

Thermal insulation of buildings is not considered here, because in Germany, ground slab isolation was not implemented into construction regulations until the late 1990s (200), leaving most buildings without insulation. Buildings that reach into the aquifer are still separated from the groundwater by the concrete slab of the basement. Thus, a minimal distance between heat source and groundwater of 30 cm was assumed. Heat flux from basement walls was not considered.

Anthropogenic heat flux from the sewage system (see Figure 4.4) is determined for every pixel, in which sewage drains are present. It comes in two ways: first, there is the conductive heat transfer ( $q_{SS}$ ), represented again based on Fourier's law:

$$q_{SS}^{ij} = \lambda \cdot \frac{T_{SS} - (T_{GW}^{ij} + \delta T_{GW})}{(d_{GW}^{ij} + \delta d_{GW}) - d_{SS}} \quad (4.3)$$

Sewage Pipes that reach into the aquifer are still separated from the groundwater by their mantle. Thus, a minimal distance between heat source and groundwater of 10 cm was assumed.

Second, there is an advective heat transfer representing sewage leakage ( $q_{SL}$ ). To quantify the heat flux from sewage leakage, the energy content of the leaked water is estimated and divided by the area covered by the sewage system within the pixel:

$$q_{SL}^{ij} = c_{pSS} \rho_{SS} r_L \cdot [T_{SS} - (T_{GW}^{ij} + \delta T_{GW})] \cdot \frac{V_{SS}}{l_{SS} D_{SS}} \quad (4.4)$$

Here,  $c_{pSS}$  is the heat capacity of waste water,  $\rho_{SS}$  the density,  $r_L$  the leakage rate,  $V_{SS}$  the volume of wastewater,  $l_{SS}$  the length of the sewage system, and  $D_{SS}$  the diameter of the sewage system.

Anthropogenic heat fluxes originating from the subway system (see Figure 4.4) are determined for all relevant pixels using Fourier's law. However, the subway tunnels in Cologne run under the groundwater level at around 19 m below surface (199). Hence, groundwater and heat source are merely separated by the tunnel walls with a thickness  $t_{SW}$  of 1.1 m:

$$q_{SW}^{ij} = \lambda \cdot \frac{T_{SW} - (T_{GW}^{ij} + \delta T_{GW})}{t_{SW}} \quad (4.5)$$

Anthropogenic heat flux from the district heating network (see Figure 4.4) is determined for all relevant pixels. The downwards directed percentage  $r_d$  of the systems heat loss  $P_{DH}$  is taken and divided by the area covered by the district heating network leading to the following equation:

$$q_{DH}^{ij} = P_{DH} \cdot r_{DH} \cdot \frac{1}{l_{DH} \cdot D_{DH}} \quad (4.6)$$

Due to the chosen approach the heat flux from the district heating networks shows no spatial variability.

### Anthropogenic Heat Flux per Pixel

The anthropogenic heat flux  $\bar{q}^{ij}$  per pixel is determined by scaling the anthropogenic heat fluxes of the individual sources to the reference area, i.e. the pixel size, of 15 m × 15 m. This is done for each heat source independently before the individual heat fluxes per pixel are added up to give the total heat flux of all anthropogenic heat sources for each pixel  $ij$ :

$$\begin{aligned} \bar{q}_{tot}^{ij} = & \underbrace{q_{GST}^{ij} \cdot [1 - (bf^{ij} + \delta bf)]}_{\bar{q}_{GST}^{ij}} + \underbrace{q_{Bld}^{ij} \cdot (bf^{ij} + \delta bf)}_{\bar{q}_{Bld}^{ij}} + \underbrace{q_{SS}^{ij} \cdot \frac{l_{SS}D_{SS}}{A_{Pixel}N_{SS}}}_{\bar{q}_{SS}^{ij}} \\ & + \underbrace{q_{SL}^{ij} \cdot \frac{l_{SS}D_{SS}}{A_{Pixel}N_{SS}}}_{\bar{q}_{SL}^{ij}} + \underbrace{q_{SW}^{ij} \cdot \frac{l_{SW}D_{SW}}{A_{Pixel}N_{SW}}}_{\bar{q}_{SW}^{ij}} + \underbrace{q_{DH}^{ij} \cdot \frac{l_{DH}D_{DH}}{A_{Pixel}N_{DH}}}_{\bar{q}_{DH}^{ij}} \end{aligned} \quad (4.7)$$

To transfer the reference area to the pixel size, the building density ( $bf$ ) is used for heat fluxes from increased GST and from buildings. For all other AHF<sub>s</sub> sources, the heat fluxes per pixel are calculated by multiplying the anthropogenic heat fluxes with the fraction of the total area covered by the heat source (i.e. length  $l$  × diameter  $D$ ), and the total area of the relevant pixels (area  $A_{Pixel}$  of one pixel × number  $N$  of relevant pixels).

### Heat Flow

The total anthropogenic heat flow into the subsurface  $I_{tot}$  is the energy input per year of the entire study area and is obtained by adding up the anthropogenic heat flux of every pixel as follows:

$$I_{tot} = A_{Pixel} \cdot \sum_{ij} \bar{q}_{tot}^{ij} \quad (4.8)$$

In addition, the heat flow generated by each individual AHF<sub>s</sub> source is determined accordingly.

#### 4.2.4. Geothermal Potential

The analysis of the geothermal potential  $Q/P_h$  offers a comparison of the potential heat content of the aquifer  $Q$  to the annual residential space heating demand  $P_h$ . The potential heat content of the aquifer is the geothermal heat content of the urban aquifer for a given temperature reduction  $\Delta T$ . It can be estimated using the following equation (60,201):

$$Q = Q_W + Q_S = A \cdot d \cdot n \cdot c_{p,W} \cdot \Delta T + A \cdot d \cdot (1 - n) \cdot c_{p,S} \cdot \Delta T \quad (4.9)$$

Here  $Q_W$  and  $Q_S$  are the potential heat contents of groundwater and solid respectively,  $A$  is the urban area,  $d$  is the aquifer thickness,  $n$  is the porosity of the aquifer, and  $c_{p,W}$  and  $c_{p,S}$  are the volumetric heat capacities of water and solid.

The annual residential space heating demand  $P_h$  is estimated as follows:

$$P_h = A_{LS} \cdot p \cdot q_{hd} \quad (4.10)$$

where  $A_{LS}$  is the average living space per person,  $p$  is the population and  $q_{hd}$  is the average annual unit heating demand (60). The parameter values for both study sites are listed in Table 4.4.

In this study, we further introduce the sustainable geothermal potential  $I_{tot}/P_h$  that compares the annual anthropogenic heat input into the aquifer (i.e. the heat flow  $I_{tot}$  from above) to the annual residential space heating demand and hence, describes the capacity of sustainable energy usage.

**Table 4.4.** Assumed Parameters for the estimation of the potential heat content of the aquifer and residential space heating demand.

Parameter	Name	Unit	Karlsruhe	Cologne
A	Urban area <sup>a</sup>	km <sup>2</sup>	61.9	81.3
D	Aquifer thickness	m	30 ± 20	20 ± 10
N	Porosity of the aquifer	%	20 ± 5	20 ± 5
$c_{p,W}$	Volumetric heat capacity of water <sup>b</sup>	kJ/m <sup>3</sup> K	4,150	4,150
$c_{p,S}$	Volumetric heat capacity of solid <sup>b</sup>	kJ/m <sup>3</sup> K	2,400 ± 200	2,150 ± 50
$\Delta T$	Temperature reduction <sup>c</sup>	K	4	4
Q	Potential heat content of the aquifer	PJ	20 ± 1	17 ± 9
$A_{LS}$	Average living space per person <sup>d</sup>	m <sup>2</sup>	43	42.3
p	Population <sup>s</sup>	-	286,000 ± 500	485,000 ± 500
$q_{hd}$	Average annual heating demand <sup>e</sup>	kJ/m <sup>2</sup>	525,600 ± 180,000	
$P_h$	Annual space heating demand	PJ	7 ± 2	11 ± 4
	Capacity for space heating	Years <sup>-1</sup>	3.1 ± 2.4	1.5 ± 1.0

<sup>a</sup> see Table 4.1; <sup>b</sup> VDI 4640 (2010) (191); <sup>c</sup> Zhu et al. (2010) (60); <sup>d</sup> Timm (2008) (202); <sup>e</sup> Nitsch (2002) (203).



## 4.3. Results and Discussion

### 4.3.1. Ground Surface Temperatures

The results of the estimated GST are shown in Figure 4.5 and Table 4.2. The mean GST in Karlsruhe is 14.4°C and in Cologne 14.7°C. This difference can be explained by a higher percentage of sealed areas in Cologne (Table 4.2).

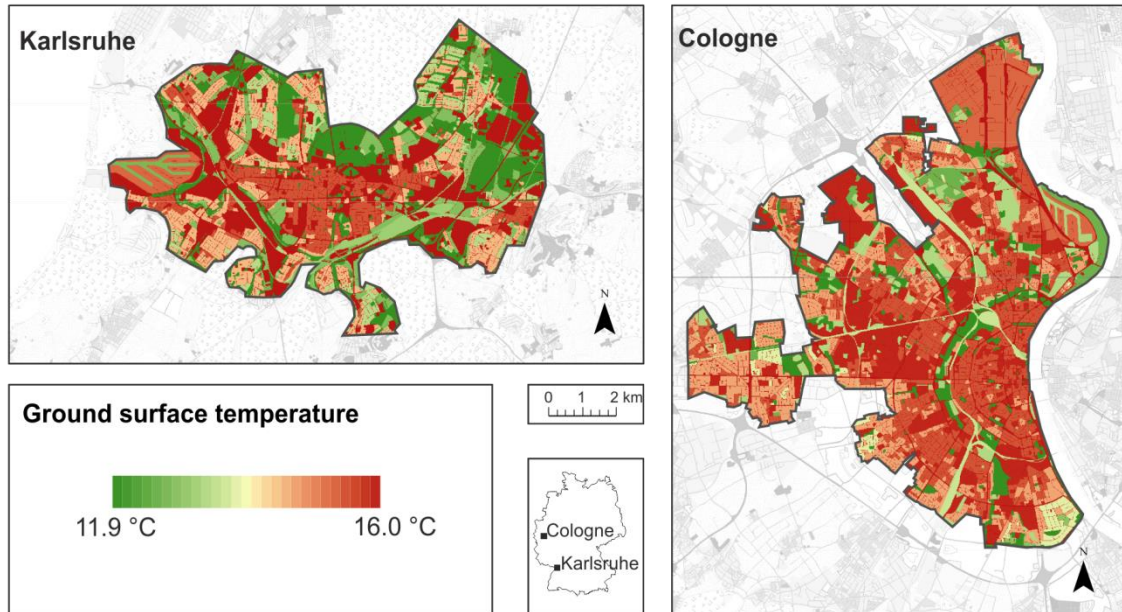


**Figure 4.5.** Estimated mean ground surface temperatures (GST) in Karlsruhe and Cologne.

### 4.3.2. Anthropogenic Heat Flux into the Subsurface

#### Anthropogenic Heat Flux from Individual Sources

The results for the anthropogenic heat fluxes of all evaluated individual AHF<sub>S</sub> sources are shown in Figure 4.6 (and Table S4.1). The most dominant source of AHF<sub>S</sub> is the district heating network in Karlsruhe with an average AHF<sub>S</sub> of 62.8 W/m<sup>2</sup> and an uncertainty (in form of standard deviation) of ±42.9 W/m<sup>2</sup>, which is one order of magnitude more than fluxes from any other AHF<sub>S</sub> source.

Increased GST is the least dominant source of anthropogenic heat flux with values of  $0.24 \pm 0.11$  W/m<sup>2</sup> in Karlsruhe and  $0.21 \pm 0.06$  W/m<sup>2</sup> in Cologne. Fluxes from increased GST correspond to the storage or ground heat fluxes (see Figure 4.4) that are commonly used in literature to describe the energy balance of the surface. Storage heat fluxes in Basel, Switzerland, were measured hourly over the span of three days (8<sup>th</sup>, 25<sup>th</sup> and 26<sup>th</sup> June 2002) by Rigo and Parlow (2007) (204). They found fluxes ranging from about -90

at night to  $240 \text{ W/m}^2$  at daytime. Similarly Liebenthal and Foke (2007) measured rural storage fluxes near Lindenberg in Germany on 10<sup>th</sup> June 2003 finding fluxes ranging from  $-50$  at night to  $150 \text{ W/m}^2$  around noon (205). While the here presented AHF<sub>s</sub> from elevated GST fall within range of both of these studies, it is important to note that both studies analyzed only a short time frame in the summer month June and are therefore expected to be elevated compared to the annual mean. A time series of 37 years of monthly measurements of storage heat flux in a rural site in Eastern Minnesota was presented by Baker and Baker (2002) (206). Here the storage heat flux ranges between  $-6$  and  $6 \text{ W/m}^2$  at 1.6 m depth and is better comparable to our findings of annual flux from elevated GST through the entire unsaturated zone. Furthermore, in 2013 the Intergovernmental Panel on Climate Change (4,207) analyzed a time frame of two decades. On a global scale, they estimated storage heat fluxes as the residual from the energy balance of the surface from  $0.2$  to  $1.0 \text{ W/m}^2$ , with the higher values representing fluxes into the ocean. This agrees well with our results for AHF<sub>s</sub> from increased GST. In contrast, Beltrami et al. (2006) discussed the absorbed ground surface heat flux in the continental Northern Hemisphere using borehole temperature profiles of up to 400 m depth (208). They determined absorbed fluxes ranging from  $0.025$  to  $0.075 \text{ W/m}^2$  in central Europe for the time period from 1930 to 1980.

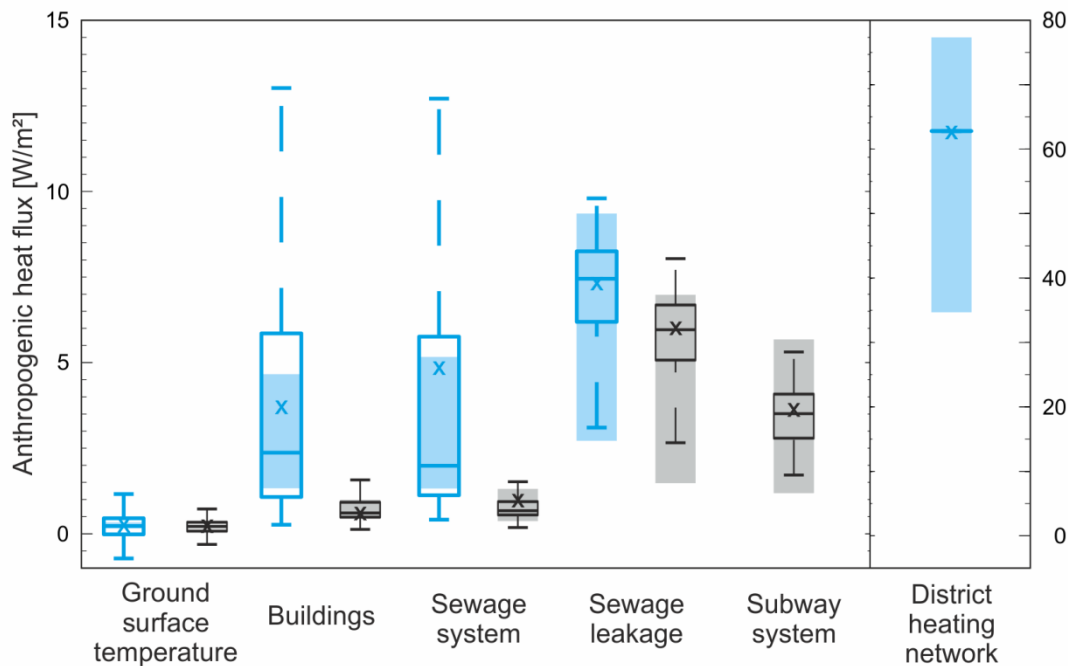


**Figure 4.6.** Anthropogenic heat fluxes in Karlsruhe (blue) and Cologne (black) for all individual anthropogenic heat flux processes. Spatial variabilities are shown as boxplots, whereas the interquartile ranges of uncertainty are indicated by fully colored boxes. Mean values are indicated with a cross.

The results for anthropogenic fluxes from buildings into the groundwater ( $3.61 \pm 3.37 \text{ W/m}^2$  in Karlsruhe;  $0.57 \pm 0.47 \text{ W/m}^2$  in Cologne) are on the lower end of

the fluxes through the ground floor slabs of a building, which range between 0 and 20 W/m<sup>2</sup> (209,210). However, they agree well with the estimation of ~2 W/m<sup>2</sup> heat loss directly beneath a building (211). In Karlsruhe, fluxes from buildings as well as conductive fluxes from the sewage system ( $4.73 \pm 6.72$  W/m<sup>2</sup> in Karlsruhe;  $0.94 \pm 0.77$  W/m<sup>2</sup> in Cologne) are significantly higher than in Cologne. This is also reflected in the long-tailed distribution of fluxes in Karlsruhe (Figure 4.6), where 4% of all buildings and 15% of the sewage system generate fluxes above 10 W/m<sup>2</sup>. In contrast in Cologne less than 0.01% of all fluxes from buildings and 1% of all conductive fluxes from sewage systems are above 10 W/m<sup>2</sup>. The obvious explanation is that due to the higher groundwater levels in Karlsruhe 40% of all buildings and 1% of all sewage pipes are only 2 meter above the groundwater level. Furthermore, 2 % of all buildings reach into the groundwater, leaving the concrete slab of the basement (thickness: 30 cm) to separate groundwater and anthropogenic heat source. These marginal distances between groundwater and heat source lead to a high thermal gradient and therefore to a high anthropogenic heat flux. These findings corroborate the results for Basel, Switzerland, which show a dominant heat flux of 16 W/m<sup>2</sup> for buildings reaching into the groundwater, while other buildings generate fluxes of less than 1 W/m<sup>2</sup> (179). Furthermore, our models show that the anthropogenic heat flux from buildings in Karlsruhe can be decreased by 45% to  $2.0 \pm 0.8$  W/m<sup>2</sup> (with a spatial variability of 1.8 W/m<sup>2</sup>), if the assumed basement depth is reduced by only 0.4 m, following the model of Menberg et al. (2013) (145).

### **Anthropogenic Heat Flux per Pixel**

The anthropogenic heat flux of the average pixel is 1.10 W/m<sup>2</sup> for Karlsruhe and 0.39 W/m<sup>2</sup> for Cologne, respectively (Figure 4.7 and Table S4.2). In contrast, the geothermal heat flux (see Figure 4.4) in Karlsruhe is only about 0.08 W/m<sup>2</sup> (212) and in Cologne 0.06 W/m<sup>2</sup> (201), indicating that AHFs dominate the heat flux into the urban aquifer.

Karlsruhe once again shows significantly higher fluxes and a wider distribution compared to Cologne. This is also reflected in the values of the standard deviation of both the spatial variability (1.49 W/m<sup>2</sup> in Karlsruhe; 0.38 W/m<sup>2</sup> in Cologne), as well as the uncertainty (0.73 W/m<sup>2</sup> in Karlsruhe; 0.12 W/m<sup>2</sup> in Cologne) of the results. The reason is the comparatively high groundwater level in Karlsruhe and the assigned uncertainty in the basement depth (0-6 m), which, in combination, result in a large and strongly variable thermal gradient, especially under buildings.

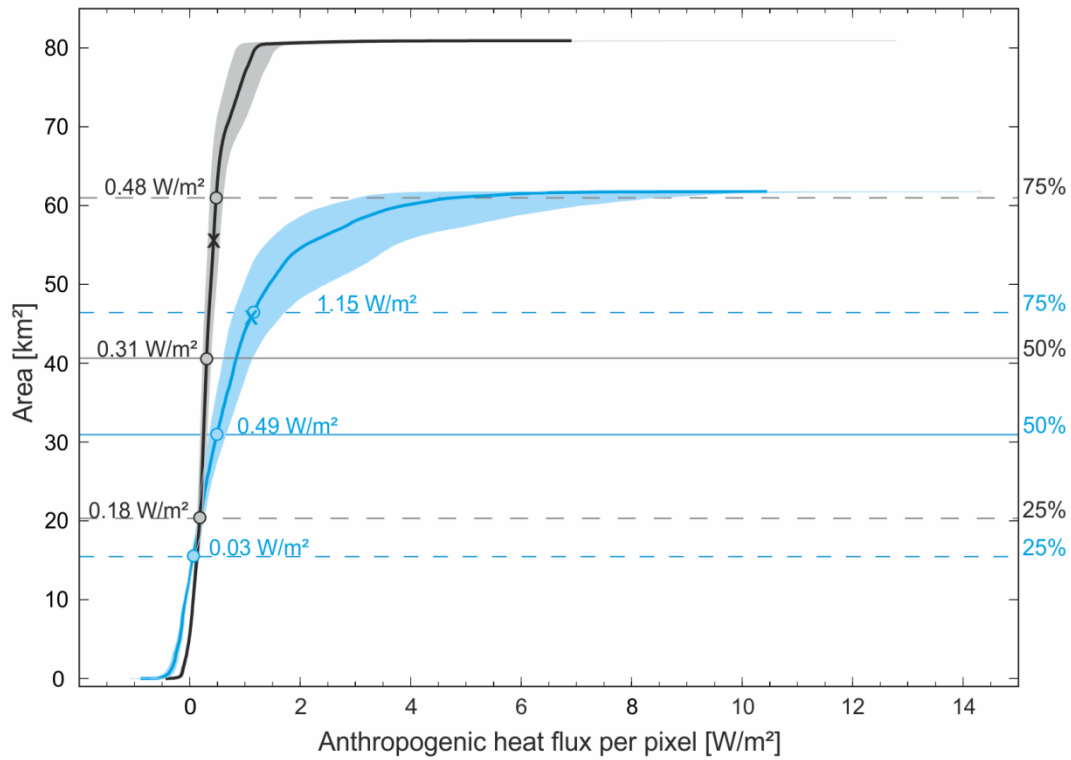


**Figure 4.7.** Anthropogenic heat flux per pixel of Karlsruhe (blue) and Cologne (black). The spatial variability is shown as the cumulative plot, whereas the interquartile range of the uncertainty is colored. Median as well as 25<sup>th</sup> and 75<sup>th</sup> percentiles are further highlighted, the particular mean for each city is indicated with a cross.

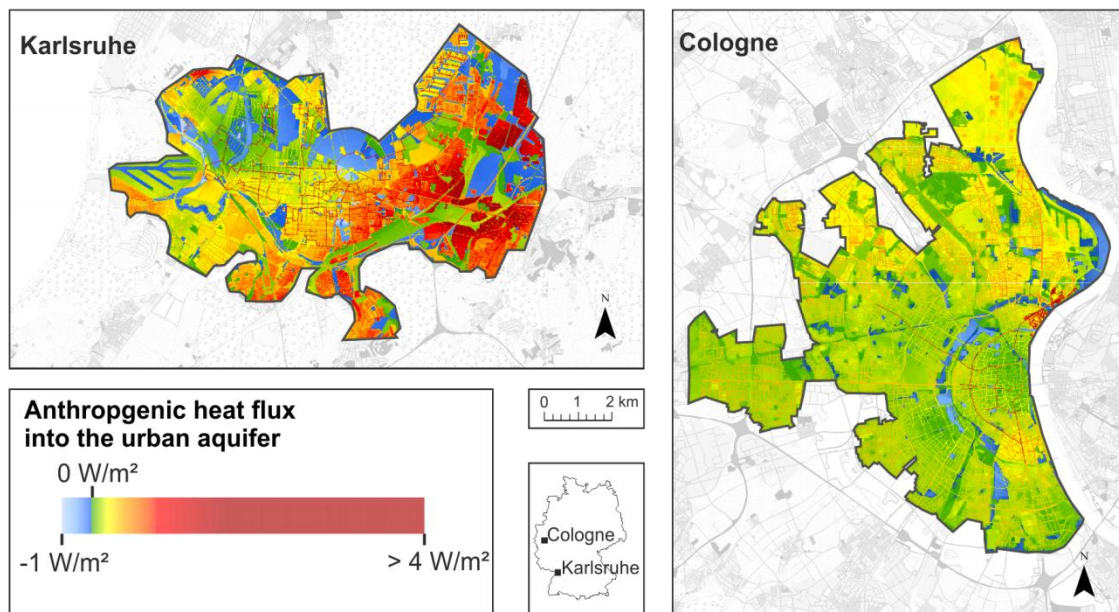


**Figure 4.8.** Total anthropogenic heat flux per pixel into the groundwater of both study areas, Karlsruhe and Cologne. Negative fluxes indicate fluxes from groundwater to the surface. The spatial resolution is  $15 \text{ m} \times 15 \text{ m}$ .

The spatial variability of the anthropogenic heat flux per pixel is depicted in Figure 4.8. Cologne shows a comparatively homogeneous distribution with the highest fluxes along the subway line and next to the sewage network near the Rhine - in the area with the highest groundwater level. The northeast of Cologne reveals generally higher fluxes than the southwest, originating from a low groundwater temperature combined with elevated GST and again comparatively high groundwater levels. In this area, the largest groundwater heat pump system is installed with a heating load of 13.8 TJ/a. In this particular location, the heating efficiency of the geothermal installation is reduced by the low GWT, but at the same time, the sustainability of the system is increased through the high local AHFs.

The highest fluxes in Karlsruhe are found to the east of the city center, where groundwater levels are highest. In the western part, it is mostly the district-heating network that leads to particularly high heat fluxes. Negative AHFs, i.e. fluxes from the groundwater to the surface, occur mainly in park areas, where the estimated ground surface temperature is lower than the groundwater temperature. Such green spaces are more common in Karlsruhe than in Cologne.

### Heat Flow

The sum of these upward directed fluxes accumulates to a median heat flow of -0.07 PJ/a in Karlsruhe and to only -0.01 PJ/a in Cologne. However, they are insignificant compared to the downward directed fluxes that accumulate to a median of 1.67 PJ/a in Karlsruhe and 0.95 PJ/a in Cologne. The overall energy balance is shown in Figure 4.9 and Table S4.3. The mean of the total anthropogenic heat flow of Karlsruhe yields  $2.1 \pm 1.4$  PJ/a, more than double that of Cologne ( $1.0 \pm 0.3$  PJ/a). The most dominant contributors of heat in Karlsruhe are buildings/basements with  $1.5 \pm 1.4$  PJ/a. In Cologne, buildings generally do not reach into the groundwater and therefore only account for  $0.3 \pm 0.1$  PJ/a. Nonetheless, they are the second most dominant AHFs source. Although insignificant regarding the anthropogenic heat flux of all individual sources, increased ground surface temperatures (GST) are the most dominant contributor of anthropogenic heat flow in Cologne, with values of  $0.4 \pm 0.1$  PJ/a due to the spatial extent of the affected areas. In Karlsruhe, fluxes from increased GST generate a heat flow of  $0.3 \pm 0.1$  PJ/a, which represents the second largest source of anthropogenic heat flow in the groundwater. In contrast, fluxes caused by industrial reinjection of thermal waste water and other geothermal systems account for only 0.08 PJ/a in Karlsruhe and -0.03 PJ/a in Cologne (145,187).

Although being dominant regarding anthropogenic fluxes from individual sources, the district heating networks of each study area only account for a minor heat flow of  $0.11 \pm 0.02$  PJ/a in Karlsruhe and  $0.02 \pm 0.01$  PJ/a in Cologne, respectively (Table S4.3). For Karlsruhe, Menberg (2013) determined similar values with minor differences for the heat flow from buildings and from increased GST (213). This can easily be explained by

the different estimations for basement depths and GST in both studies. Overall, the separation of spatial variability and uncertainty introduced in this study reduces the standard deviation of the total flow by 87% in comparison to the previous approach by Menberg et al. (2013)(213).

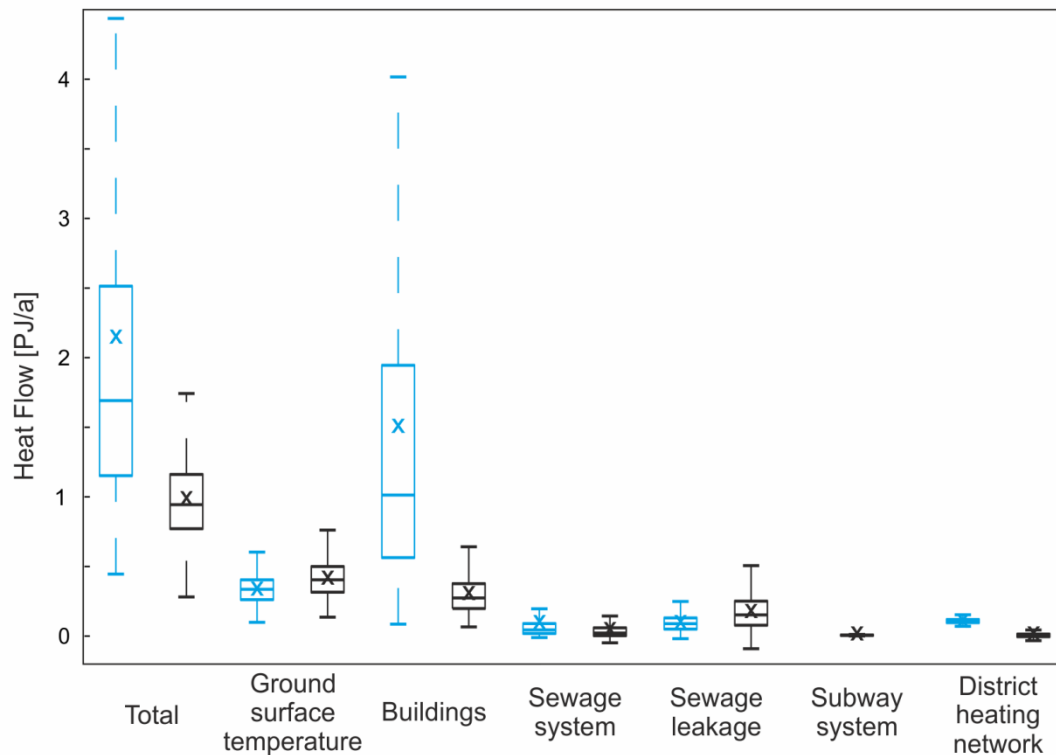


**Figure 4.9.** Boxplot of the heat flow of Karlsruhe (blue) and Cologne (black). Mean values are indicated with a cross.

### Covariance Analysis

To analyze the model sensitivity in relation to the uncertainty of the Monte Carlo simulation, Spearman's rank correlation coefficients between the total heat flow and the parameter range distributions are determined (Figure 4.9, Table 4.3). The results are illustrated in Figure 4.10a); a detailed list of all parameters and their statistical significance  $p$  is given in Tables S4.4 (supporting information). As expected, the uncertainty of basement depth shows the highest correlation to the heat flow in Karlsruhe, whereas it has only a minor influence on fluxes in Cologne, where buildings rarely reach into the groundwater.

Sewage temperature and the percentage of downwards directed heat flux show slightly elevated correlations in Cologne, confirming that the advective fluxes are more important in a city with a low thermal gradient. As expected, the heat flow of both cities is highly affected by the thermal conductivity, a parameter that is not expected to show a significant spatial variability in our study areas, due to the geological settings. However,



since no measured values from within the study site were available, a broad range of 0.3 to 1.8 W/mK (Table 4.3) was chosen to account for all eventualities.

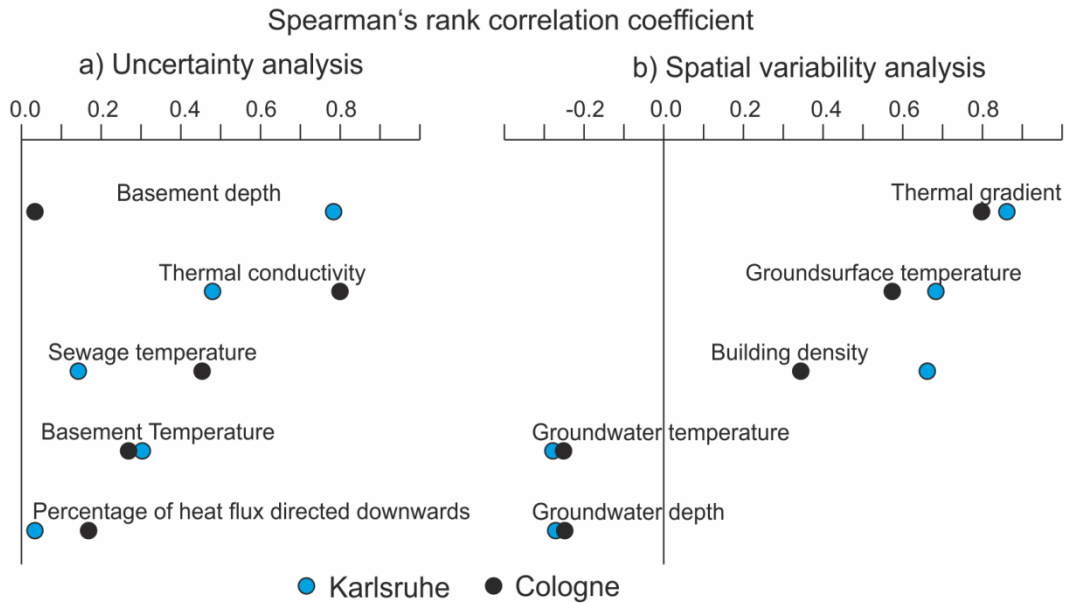


**Figure 4.10.** Spearman's rank correlation coefficients between the heat flow and the individual parameters as an analysis of uncertainty and between the heat flux per pixel and the individual parameters as an analysis of spatial variability. The thermal gradient  $\nabla T$  was determined through:  $\nabla T = (T_{GS} - T_{GW})/d_{GW}$ . Only parameters with a correlation coefficient of  $> 0.1$  are shown. The statistical variance  $p$  can be found in the supporting information (Table S4.4 and S4.5).

To analyze the model sensitivity in relation to the spatial variability of its input parameters, Spearman's rank correlation coefficients between the spatial variability of the total heat flux and the input parameters are determined (Figures 4.1, 4.2, 4.4 and 4.8). The results are illustrated in Figure 4.10b). A detailed list of all parameters and their statistical significance  $p$  is given in Tables S4.5 (supporting information). The spatial variability of the thermal gradient  $\nabla T = (T_{GS} - T_{GW})/d_{GW}$  is most influential regarding the spatial variability of the anthropogenic heat flux per pixel. However, nearly all uncertainties of the thermal gradient stem from the GST, which itself shows a high influence on the spatial variability of the anthropogenic heat flux per pixel. For further improvement of this method, it is therefore recommended to focus on spatial measurements of GST data in urban areas. Besides the thermal gradient and its linked parameters, building density is the most significant parameter.

### 4.3.3. Implications

Figure 4.11 shows the potential heat content of the aquifer for a temperature reduction of 4 K, annual residential space heating demand and the annual anthropogenic heat flow

determined for both study sites. The mean values and the uncertainties of the potential heat input as well as the annual heating demand are also given in Table 4.4. The heat content of the aquifer in Karlsruhe could provide enough heat to cover the space heating demand for  $3.1 \pm 2.4$  years, while Cologne's aquifer only yields heat for  $1.5 \pm 1$  years.

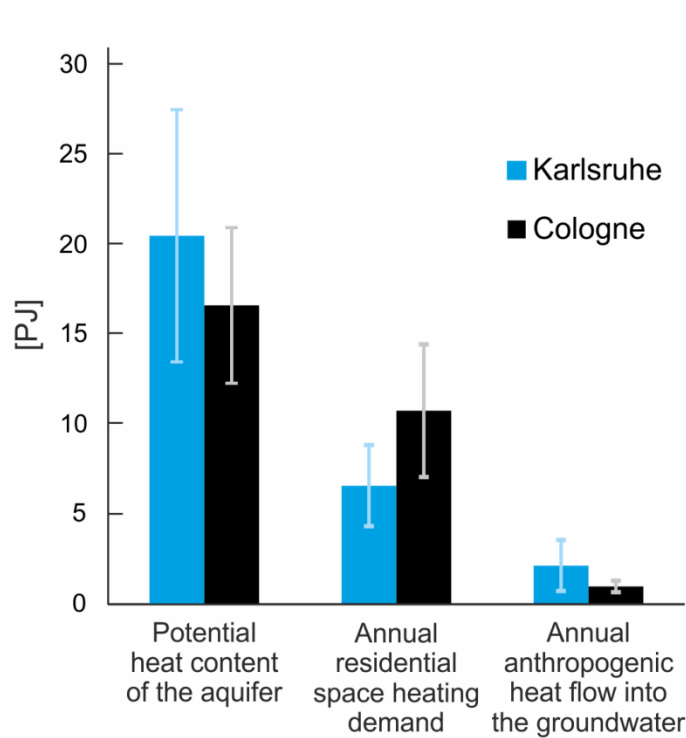


**Figure 4.11.** Comparison of the determined anthropogenic heat flow with the annual residential space heating demand and the potential heat content of the aquifer for a temperature reduction of 4 K. Uncertainties are given in form of standard deviations.

These differences in the geothermal potential stem from a thinner aquifer in Cologne in combination with a higher population and therefore higher space heating demand inside the study area. An earlier study of the entire municipal Cologne showed a capacity for space heating in between 2.5 and 10.7 years for a temperature reduction of 2 to 6 K and assuming a rather optimistic average annual heating demand of 180,000 kJ/m<sup>2</sup> (60). Furthermore, in Westminster, a large proportion of buildings could support their own heating demand using ground source heat pumps without losing control of the ground thermal capacity (214). In Finland, 25% to 40% of annually constructed residential buildings could be heated utilizing groundwater (215). However, using the heat content of the aquifer for space heating will cool the urban aquifer by several degrees. In order to sustainably utilize the geothermal potential, the energy budget of all geothermal energy systems combined - heating and cooling - should not exceed the annual anthropogenic heat input into the aquifer. Nevertheless, assuming a steady-state system, this energy could sustainably supply 32% of the annual residential space heating demand in Karlsruhe and 9% in Cologne. This would be even more if additional cooling systems were to be installed. However, currently, a total of only about 0.03 PJ of heat are



extracted in Cologne each year. This is merely 5% of the annual heat flow generated by AHF<sub>S</sub>. In Karlsruhe, there are currently no significant industrial geothermal heating systems in place. On the contrary, 0.1 PJ of energy are transported into the groundwater each year mainly due to reinjection of thermal wastewater.

## 4.4. Conclusions

The development of a sustainable geothermal energy concept should be the goal of cities that want to use renewable energies such as shallow geothermal energy or thermally manage their groundwater resources. Hence, a 2D statistical analytical heat flux model was developed and successfully applied to the cities of Karlsruhe and Cologne, Germany. The heat flux model gives a spatial representation of the vertical subsurface anthropogenic heat fluxes into urban aquifers. Hence, a sustainable thermal energy management tool could be developed for both cities.

We found that district heating pipes are the dominant source of anthropogenic heat fluxes with average values of more than  $60 \text{ W/m}^2$ , more than one order of magnitude higher than all other heat sources. Only sewage pipes and basements reaching into the groundwater are the cause of equally extraordinary heat sources with maximal fluxes of  $40 \text{ W/m}^2$  and  $14 \text{ W/m}^2$ , respectively. These can be found in Karlsruhe, where the groundwater level is on average only 5.4 m below the subsurface. In Cologne, with a mean groundwater depth of 10.2 m, buildings and the sewage system do not reach into the groundwater. Thus, their fluxes show only minor spatial variability. Furthermore, in Cologne, the total  $\text{AHF}_S$  is lower ( $0.39 \pm 0.12 \text{ W/m}^2$ ) and has a lower spatial variability ( $\pm 0.38 \text{ W/m}^2$ ) than the total  $\text{AHF}_S$  in Karlsruhe ( $1.10 \pm 0.73 \text{ W/m}^2$ ; spatial variability of  $\pm 1.49 \text{ W/m}^2$ ).

While dominating the local anthropogenic fluxes, the district heating network is insignificant for the citywide  $\text{AHF}_S$  budget in both cities. Heat from buildings ( $1.51 \pm 1.36 \text{ PJ/a}$  in Karlsruhe;  $0.31 \pm 0.14 \text{ PJ/a}$  in Cologne) and elevated GST ( $0.34 \pm 0.10 \text{ PJ/a}$  in Karlsruhe;  $0.42 \pm 0.13 \text{ PJ/a}$  in Cologne) are dominant contributors of the anthropogenic heat flow into the urban aquifer. In Karlsruhe, buildings are the source of 70% (in Cologne 30%) of the annual heat transported into the groundwater, which is mainly caused by buildings reaching into or close to the groundwater. A covariance analysis confirmed these findings. Hence, basement depth is the most influential factor to citywide heat flow in cities with a high groundwater level.

The spatial distribution of fluxes, however, is mostly influenced by the thermal gradient of the unsaturated zone. A cold GWT combined with a high GST, as well as a high groundwater level, results in elevated fluxes like in the east of Karlsruhe. Overall,  $2.15 \pm 1.42 \text{ PJ}$  and  $0.99 \pm 0.32 \text{ PJ}$  of thermal energy are annually transported into the groundwater of Karlsruhe and Cologne due to  $\text{AHF}_S$ . This is sufficient to sustainably cover 32% and 9% of the annual residential space heating demand of Karlsruhe and Cologne, respectively.

## Acknowledgments

The financial support for S. Benz from the German Research Foundation (DFG) under grant number BL 1015/4-1 and the Swiss National Science Foundation (SNSF) under grant number 200021L 144288 is gratefully acknowledged. Furthermore, we thank Susanne Reimer, Friedhelm Fischer, Rüdiger Haas and Ralf Schneider (Tiefbauamt Karlsruhe), Annette März (Stadt Karlsruhe, Umwelt- und Arbeitsschutz), and Manuel Rink (Stadtwerke Karlsruhe GmbH) as well as Sebastian Greve (Stadtentwässerungsbetriebe Köln), Stephanie Kempkes (Landesamt für Natur, Umwelt und Verbraucherschutz NRW), Karin Landsberg (Bezirksregierung Köln), and Stefan Simon (Erft-Verband) for their valuable support with data and additional information. Finally, we would like to thank the four anonymous reviewers for their comments.

## Supplementary Material

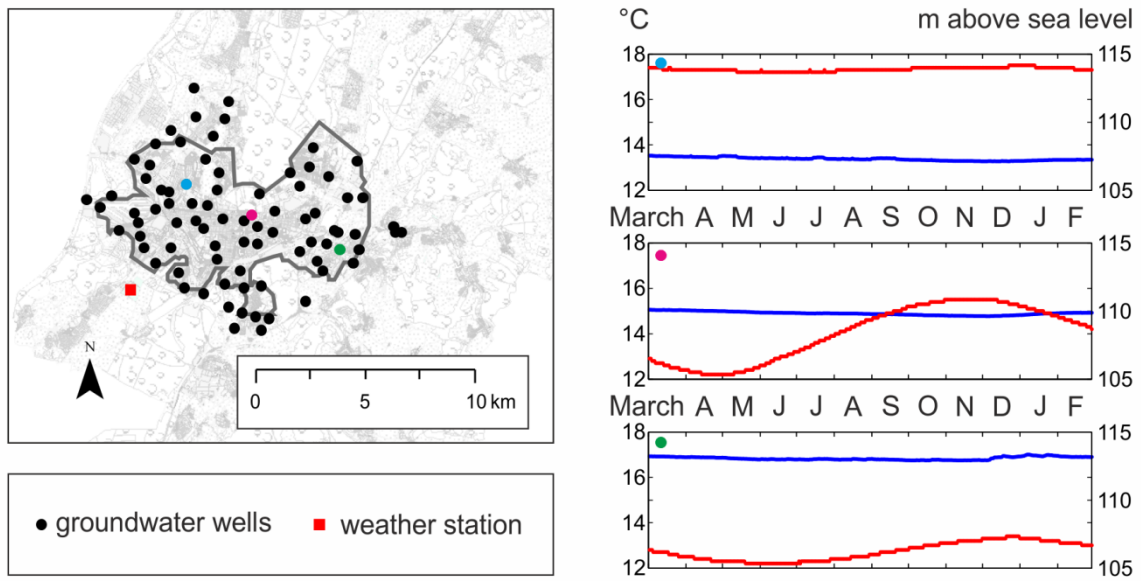


**Figure S4.1.** Well location in Karlsruhe and plots of groundwater temperature (red) as well as groundwater depth (blue) for selected wells (marked blue, pink, and green on the map).

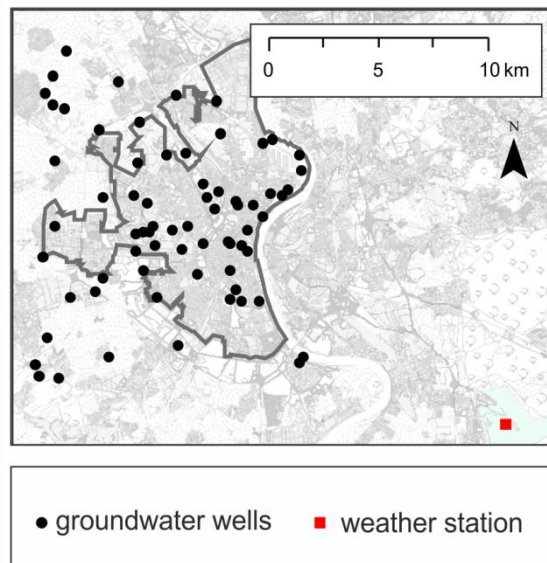


**Figure S4.2.** Groundwater well location and weather station of Cologne

**Table S4.1.** Results for the anthropogenic heat flux from individual heat sources of both cities. Uncertainty and spatial variability are given as the standard deviation.

Anthropogenic heat flux from	Increased GST	Buildings	Sewage system	Sewage leakage	Subway system	District heating
[W/m <sup>2</sup> ]	Karlsruhe					
Mean	0.24	3.61	4.73	7.15	-	62.80
Uncertainty	0.11	3.37	6.72	6.95	-	41.87
Spatial variability	0.35	3.04	6.16	1.41	-	-
[W/m <sup>2</sup> ]	Cologne					
Mean	0.21	0.57	0.94	5.87	3.53	-
Uncertainty	0.06	0.25	0.77	8.52	3.13	-
Spatial variability	0.17	0.47	2.19	1.28	0.91	-

**Table S4.2.** Results for the total anthropogenic heat flux per pixel of both cities. Uncertainty and spatial variability are given as the standard deviation.

Mean total heat flux per pixel [W/m <sup>2</sup> ]	Karlsruhe	Cologne
Mean	1.10	0.39
Uncertainty	0.73	0.12
Spatial variability	1.49	0.38

**Table S4.3.** Results for the heat flow of both cities.

Heat flow	Total	Increased GST	Buildings	Sewage system	Sewage leakage	Subway system	District heating
[PJ/a]	Karlsruhe						
Mean	2.15	0.34	1.51	0.10	0.10	-	0.11
Standard deviation	1.42	0.10	1.36	0.16	0.06	-	0.02
[PJ/a]	Cologne						
Mean	0.99	0.42	0.31	0.05	0.18	0.02	0.02
Standard deviation	0.32	0.13	0.14	0.06	0.13	0.00	0.01

**Table S4.4.** Results and statistical significance of the Spearman's rank correlation coefficients  $\rho$  for the uncertainty analysis.

Parameter	Karlsruhe		Cologne	
	$\rho$	p-value	$\rho$	p-value
$\lambda$	0.49	0.00	0.81	0.00
$\delta T_{GW}$	0.04	0.26	-0.08	0.03
$\delta d_{GW}$	-0.01	0.86	-0.02	0.53
$\delta bf$	0.04	0.24	0.07	0.03
$T_{Bld}$	0.31	0.00	0.27	0.00
$d_{Bld}$	0.79	0.00	0.03	0.38
$T_{SS}$	0.14	0.00	0.46	0.00
$d_{SS}$	0.08	0.03	0.06	0.09
$D_{SS}$	0.09	0.01	0.03	0.42
$l_{SS}$	0.00	0.99	-0.05	0.16
$c_{pSS}$	0.01	0.87	0.05	0.19
$V_{SS}$	-0.03	0.38	0.04	0.12
$r_L$	0.03	0.37	0.17	0.00
$P_{DH}$	0.03	0.34	-0.05	0.14
$r_d$	0.05	0.14	0.06	0.09
$T_{SW}$	-	-	0.07	0.05
$l_{SW}$	-	-	0.02	0.62
$D_{SW}$	-	-	0.05	0.18
$D_{DH}$	0.01	0.84	-	-
$l_{DH}$	0.07	0.05	-	-

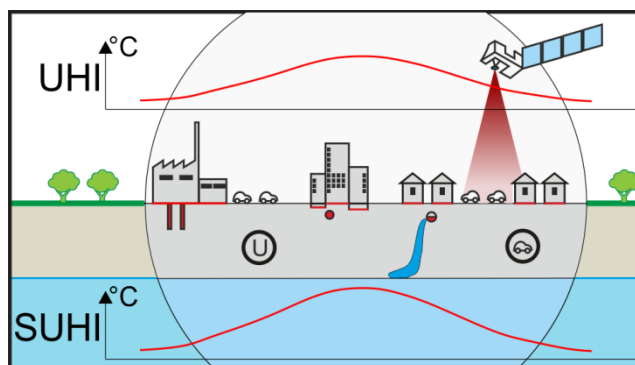
**Table S4.5.** Results and statistical significance of the Spearman's rank correlation coefficients  $\rho$  for the spatial variability analysis.

Parameter	Karlsruhe		Cologne	
	$\rho$	p-value	$\rho$	p-value
$T_{GS}$	0.68	0.00	0.57	0.00
$T_{GW}$	-0.28	0.00	-0.25	0.00
$d_{GW}$	-0.27	0.00	-0.25	0.00
$bf$	0.66	0.00	0.34	0.00
$\nabla T$	0.86	0.00	0.80	0.00

## 5. Linking Surface Urban Heat Islands with Groundwater Temperatures

*Reprinted with permission from 'Benz, S. A., Bayer, P., Goettsche, F. M., Olesen, F. S. & Blum, P. Linking Surface Urban Heat Islands with Groundwater Temperatures. Environmental Science and Technology 50, 70-78, 2016'. Copyright 2016 American Chemical Society.*

### Graphical Abstract



## **Abstract**

Urban temperatures are typically, but not necessarily, elevated compared to their rural surroundings. This phenomenon of urban heat islands (UHI) exists both above and below the ground. These zones are coupled through conductive heat transport. However, so far, the precise process is not sufficiently understood. Using satellite derived land surface temperature and interpolated groundwater temperature measurements, we compare the spatial properties of both kinds of heat islands in four German cities and find correlations of up to 80%. The best correlation is found in older, mature cities such as Cologne and Berlin. However, in 95% of the analyzed areas, groundwater temperatures are higher than land-surface temperatures due to additional subsurface heat sources such as buildings and their basements. Especially since local groundwater hot spots under city centers and under industrial areas are not revealed by satellite derived land-surface temperatures. Hence, we propose an estimation method that relates groundwater temperatures to mean annual land-surface temperatures, building density, and elevated basement temperatures. Using this method, we are able to accurately estimate regional groundwater temperatures with a mean absolute error of 0.9 K.



## 5.1. Introduction

In urban settlements, temperatures are typically, but not necessarily, elevated (30). This so-called urban heat island (UHI) phenomenon exists in all layers of modern cities such as atmosphere, surface and subsurface (SUHI). Various unfavorable issues are related to this phenomenon. The UHI on the surface is in part responsible for increased mortality rates during heat waves (169) and regional atmospheric pollution (170). In contrast, the investigation of SUHI indicated some favorable qualities such as economic and ecological advantages for the use of shallow geothermal energy (58). However, the increased groundwater temperatures also put stress on the underground ecosystems (68). Until now, all layers are typically investigated individually and information on the relationship between temperatures below and above ground is scarce.

The annual mean air temperature is closely related to the annual mean groundwater temperature due to conductive heat transport processes (9,148,149,216). The timely correlation of subsurface temperatures and air temperatures has previously been shown by Cheon et al. (217) for four urban settlements in South Korea between 1960 and 2010. In addition, results from a study by Menberg et al. (25) demonstrated that the surface air temperature has a considerable impact on subsurface and groundwater temperatures (GWT). However, the coupling process between air and ground temperatures is not yet fully understood (10,190).

In recent years, satellite derived land surface temperatures (LST) has evolved as a new technique for above ground temperature measurements. Its relationships to air temperature and ground surface temperatures imply a correlation, but are not yet precisely determined (18,92,139,218). However, satellite derived LST enables easy access to the spatial and temporal conditions of UHIs, and it is therefore frequently applied in cities in India (219), North America (220), central Europe (138), and worldwide (34). In contrast, the spatial description of SUHIs relies on the interpolation of GWT measurements in existing groundwater monitoring wells and boreholes (52,56,57), which is expensive and time-consuming. Especially in urban areas, groundwater wells are scarce and often too shallow (< 15 m below ground) for characterizing SUHIs.

Thus, many studies try to estimate GWT from above ground measurements such as surface air temperature (2 m temperature) and/or LST (221). Simulations of borehole temperatures from long term measurements of surface air temperature or vice versa indicate promising results (222-224). For example, Beltrami et al. were able to reproduce 98% of the variance in the borehole temperature using 70 years of surface air temperature in a rural area of Quebec (167). However, Huang et al. showed that measured urban borehole temperatures were significantly elevated compared to those predicted from meteorological time series in Osaka, Japan (225). These deviations are caused by anthropogenic heat sources such as buildings and their basements, sewage systems,

sewage leakage, subway tunnels, district heating networks, reinjection of thermal wastewater and geothermal energy systems (36,52).

Zhan et al. developed a one-dimensional (1-D) vertical heat transport model of Beijing's underground and reconstructed the subsurface thermal field at depths of 0.05 m, 0.40 m and 3.20 m from satellite derived LST data (226). The results were validated with soil temperatures measured at seven ground-based sites for which the overall average mean absolute error for one year of daily temperatures was 1.5 K. However, due to the time delay between above- and below-ground temperatures and the lack of satellite data, modeling of deeper GWT was impossible. Furthermore, Zhan et al. neglected below-ground anthropogenic heat fluxes into the subsurface (226), although recent studies showed that buildings and basements as well as elevated ground surface temperatures thermally dominate alterations of the urban underground (86,179). In cities with a shallow groundwater table, heat flow from buildings can be more than double the heat flow from elevated ground surface temperatures (86). Hence, for an improved estimation of urban GWT, the effects of buildings and urban infrastructure need to be considered. Furthermore, Zhu et al. demonstrated that advection from horizontal groundwater flow is a crucial heat transport mechanism in the subsurface of Cologne (177). It thus has to be considered when reconstructing the thermal environment of the urban underground.

The main objective of this study is to develop a method to estimate urban groundwater temperatures (GWT) from satellite-derived data. First, we compare urban heat islands (UHI) and subsurface urban heat islands (SUHI) in four German cities and analyze their dissimilarities in order to understand the interaction between the urban surface and subsurface. Spatial correlation and absolute differences between land surface temperatures (LST) and GWTs are carefully evaluated and the key drivers for the correlations are identified in an effort to analyze the interplay of UHI and SUHI. Second, we estimate annual mean urban GWT from annual mean satellite derived LST and building densities of the studied cities. For two cities this estimation method is then extended to include horizontal groundwater flow. These estimations allow for a first assessment of the SUHI and consequently the geothermal potential and groundwater ecological conditions, without the need for groundwater temperature measurements and data interpolation

## 5.2. Materials and Methods

Four German cities are chosen as study areas: Berlin, Munich, Cologne, and Karlsruhe (Table 5.1). From these, Karlsruhe stands out as being both the significantly smallest and youngest city. While Berlin, Munich and Cologne have more than 1 million inhabitants, Karlsruhe only has slightly more than 300,000. A single year of data for the three German megacities is analyzed; for Karlsruhe, two consecutive years (2011 and 2012) are analyzed, which also allows for the investigation of potential time-dependent changes. In the following, a brief overview of the hydrogeological properties and the GWT measurements of the studied cities is provided.

**Table 5.1.** General information on the four studied cities and years.

City	Berlin	Munich	Cologne	Karlsruhe	Karlsruhe
Year studied	2010	2009	2009	2011	2012
Year founded	1237	1158	38 B.C.	1715	1715
Area [km <sup>2</sup> ]	891.7 <sup>a</sup>	310.7 <sup>b</sup>	405.2 <sup>c</sup>	173.5 <sup>d</sup>	173.5 <sup>d</sup>
Population	3,460,700 <sup>a</sup>	1,364,200 <sup>b</sup>	1,020,000 <sup>c</sup>	303,000 <sup>d</sup>	307,000 <sup>d</sup>
Population density [km <sup>-2</sup> ]	3881	4391	2517	1746	1769
Analyzed area [Pixel]	928	437	147	89	88
Groundwater flow velocity <sup>e</sup> [m/d]	0.03–1.4	10-15	ca. 1.0	0.5 – 3.5	0.5 – 3.5
Groundwater depth [m]	1-10	0-22	3-22	2-10	2-10
Measurement depth [m]	15	1-23	20	5-14	5-14
Air temperature <sup>f</sup> [°C]	8.9	9.1	10.7	11.8	11.2

<sup>a</sup> Office for statistics, Berlin-Brandenburg (Amt für Statistik Berlin-Brandenburg); <sup>b</sup> Office for statistics, Munich (Statistisches Amt München); <sup>c</sup> Office for urban development and statistics, Cologne (Stadt Köln, Amt für Stadtentwicklung und Statistik); <sup>d</sup> Office for urban development, Karlsruhe (Stadt Karlsruhe, Amt für Stadtentwicklung); <sup>e</sup> Menberg et al. (2013)(36); <sup>f</sup> German Weather Service (Deutscher Wetterdienst, DWD).

### 5.2.1. Hydrogeology and Groundwater Temperature

In general, the seasonal temperature fluctuations get damped and show a certain time lag in the unsaturated zone, which depends on the effective thermal diffusivity (9). The penetration depth of this seasonal temperature fluctuation is also a function of the effective thermal diffusivity and typically ranges between 10-15 m (9). In the present study the focus is merely on annual mean temperatures that can be considered constant over certain depth. With increasing depth, however the groundwater temperature is governed by the geothermal gradient at the site. Consequently, annual mean temperatures

can be determined by either repeated measurements at shallow depths or a single measurement in a depth below the penetration depth of seasonal temperature fluctuation.

Berlin is located in the flat river Spree valley surrounded by two minor high points in the south and north. Both consist mainly of marly till and they are separated by the sandy glacial Spree valley. In this valley, the groundwater hydraulic head is between 1 and 10 m below the surface, while the groundwater table goes down to 40 m below surface under the two hills (227). In 2010, GWT was manually measured in 123 wells by the Department for Urban Development and the Environment at depths of 15 m below ground (145).

The subsurface of Munich consists mainly of gravel and cobble, and an unconfined aquifer (36,228). The groundwater level reaches up to 1 m below the surface in the north and close to the Isar River. Only in the far south of the city is the groundwater level at 18 m below the surface. In October 2009, groundwater temperatures (GWT) were measured in 492 wells by the Environmental Department of Munich, but only one meter below the groundwater surface. Hence, these measurements are most probably influenced by seasonal temperature oscillations since they were elevated for this month compared to the annual mean values. To emphasize this bias, the data for Munich is marked with an asterisk (2009\*) in the present study and is not considered in the derivation of the estimation method.

In Cologne, the shallow subsurface also consists mainly of gravels and sands (186), with the groundwater level at approximately 10 m below ground surface. GWTs were measured between September and October 2009 in 52 wells at 20 m below the surface using SEBA KLL-T logging equipment. The SUHI of Cologne was previously described comprehensively by Zhu et al.(177), Menberg et al. (36), and Benz et al. (86).

The shallow subsurface of Karlsruhe is also dominated by gravels and sands (184). However, here the average groundwater level is only at 5 m below ground. GWT were measured 2-3 meters below the groundwater surface in 82 wells by the Public Works Service of Karlsruhe. The wells are equipped with an Ackerman WPS05 data logger that records daily temperatures at 7 am. From these measurements, annual means for 2011 and 2012 were determined. The SUHI and the spatially variable subsurface anthropogenic heat fluxes of Karlsruhe have previously been described by Menberg et al. (145) and Benz et al. (86).

In the four studied cities, GWTs were interpolated with the same resolution as the available LST data (~1 km) using kriging in GIS (ESRI® ArcInfo™, Version 10.1). Mean temperatures and their standard deviations and measurement years are compiled in Table 5.2.

### 5.2.2. Land Surface Temperature

Eight-day mean land surface temperatures (LST) were taken from the **Moderate Resolution Imaging Spectroradiometer (MODIS)** level-3 products, MOD11A2 and MYD11A2 (15,89), as obtained from NASA's TERRA and AQUA satellites, courtesy of the NASA Land Processes Distributed Active Archive Center (LP DAAC), USGS/Earth Resources Observation and Science (EROS) Center, Sioux Falls, South Dakota, <https://lpdaac.usgs.gov> (14). They are composed of the daily 1-kilometer product of both satellites. TERRA passes the study areas daily at approximately 10:30 am and pm, and AQUA at approximately 01:30 am and pm. LST is retrieved only for clear sky observations. Out of these, the annual arithmetic mean was determined for all cities and years. MODIS-derived LSTs have been previously validated by several studies (16,90-92) on the basis of ground-based and heritage satellite measurements. The annual mean MODIS LSTs are also given in Table 5.2.

The UHI of Berlin was discussed by Dugord et al.(229). They found a UHI magnitude [max LST – mean LST] (142) of 8.7 K at 10 am and 3.2 K at 10 pm on August 14<sup>th</sup>, 2000. In contrast, the annual mean UHI magnitude of Berlin determined for the year 2010 is only 2.8 K. This low value is expected due to the weak surface UHI in winter (40) that lowers the annual UHI magnitude compared to the summer.

### 5.2.3. Estimation Method

In rural areas, annual mean GWTs are often estimated using surface air temperatures, ground temperatures or recently LSTs. However, in urban settlements, GWTs are also influenced by buildings (86) and other heat sources. Thus, it is impossible to estimate annual mean GWT using solely above-ground temperature. Hence, we combine annual mean LSTs and basement temperatures (BT) according to the building density (bd) to estimate annual mean groundwater temperatures (eGWT). Basements are typically not cooled (i.e. air conditioned), and thus LST was taken as the lower limit of eGWT leading to the following equation:

$$eGWT = Max \left\{ \begin{array}{l} LST \\ LST \cdot (1 - bd) + BT \cdot bd \end{array} \right. \quad (5.1)$$

Building densities were determined at the resolution of LST using building locations provided by OpenStreetMap (230) (Figure 5.4). In Germany, ground slab isolation was not implemented into construction regulation until the late 1990s (200), thus additional thermal insulation of buildings is not considered here. Basement temperatures were estimated as  $17.5 \pm 2.5$  °C following guidelines by the German Institute for Standardization (192). Additionally, building density and LST were assumed to be free of error.

To account for advective heat transport due to horizontal groundwater flow, the estimated groundwater temperature (eGWT) from satellite derived land surface temperature (LST) and building density is shifted according to the velocity and direction of the temperature signal in Cologne and Karlsruhe. At these locations, the flow can be considered constant over the entire study area. A detailed description of the calculation method can be found in the supplementary information.

**Table 5.2.** Summary of the main outcomes. Shown are annual mean values of groundwater temperatures (GWT), land surface temperatures (LST), and estimated groundwater temperatures without (eGWT) and with (eGWT<sub>FLOW</sub>), correlation and corresponding standard deviation (obtained via bootstrap method) and the accuracy of the estimated eGWT and eGWT<sub>FLOW</sub>.

City (Studied year)		Berlin (2010)	Munich (2009)	Cologne (2009)	Karlsruhe (2011)	Karlsruhe (2012)
Annual mean temperature and standard deviation [°C]	GWT	9.9 ± 0.8	11.9 ± 1.7	12.4 ± 1.0	13.0 ± 1.0	13.1 ± 1.0
	LST	8.7 ± 1.1	8.8 ± 0.8	11.7 ± 0.6	12.4 ± 0.8	11.1 ± 0.8
	eGWT	9.8 ± 1.6	10.2 ± 1.3	12.5 ± 1.0	13.6 ± 0.8	12.3 ± 0.9
	eGWT <sub>FLOW</sub>	-	-	12.6 ± 1.0	13.7 ± 0.7	12.5 ± 0.8
Correlation and standard deviation	GWT/LST	0.77 ± 0.01	0.74 ± 0.03	0.83 ± 0.03	0.48 ± 0.08	0.62 ± 0.07
	GWT/eGWT	0.74 ± 0.02	0.74 ± 0.03	0.81 ± 0.04	0.49 ± 0.08	0.56 ± 0.08
	GWT/eGWT <sub>FLOW</sub>	-	-	0.87 ± 0.02	0.57 ± 0.09	0.66 ± 0.07
RMSE [K]	GWT/eGWT	1.1	2.1	0.7	1.0	1.2
	GWT/eGWT <sub>FLOW</sub>	-	-	0.6	1.0	1.2
MAE [K]	GWT/eGWT	0.9	1.8	0.6	0.8	1.0
	GWT/eGWT <sub>FLOW</sub>	-	-	0.5	0.8	0.9

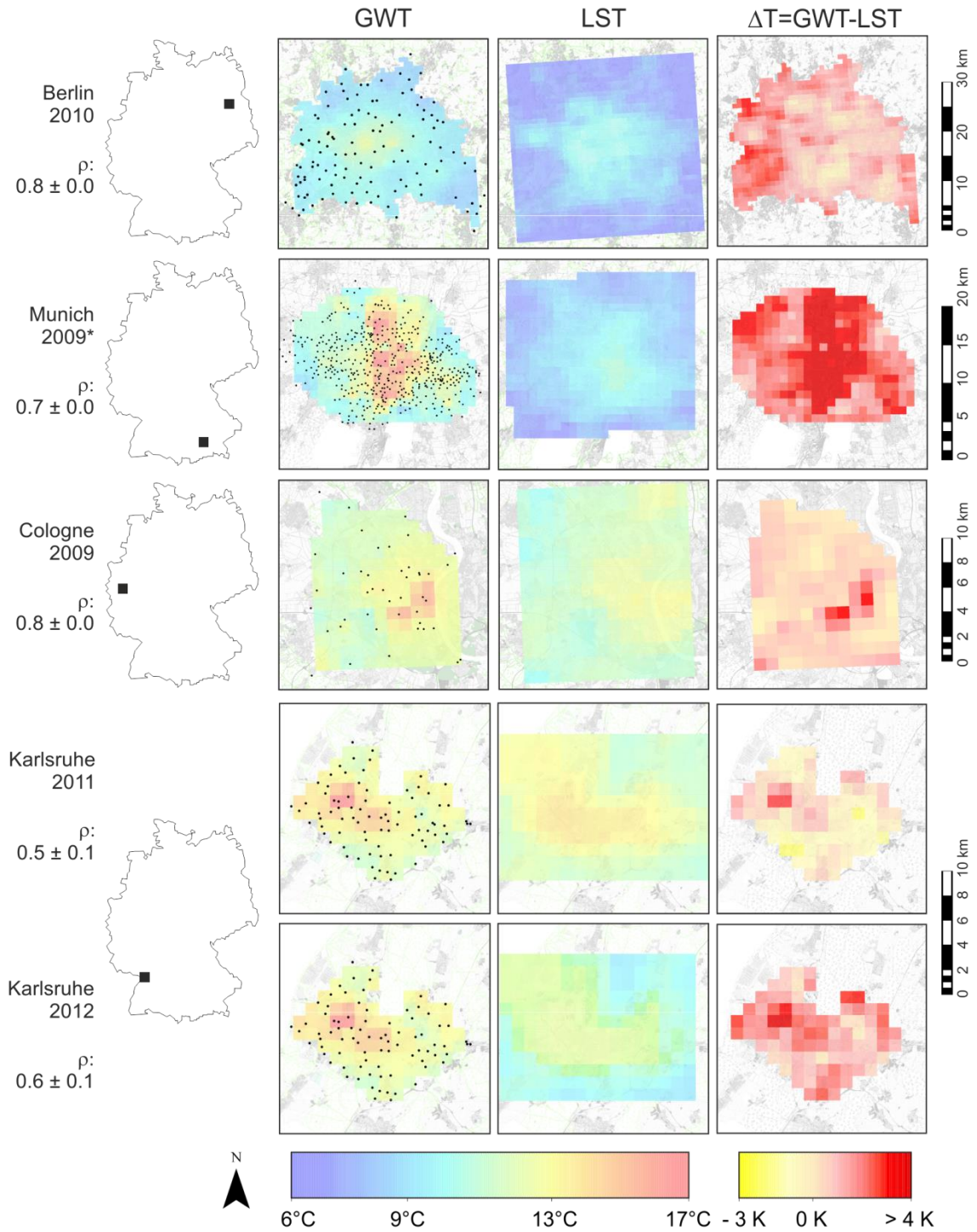


**Figure 5.1.** Geographical location, land surface temperature (LST), groundwater temperature (GWT), difference in temperatures ( $\Delta T$ ), and Spearman correlation ( $\rho$ ) for all analyzed cities

## 5.3. Results

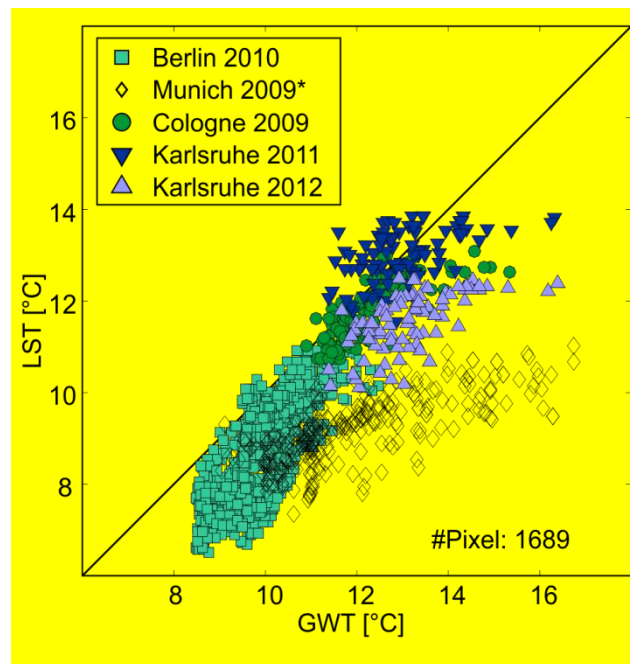
### 5.3.1. Comparison of Groundwater Temperature (GWT) and Land Surface Temperature (LST)

Table 5.2 summarizes the main outcomes of this study, including mean values for GWTs and LSTs. Of the four analyzed cities, Berlin is the coldest (GWT: 10 °C; LST: 9 °C) and Karlsruhe, 2011, the warmest (GWT: 13 °C; LST: 12°C). A map of GWTs, LSTs, and the difference  $\Delta T$  of both temperatures and the Spearman correlation coefficient between GWT and LST are shown in Figure 5.1. The correlation coefficient for all cities and years ranges from  $0.5 \pm 0.1$  for Karlsruhe, 2011, to  $0.8 \pm 0.0$  for Cologne, 2012. All p-values are below 0.01, indicating statistical significance. In the four studied cities, GWTs indicate local hotspots which are not observed in the satellite-derived LST data. In Berlin, Cologne and Karlsruhe, these hotspots are especially distinct and occur mainly under the city center where building densities are the highest. Moreover, in Cologne the hotspot can be directly linked to specific groundwater wells located next to the subway system and areas of local high sewage leakages (86,231). These anthropogenic heat sources affect GWT, but have no or only minor effects on above-ground temperatures. Similarly, the rise in GWT in the northwest of Karlsruhe is due to several existing reinjection wells of thermal wastewater (145). This anthropogenically caused hotspot is particularly noticeable in 2011, when the LST was significantly higher than its long-term average (Table 5.2). The mean annual GWTs do not respond to such short term changes in temperature, and therefore do not significantly deviate from their long-term mean. Still, the GWT close to the reinjection wells is about 3 K warmer than the LST over the entire area.

In Munich, the largest negative difference in temperature ( $\Delta T$ ) is due to the GWT measurements itself, which were taken in October only 1 m below the groundwater surface, resulting in significant seasonal bias. Hence, Munich is not considered much further in detail here. Still, it is an important case to demonstrate the large influence of shallow sampling depth and time.

For 95 % of the analyzed pixels of the four cities, GWT was higher than LST (Figure 5.2). Disregarding Karlsruhe, 2011, where LSTs were considerably higher than the long-term average, this number increases to 97.4 %. This confirms that the mean annual GWT is influenced by subsurface anthropogenic heat sources and therefore cannot solely be estimated from LST. However, in the four studied cities, long-term LSTs provide minimum temperatures for estimating annual mean urban GWTs (Eq. 5.1). On average, the measured GWTs are  $1.5 \pm 1.1$  K warmer than the satellite-derived LSTs.





**Figure 5.2.** Comparison of groundwater temperature (GWT) and land surface temperature (LST) for all four analyzed cities. In 95% of the analyzed 1689 pixels, the GWT is higher than the LST.

### 5.3.2. Influences on the Correlation of UHI and SUHI

Figures 5.3 a) to c) show the influence of city- and year-specific parameters on the correlation coefficient  $\rho$  between groundwater temperature (GWT) and land surface temperature (LST) (see Figure 5.1). Only parameters that correlate to  $\rho$  with more than 85 % and which have a p-value of  $< 0.1$  are shown. A list of all analyzed parameters is provided in Table S5.1 (Supplementary information). The largest correlation of 100 % was found for the measurement depth in the groundwater (Table S5.1). This agrees with the fact that the influence of short-term anthropogenic heat sources such as road works or newly constructed buildings, and the seasonal oscillations of the LST decreases with depth (9).

However, it is important to note that with increasing depth, groundwater temperatures are dominated by the natural heat flow, i.e. according to the geothermal gradient. Thus, the correlation between GWT and LST generally decreases with increasing measurement depth, depending on the vertical extension of the subsurface urban heat island (SUHI). The latter depends mainly on conductive heat transport and therefore on the age of the anthropogenic heat sources in the city. Accordingly, LST and GWT are better correlated for older and more mature urban settlements (Figure 5.3a). The size of the city also influences the observed relation between GWT and LST due to the fact that pristine groundwater laterally enters the urban aquifer and influences the observed groundwater temperatures at the city border. With increasing size of the city, a smaller percentage of

the area becomes affected and thus the influence on the overall correlation becomes minor (Figure 5.3b). However, due to the small sample size of four cities, major conclusions cannot be drawn and further research, including numerical simulations, should be performed to verify this interpretation.

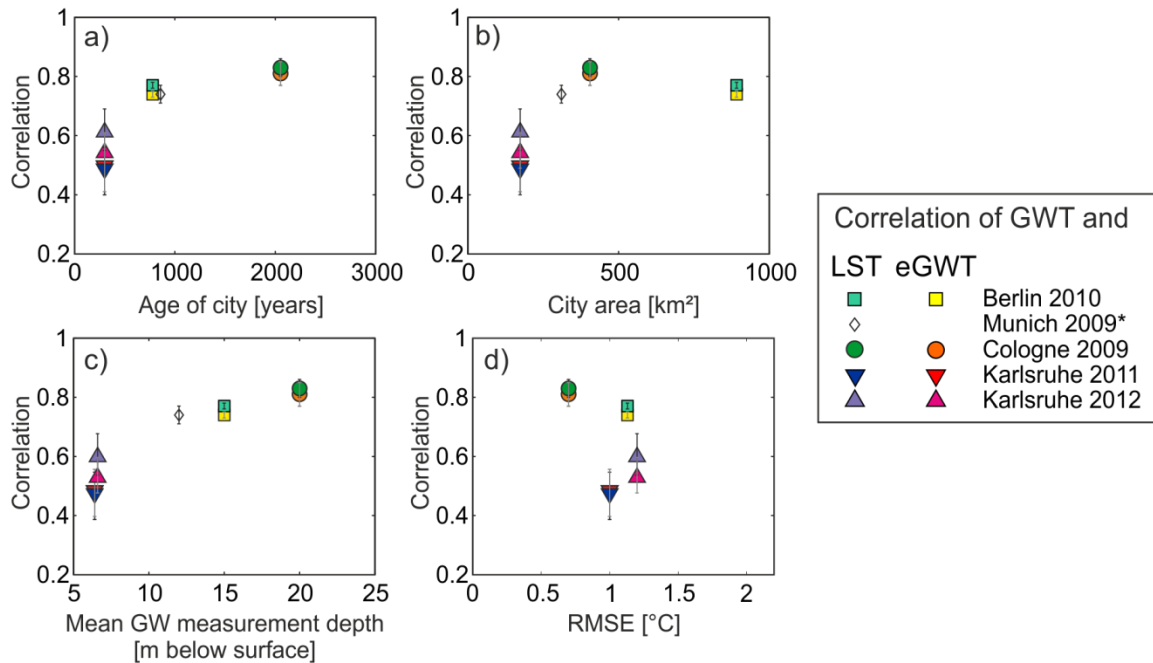


**Figure 5.3.** Spearman correlation coefficients ( $\rho$ ) of groundwater temperature (GWT) and land surface temperature (LST), as well as of GWT and estimated groundwater temperature (eGWT), are plotted against several city-specific parameters. Mean groundwater measurement depth and the age of the city influence the correlation of GWT and LST the most, while RMSE and spatial correlation of GWT and LST seem independent of each other.

### 5.3.3. Estimation of Groundwater Temperature

The estimated groundwater temperature (eGWT) was determined from land surface temperature (LST) and building density according to equation 5.1 (Table 5.2). In Figure 5.4, the building density, the groundwater temperature (GWT), the eGWT, and the difference between estimated and measured GWT ( $\Delta T$ ) are shown for three analyzed cities. Because of its seasonally influenced GWT measurements, Munich is excluded from the detailed discussion. In short, the results for Munich show a mean annual eGWT of 10.2°C, which is 1.7 K lower than the GWT measured in October 2009.

The correlation between GWT and eGWT shows no significant differences in the correlation between GWT and LST. Again, Karlsruhe – the smallest and youngest city – shows the lowest correlation, while Cologne – the oldest city with a study area roughly the size of Karlsruhe – has the largest correlation ( $\rho = 0.8$ ). The estimated eGWT map displays the hotspots in the city center of the three investigated cities (Figure 5.4).

However, as expected, the hotspot in the northwest of Karlsruhe, which is caused by local reinjections of thermal wastewater, cannot be determined using our proposed estimation method (Eq. 5.1). Similarly, the elevated GWT in the western part of Berlin cannot be identified either. Here, the building density is less than 2% and heat is most likely transported from the more densely populated city on top of the Tellow-Plateau into this western portion which is located in a valley (232). It is also possible that other unidentified heat sources cause this local hotspot.

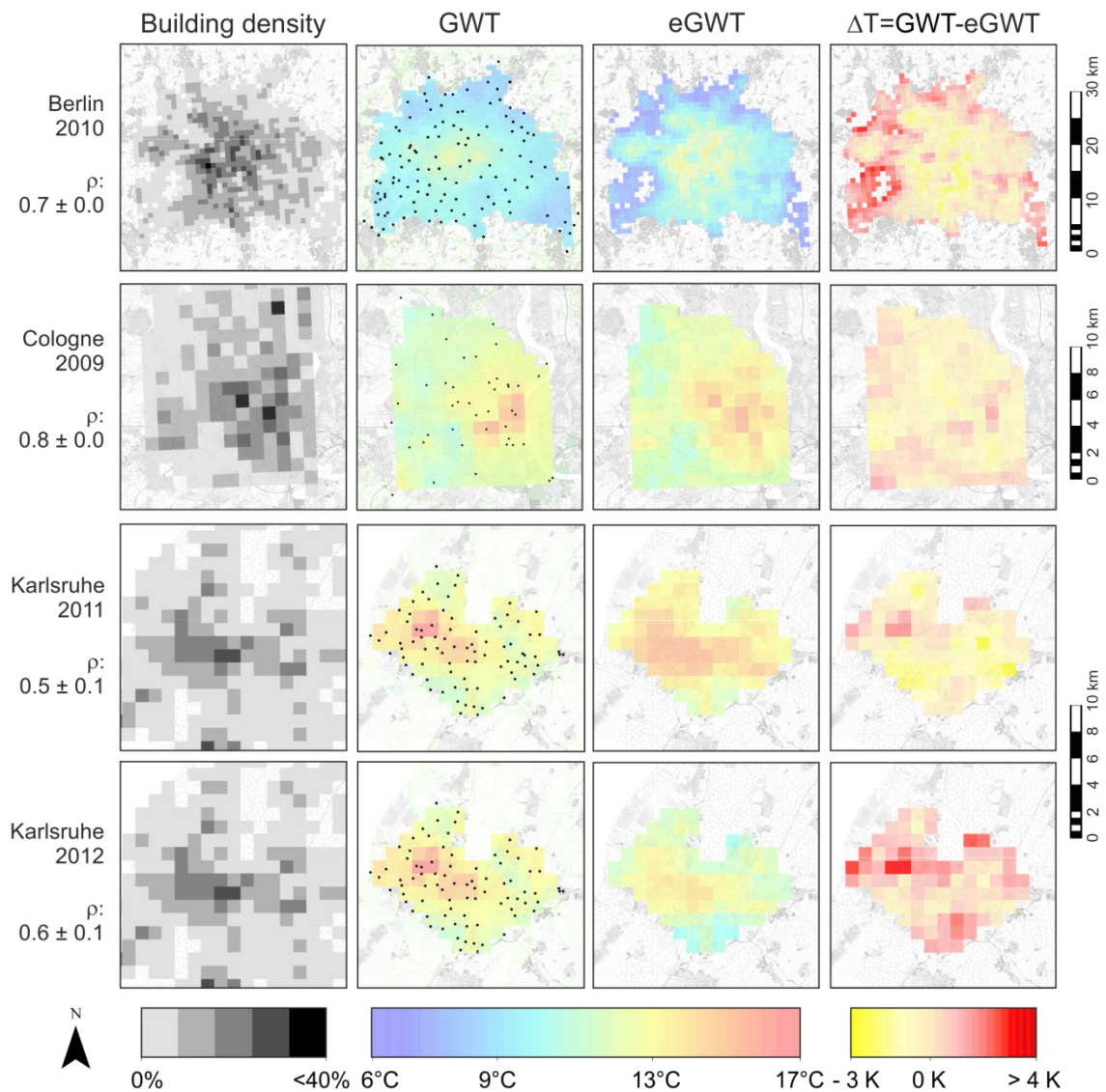


**Figure 5.4.** Building density, groundwater temperature (GWT), estimated groundwater temperature (eGWT), difference in temperatures ( $\Delta T$ ), and Spearman correlation ( $\rho$ ) for all analyzed cities and years. Well locations are shown with GWTs. A high (red)  $\Delta T$  represents a higher measured GWT and a lower (yellow)  $\Delta T$  represents a higher estimated eGWT. Building densities were derived from building locations as given by OpenStreetMap (230).

Overall, the deviation between measured and estimated GWT is minor and results in an average RMSE of 1.1 K (Figure 5.5). The error bars in Figure 5.5 represent the range

of estimated eGWT and stem from the assumed range of basement temperatures. Taking into account that the average range spans over  $0.3 \pm 0.2$  K, the estimated eGWT range deviates on average by  $0.6 \pm 0.6$  K from the measured temperatures.

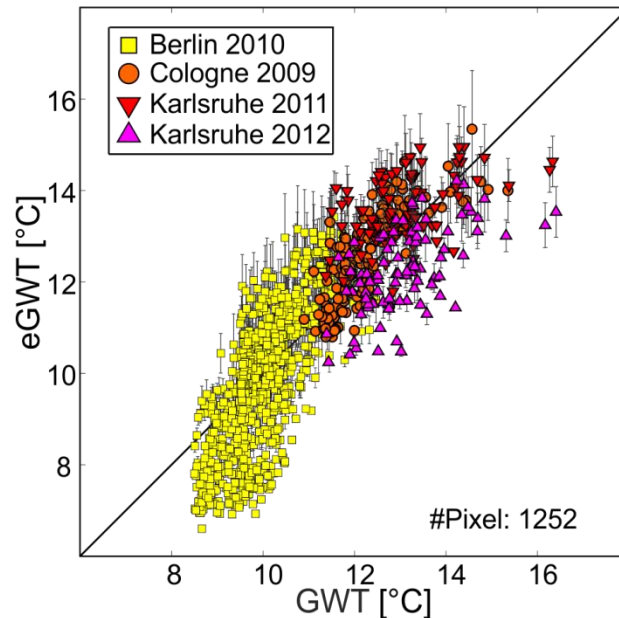


**Figure 5.5.** Comparison between measured groundwater temperatures (GWT) and estimated groundwater temperatures (eGWT). Error bars represent the assumed range due to uncertain basement temperatures. The overall mean absolute error is 0.9 K.

It is important to note that a good RMSE does not necessarily mean that GWT and LST correlate spatially (Figure 5.3d). Berlin, for example, has a significantly higher correlation than Karlsruhe. However, when comparing the absolute values of eGWT, estimations for Karlsruhe agree slightly better with measured GWTs. The relatively low correlation of GWT and LST in Karlsruhe can be explained by the anthropogenic hotspot in the northwest which is disproportionally weakening the correlation due to the small size of the city and the high velocity of the groundwater flow (see Table 5.1).

Hence, the GWT-LST correlation for Karlsruhe increases by up to 0.1 if the groundwater flow is taken into account. Figure 5.6 shows maps of the estimated groundwater temperature with flow ( $eGWT_{\text{FLOW}}$ ), as well as the temperature difference  $\Delta T = GWT - eGWT_{\text{FLOW}}$ . For both analyzed cities the correlation is improved by 6 to 10 % (see Table 5.2). In contrast, the RMSE between GWT and  $eGWT_{\text{FLOW}}$  is only slightly improved by less than 0.1 K compared to the estimation without groundwater flow (see Table 5.2 and Figure S5.1).

The mean absolute error (MAE) in this study is 0.9 K and therefore 0.7 K lower than in the study by Zhan et al., who utilized satellite-derived LST to reconstruct the subsurface thermal field of Beijing (226). However, they did not consider anthropogenic

heat sources such as buildings and only estimated ground temperatures within a maximum depth of 3.20 m. We assume the remaining deviations between estimated and measured GWT stem from other anthropogenic sources rather than elevated surface temperatures and buildings. Benz et al. found that 27% of the subsurface anthropogenic heat flow to the top of the groundwater surface in Cologne stems from sewage systems, sewage leakage, district heating networks, and the subway system, a considerable fraction that is not represented in our approach (86). For the year 2009, however, these heat sources alone could increase the groundwater temperature by approximately 0.1 K. Furthermore, this study considers only basements without insulation, which would result in an overestimation of GWT.

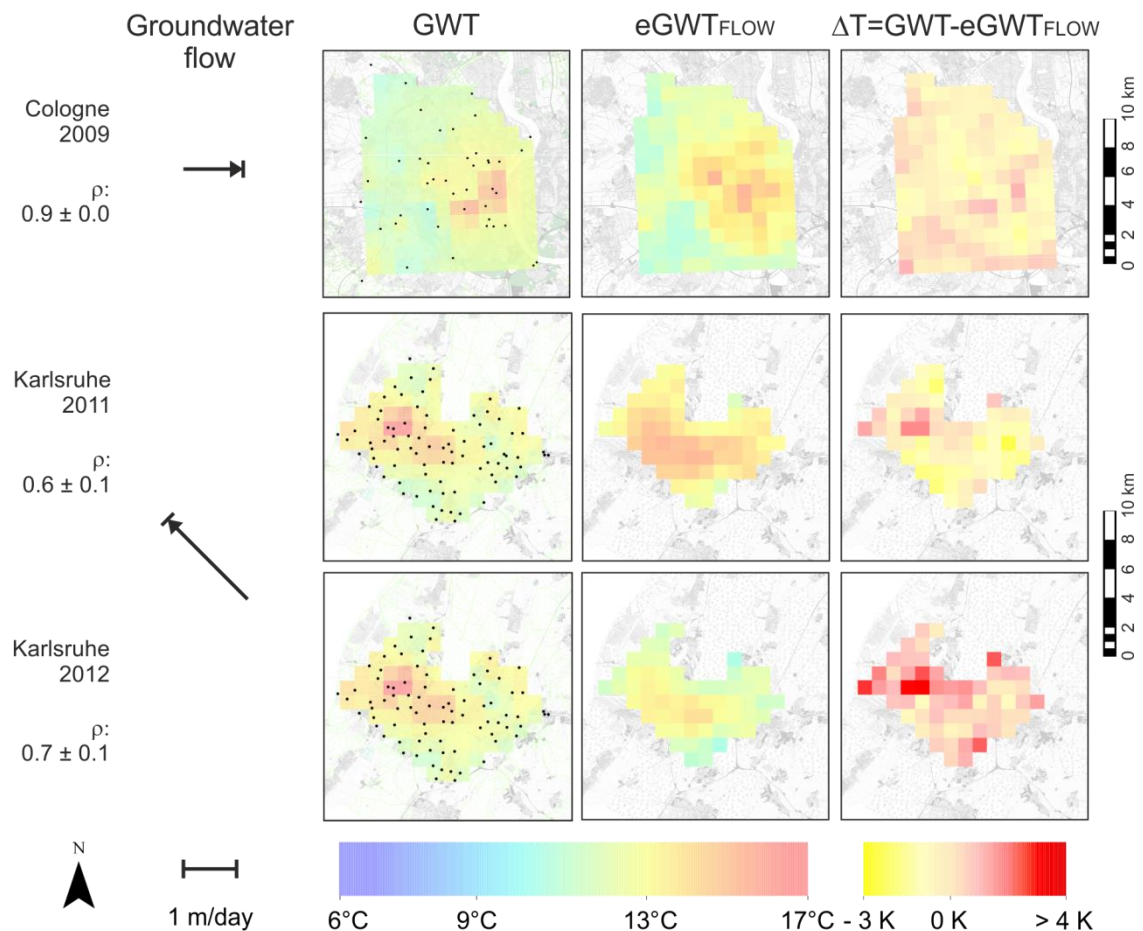


**Figure 5.6.** Groundwater flow, groundwater temperature (GWT), estimated groundwater temperature with groundwater flow (eGWT<sub>FLOW</sub>), the difference in temperatures ( $\Delta T$ ), and Spearman correlation ( $\rho$ ) for all analyzed cities.

Our proposed estimation method combines land surface temperatures (LST) with basement temperatures to estimate groundwater temperatures (GWT) and improves the mean absolute error to a value of 0.9 K. In comparison, estimating GWT from LST alone results in an underestimation of 1.5 K. Hence, we conclude that mean annual urban GWT



can be well approximated by combining satellite-derived LST data and building density data. The method allows investigations of subsurface urban heat islands (SUHI) and related issues such as geothermal potential (60) and groundwater quality where intensive GWT monitoring is not feasible. However, because the vertical extension of the SUHI appears to influence the correlation between above and below ground temperatures (Figure 5.3), we recommend applying the proposed estimation method to young megacities that are typically found in developing and BRIC (Brazil, Russia, India and China) countries. In principle, since LST and building density data are available from remote sensing, our method has the potential for large scale and even global estimations of urban GWTs.

## **Acknowledgements**

The financial support for S. Benz from the German Research Foundation (DFG) under grant number BL 1015/4-1 and the Swiss National Science Foundation (SNSF) under grant number 200021L 144288 is gratefully acknowledged. Furthermore, we thank Alexander Limberg and Thomas Scheider (Senate Department for Urban Development and the Environment, Berlin) Folker Dohr (Environmental Department, Munich), Stefan Jung (Karlsruhe Institute of Technology), Susanne Reimer and Friedhelm Fischer (Public Work Service Karlsruhe) for their valuable support with data and additional information. Finally, we would like to thank the two anonymous reviewers for their helpful comments.

## Supplementary Material

### Influences on the Correlation of UHI and SUHI

**Table S5.1.** Correlation coefficient and p-value between several year and city specific parameters, and the correlation coefficient of groundwater temperature (GWT) and land surface temperature (LST).

Parameter	Correlation coefficient	p-value
Age	0.9	0.08
Mean GWT	-0.6	0.35
Mean LST	-0.4	0.52
RMSE	-0.3	0.68
Area	0.9	0.10
Measurement depth	1.0	0.01
Population density	0.6	0.35

### Estimation of Groundwater Temperature with Groundwater Flow

To account for advective heat transport due to horizontal groundwater flow, the estimated groundwater temperature (eGWT) from satellite derived land surface temperature (LST) and building density is shifted according to the temperature flow velocity and direction. This is done for Cologne and Karlsruhe, where groundwater flow is roughly considered constant over the entire study area.

Heat advection is retarded in comparison to the groundwater flow velocity  $v_W$ . The velocity  $v_T$  of a temperature signal can be determined from the groundwater flow velocity  $v_W$  as follows (5):

$$v_T = \frac{v_W}{1 + R_T} \quad (S5.1)$$

With the thermal retardation factor  $R_T$  defined as

$$R_T = \frac{(1 - n) \cdot c_{V,S}}{n \cdot c_{V,W}} \quad (S5.2)$$



Here,  $n$  is the porosity of the aquifer, while  $c_{V,S}$  and  $c_{V,W}$  are the volumetric heat capacities of solid and water, respectively. The parameter values assumed for the estimation of  $v_T$  in Cologne and Karlsruhe can be found in Table S5.2.

**Table S5.2.** Assumed parameter values for the estimation of the advective heat transport velocity  $v_T = \begin{pmatrix} v_{T,x} \\ v_{T,y} \end{pmatrix}$  characteristic for Cologne and Karlsruhe.

Parameter	Name	Unit	Cologne		Karlsruhe	
			Mean	Uncertainty	Mean	Uncertainty
$v_W$	Groundwater flow velocity	m/a	(360,0)	-	(-500,500)	-
$n$	Porosity	%	20	5	20	5
$c_{V,W}$	Volumetric heat capacity of water	kJ/m <sup>3</sup> K	4150	-	4150	-
$c_{V,S}$	Volumetric heat capacity of solid	kJ/m <sup>3</sup> K	2150	50	2400	200
$D_T$	Thermal retardation factor	-	2.1	0.5	2.3	0.6
$v_T$	Velocity of advective heat transport	m/a	(120,0)	(20,0)	(-150,150)	(30,30)

To estimate groundwater temperature ( $eGWT_{FLOW}$ ) influenced by horizontal advection, the estimated  $eGWT$  is shifted according to the distance  $d_T = \begin{pmatrix} d_{T,x} \\ d_{T,y} \end{pmatrix}$  that the temperature signal traveled in one year. In the discretized map, this results in a new  $eGWT_{FLOW}$  of a pixel  $ij$  computed from the original temperature  $eGWT$  of certain pixel  $ij$  and the pixels surrounding it, according to the percentage of area covered by the shifted  $eGWT$ . For a resolution of  $1 \text{ km} \times 1 \text{ km}$  this can be expressed as

$$\begin{aligned}
 eGWT_{FLOW}(i, j) &= (1 - |\delta_{T,x}|)(1 - |\delta_{T,y}|) \cdot eGWT(i, j) \\
 &+ |\delta_{T,x}|(1 - |\delta_{T,y}|) \cdot eGWT\left(i - \frac{\delta_{T,x}}{|\delta_{T,x}|}, j\right) \\
 &+ (1 - |\delta_{T,x}|)|\delta_{T,y}| \cdot eGWT\left(i, j - \frac{\delta_{T,y}}{|\delta_{T,y}|}\right) \\
 &+ |\delta_{T,x}||\delta_{T,y}| \cdot eGWT\left(i - \frac{\delta_{T,x}}{|\delta_{T,x}|}, j - \frac{\delta_{T,y}}{|\delta_{T,y}|}\right)
 \end{aligned} \tag{S5.3}$$

using the dimensionless distance  $\delta_T = \begin{pmatrix} \delta_{T,x} \\ \delta_{T,y} \end{pmatrix} = \frac{d_T}{1 \text{ km}}$ .

In Cologne the groundwater flow was estimated with 360 m per year (Table 5.1 and S5.2) eastwards to the Rhine River (177). By means of equations S5.1 and S5.2, the horizontal velocity of a thermal signal was determined to be  $\begin{pmatrix} 120 \pm 20 \\ 0 \end{pmatrix}$  m/a. Hence, the new estimated groundwater temperature of a pixel (i,j) with horizontal flow ( $eGWT_{FLOW}$ ) is a mixed temperature composed of  $88\% \pm 2\%$  of the eGWT of the analyzed pixel (i,j) and  $12\% \pm 2\%$  of the eGWT of the pixel to its west (i-1,j) (see Eq. S5.3):

$$\begin{aligned} eGWT_{FLOW}(i,j) &= (0.88 \pm 0.02) \cdot eGWT(i,j) \\ &+ (0.12 \pm 0.02) \cdot eGWT(i-1,j) \end{aligned} \quad (S5.4)$$

In Karlsruhe a groundwater flow of approximately  $710 \approx \begin{pmatrix} -500 \\ 500 \end{pmatrix}$  m/a (Table 5.1 and S5.2) in a northwest direction was assumed, leading to a thermal flow velocity of  $\begin{pmatrix} -150 \pm 30 \\ 150 \pm 30 \end{pmatrix}$  m/a. Thus, the new estimated groundwater temperature with flow ( $eGWT_{FLOW}$ ) of a pixel (i,j) is composed of the eGWT of the original pixel (i,j), the eGWT of the pixel to the east (i+1,j), the eGWT of the pixel to the south (i,j-1), and the eGWT of the pixel to the southeast (i+1,j-1) in the following way (see Eq. S5.3):

$$\begin{aligned} eGWT_{FLOW}(i,j) &= (0.85 \pm 0.03)^2 \cdot eGWT(i,j) \\ &+ (0.15 \pm 0.03)(0.85 \pm 0.03) \cdot eGWT(i+1,j) \\ &+ (0.85 \pm 0.03)(0.15 \pm 0.03) \cdot eGWT(i,j-1) \\ &+ (0.15 \pm 0.03)^2 \cdot eGWT(i+1,j-1) \end{aligned} \quad (S5.5)$$

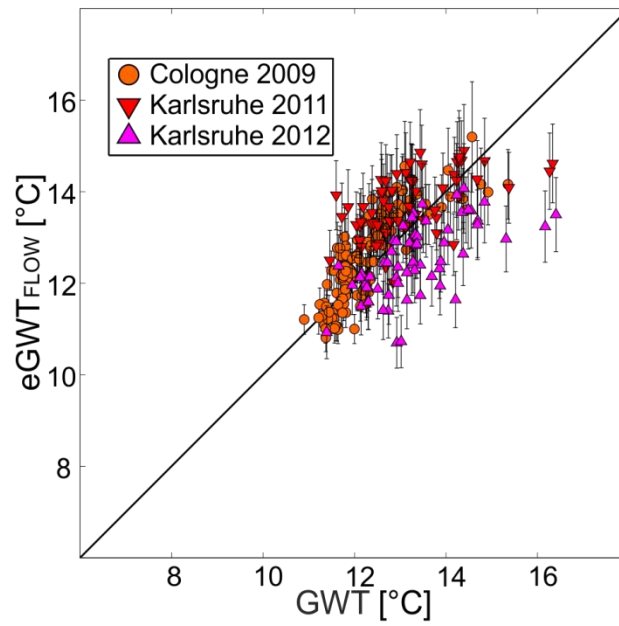


**Figure S5.1.** Comparison between measured groundwater temperatures (GWT) and estimated groundwater temperatures including horizontal groundwater flow (eGWT<sub>FLOW</sub>). Error bars represent the assumed range due to uncertain basement temperatures and temperature flow velocities.



## 6. Synthesis

### 6.1. Estimating Urban Groundwater Temperatures

In this thesis two estimation techniques for shallow groundwater temperatures (GWT) were introduced:

- In Chapter 2 the global offset between GWT and satellite derived land surface temperature (LST) has been analyzed and linked to evapotranspiration and snow cover. Considering these two factors only, global shallow groundwater temperatures were estimated. From this point forward GWT estimated with this method will be referred to as  $eGWT_{rural}$ .
- In Chapter 5 the spatial properties of surface and subsurface urban heat islands were compared in four German cities. Under the assumption that LST and GWT are equal in rural, undisturbed areas, differences could be linked to building density. Hence, an estimation method that relates urban groundwater temperatures to mean annual LST, building density, and elevated basement temperatures was proposed. From this point forward GWT estimated with this method will be referred to as  $eGWT_{urban}$ .

As the study in Chapter 5 (study 2) was published before the study in Chapter 2 (study 3), the influence of snow and evapotranspiration on urban GWTs has not yet been discussed. Thus, the following Chapter will compare both methods at the example of three German cities. Furthermore it will illustrate an additional estimation technique of urban GWTs based on LST, snow, evapotranspiration, building density, and elevated basement temperatures. From this point forward GWT estimated with this method will be referred to as  $eGWT_{combined}$ .

#### 6.1.1. Materials and Methods

All three estimation techniques are applied to Berlin, Cologne and Karlsruhe. For Berlin and Cologne the single year GWT datasets introduced in Chapter 5 were used and annual mean data of the same year is used for all estimations. In Karlsruhe the multi-year mean GWT (Chapter 2, Table S2.1) is estimated using 10 year mean (01/2005 – 12/2014) data.

#### Data

To determine mean land surface temperatures (LST), MODIS daily products MOD11A1 and MYD11A1 (15,89) were used. They are obtained from NASA's TERRA

and AQUA satellites, courtesy of the NASA Land Processes Distributed Active Archive Center (LP DAAC), USGS/Earth Resources Observation and Science (EROS) Center, Sioux Falls, South Dakota, <https://lpdaac.usgs.gov> (14). Each satellite observes the entire planet twice daily, giving four LST measurements a day. Because LSTs are only retrieved for clear sky observations, they have a bias towards non cloudy days. To correct for this bias in regards to the seasonal variations of cloud cover, the appropriate (multi-)annual mean was determined from monthly mean temperatures for each analyzed city. This was performed using Google Earth Engine (93) and was exported in a resolution of approximately  $1 \text{ km} \times 1 \text{ km}$  ( $0.009^\circ \times 0.009^\circ$ ) (Fig. 6.1).

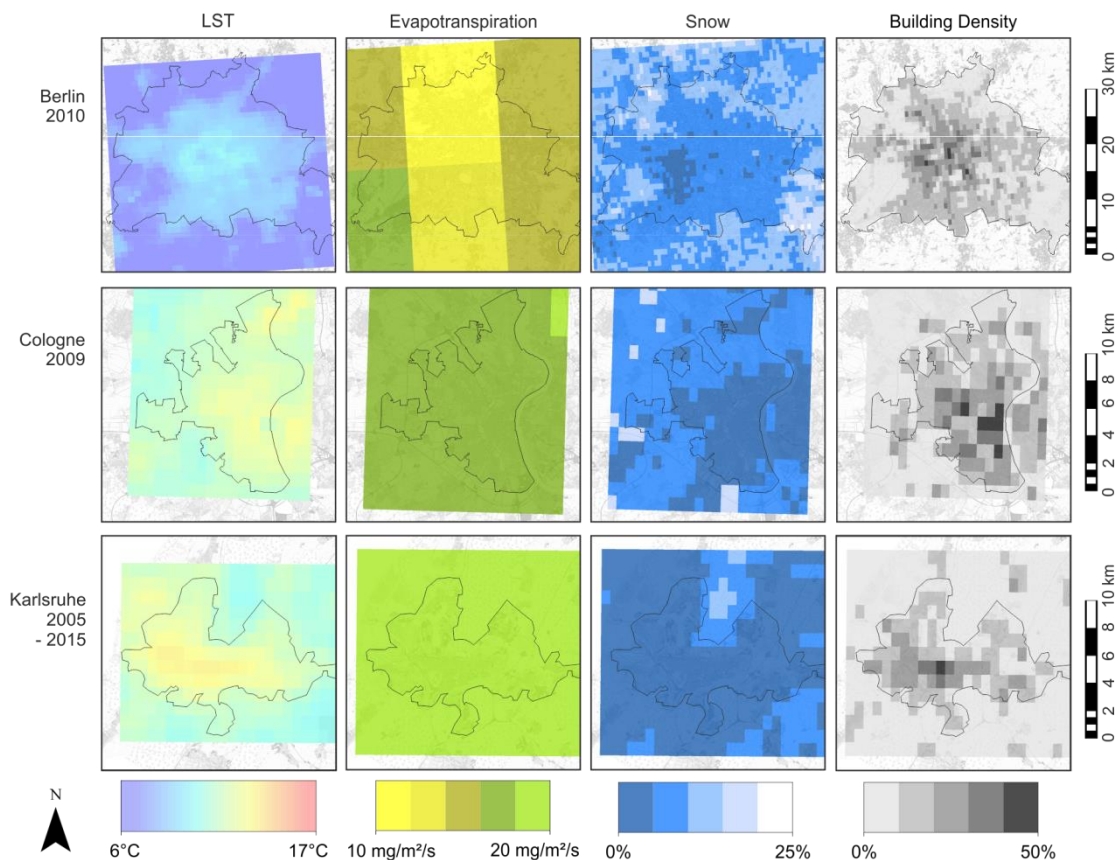


**Figure 6.1.** Land surface temperature (LST), evapotranspiration, percentage of snow days and building density of Berlin, Cologne and Karlsruhe.

Evapotranspiration (ET) data was gathered from the Noah 2.7.1 model in the Global Land Data Assimilation System (GLDAS) data products Version 1 (94) (spatial resolution:  $0.24^\circ$ ). Mean ET for the analyzed timeframe of each city was determined using Google Earth Engine (93) and was exported in a resolution of approximately  $1 \text{ km} \times 1 \text{ km}$  resolution (Fig. 6.1).

Information on snow days was derived from MODIS Terra and Aqua Snow Cover Daily L3 Global 500 m Grid, Version 5 (99), products MOD10A1 and MYD10A1, courtesy of the National Snow and Ice Data Center (NSIDC). Using Google Earth Engine

(93), the percentage of snow days in the analyzed timeframe was determined by dividing the number of days classified as “snow” by the sum of the days classified as either “no snow” or “snow”. For each city data was exported in a  $\sim 1 \text{ km} \times 1 \text{ km}$  resolution (Fig. 6.1).

Building densities were determined at the resolution of LST using building locations provided by OpenStreetMap (230) (Fig. 6.1). Basement temperatures were estimated as  $17.5 \pm 2.5 \text{ }^\circ\text{C}$  following guidelines by the German Institute for Standardization (192).

### Estimation Techniques

All GWT estimations were performed in GIS (ArcMap 10.1) and compared using Matlab R2016a.

The rural estimation method has been established in Chapter 2. It relates global shallow GWTs to satellite derived LST, evapotranspiration (ET) and snow cover, in form of percentage of snow days. The estimation is performed via the following fit:

$$\begin{aligned}
 eGWT_{rural} = & LST \\
 & + (3.5 \pm 0.2) \cdot 10^4 \text{ K} \frac{\text{m}^2 \cdot \text{s}}{\text{kg}} \cdot ET \\
 & + (6.6 \pm 0.3) \text{K} \cdot \text{snow days}
 \end{aligned} \tag{6.1}$$

In Chapter 5 an urban estimation technique is introduced. It relates urban GWTs to LST, building density (bd) and basement temperatures (BT):

$$eGWT_{urban} = \text{Max} \left\{ \begin{array}{l} LST \\ LST \cdot (1 - bd) + BT \cdot bd \end{array} \right. \tag{6.2}$$

One of the main assumptions of this urban estimation technique is that annual mean LST and GWT are equal for rural, undisturbed areas. In reality however, snow cover and evapotranspiration offset GWT and LST. Rural GWT is generally elevated compared to LST and has been estimated in equation 6.1. Here both methods are combined and urban GTWs are estimated from estimated rural groundwater temperatures ( $eGWT_{rural}$ ), building density (bd) and basement temperatures (BT).

$$eGWT_{combined} = \text{Max} \left\{ \begin{array}{l} eGWT_{rural} \\ eGWT_{rural} \cdot (1 - bd) + BT \cdot bd \end{array} \right. \tag{6.3}$$

### 6.1.2. Results and Discussion

Maps of all estimated as well as measured and interpolated GWTs are displayed in Figure 6.2. The comparison of absolute temperatures for all analyzed cities and methods is given in Figure 6.3. While GWTs Karlsruhe and Cologne are estimated most precise using the rural approach (Table 6.1; RMSE of 0.45 K or rather 0.50 K); mean temperatures in Berlin are reflected best by the combined method (RMSE: 0.96 K). Only methods that consider building location are able to accurately predict the location of urban hot spots. However, the combined method tends to overestimate temperatures within the city center where building density is highest by approximately 0.8 K. This is most likely due to insulation, which has not been taken into account. As the urban method neglects to consider the natural offset between GWT and LST, both errors (natural offset and insulation) balance each other out for the analyzed cities. For all cities combined, the rural technique estimates GWTs with an RMSE of 1.03 K, the urban method with an RMSE of 1.37 K and the combined method with an RMSE of only 0.93 K. Additional research on the influence of insulation and the implementation of groundwater flow (see Chapter 5) is necessary to further improve this method.

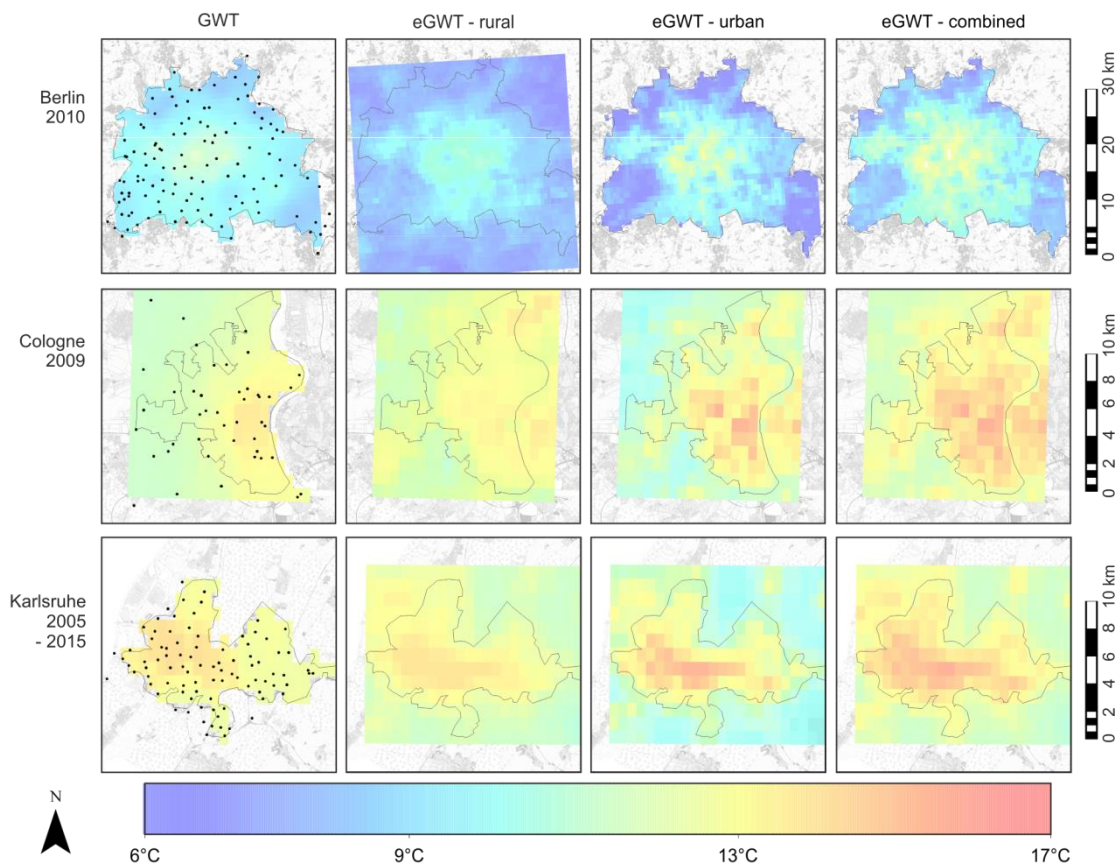


**Figure 6.2.** Groundwater temperature (GWT), estimated GWT using the method for undisturbed, rural areas (eGWT – rural; Chapter 2), estimated GWT using the method for disturbed, urban areas (eGWT – urban; Chapter 2), and estimated GWT using a combination of both methods (eGWT– combined; Chapter 6) for all analyzed cities.



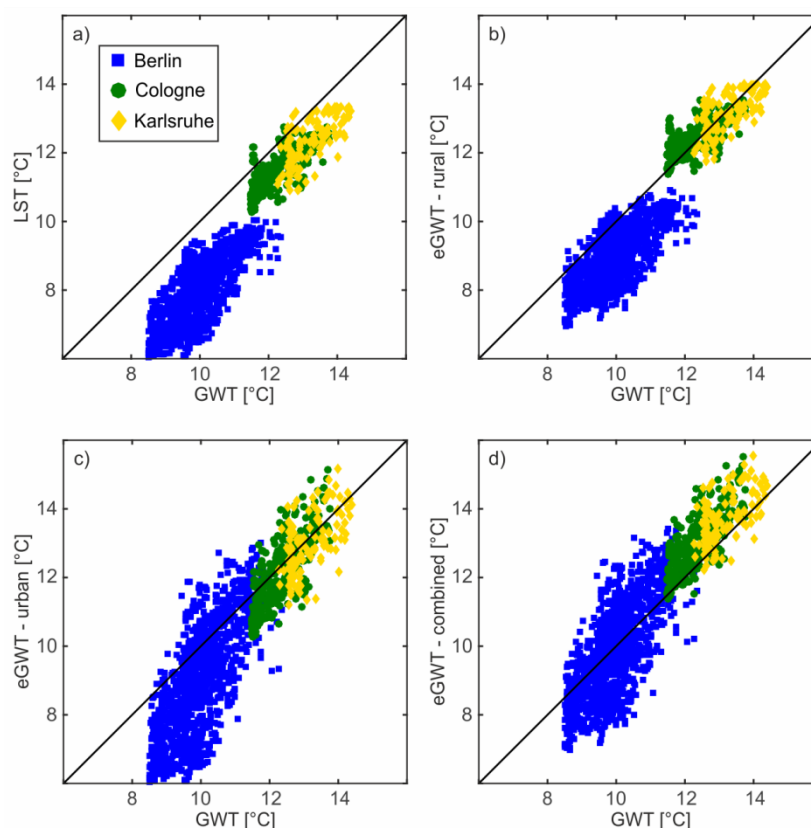


**Figure 6.3.** Comparison of a) groundwater temperature (GWT) and land surface temperature (LST), b) GWT and estimated GWT for undisturbed, rural areas (eGWT – rural; Chapter 2), c) GWT and estimated GWT for disturbed, urban areas (eGWT – urban; Chapter 5), and d) GWT and estimated GWT using a combination of both methods (eGWT – combined; Chapter 6).

**Table 6.1.** Summary of the main outcomes. Given are the Pearson correlation coefficient, the root mean square error (RMSE) and the mean absolute error (MAE) in comparison to interpolated GWT measurements for all analyzed cities and estimation techniques.

City (Studied year)		Berlin (2010)	Cologne (2009)	Karlsruhe (2005-2015)
RMSE [K]	GWT/LST	2.10	0.88	1.01
	GWT/ $eGWT_{rural}$	1.14	0.45	0.50
	GWT/ $eGWT_{urban}$	1.51	0.73	0.73
	GWT/ $eGWT_{combined}$	0.96	0.86	0.82
MAE [K]	GWT/LST	2.01	0.80	0.88
	GWT/ $eGWT_{rural}$	1.00	0.37	0.41
	GWT/ $eGWT_{urban}$	1.21	0.61	0.60
	GWT/ $eGWT_{combined}$	0.77	0.70	0.65

## 6.2. Summary and Conclusion

The thermal regime of the shallow underground plays a crucial role in various fields of modern sciences. They are habitat, provide drinking water, and serve as sustainable energy source all in one. Yet we know only little about their thermal conditions and the influence modern humanity has on them.

Thus, the first aim of this study is to contribute to a better understanding of global shallow groundwater temperatures (GWT) in undisturbed, rural areas. 2,548 measurement points in 29 countries are compiled and reveal characteristic trends in the offset between shallow groundwater temperatures and satellite derived land surface temperatures (LST). For 83 % of all measurement points, GWTs are warmer than LST; the average offset  $\Delta T = GWT - LST$  is  $1.2 \pm 1.5$  K. The data indicates that GWTs are elevated compared to LSTs for coldest and warmest temperatures. These differences are caused by two distinct effects: in areas with lower temperatures, snow cover insulates warm groundwater temperatures during the winter months; in warmer and more humid areas, latent heat flux caused by evapotranspiration factors into the surface energy balance, thus decreasing LSTs. Considering these two processes only, global shallow groundwater temperatures were estimated with a root mean square error of 1.4 K. However, GWT anomalies caused by other effects such as geothermal hotspots, fossil groundwater and last but not least subsurface urban heat islands were not resolved with the presented method.

Further aims of this study are related to the human impact on local temperatures. One focus is to quantify said impact for different compartments (air, surface and groundwater) over a large, country wide area, in this case Germany. A universal parameter, the anthropogenic heat intensity (AHI), is introduced. It can be applied to a broad variety of different temperature measurements such as groundwater temperatures (GWT), land surface temperatures (LST), and surface air temperatures (SAT). Following the commonly used urban heat island intensity (max. urban temperature - rural background temperature) it is determined by subtracting median rural background temperatures  $T_r$  from individual temperatures  $T$ , recorded at each measurement point (GWT and SAT) or pixel (LST), regardless of land cover and land use. Here nighttime light was used as an indicator for rural areas, while elevation and distance to the analyzed pixel or measurement point are considered to find appropriate background measurement locations. The main drivers of AHI are analyzed and it becomes apparent that while population density has only a minor effect, AHI grows with increasing nighttime lights and decreases with increasing vegetation. At the surface of Germany, the highest annual mean AHI of 4.5 K is found at an open-pit lignite mine near Jülich, followed by the cities Munich, Düsseldorf and Nuremberg with anthropogenic heat intensities of more than 4 K. The top 15 surface AHI locations also include pixels in smaller cities (e.g. Wolfsburg: surface AHI of 3.7 K, 120,000 residents; Saarlouis: surface AHI of 3.4 K, 40,000 residents) known for their industrial sites. This indicates that not only urban heat islands exist, but industrial heat islands as well. Overall surface AHI greater than zero and thus urban heat

islands are observed in communities with a population of 5,000 residents and can be predicted for communities down to 3,000 residents.

Furthermore, when comparing the different compartments (air, surface and groundwater) SAT appears least vulnerable to human activity while GWT is most vulnerable.

Subsequent to the identification of non-urban anthropogenic heat anomalies, another aim is to better understand the spatial properties and sources of subsurface urban heat islands (SUHI). Thus, a 2D statistical analytical heat flux model is developed and successfully applied to the cities of Karlsruhe and Cologne, Germany. The heat flux model gives a spatial representation of the vertical subsurface anthropogenic heat fluxes into urban aquifers. Results show that district heating pipes are the dominant source of anthropogenic heat fluxes into the subsurface (AHF<sub>S</sub>) with average values of more than 60 W/m<sup>2</sup>, more than one order of magnitude higher than all other heat sources. Only sewage pipes and basements reaching into the groundwater are the cause of equally extraordinary heat fluxes with maximal values of 40 W/m<sup>2</sup> and 14 W/m<sup>2</sup>, respectively. These can be found in Karlsruhe, where the groundwater level is on average only 5.4 m below the subsurface. In the studied western part of Cologne, with a mean groundwater depth of 10.2 m, buildings and the sewage system do not reach into the groundwater. Thus, their fluxes show only minor spatial variability. Furthermore, in Cologne, the average total AHF<sub>S</sub> is lower ( $0.39 \pm 0.12$  W/m<sup>2</sup>) and has a lower spatial variability ( $\pm 0.38$  W/m<sup>2</sup>) than the average total AHF<sub>S</sub> in Karlsruhe ( $1.10 \pm 0.73$  W/m<sup>2</sup>; spatial variability of  $\pm 1.49$  W/m<sup>2</sup>). While dominating the local anthropogenic fluxes, the district heating network is insignificant for the citywide AHF<sub>S</sub> budget in both cities. Heat from buildings ( $1.51 \pm 1.36$  PJ/a in Karlsruhe;  $0.31 \pm 0.14$  PJ/a in western Cologne) and elevated GST ( $0.34 \pm 0.10$  PJ/a in Karlsruhe;  $0.42 \pm 0.13$  PJ/a in western Cologne) are dominant contributors of the anthropogenic heat flow into the urban aquifer. In Karlsruhe, buildings are the source of 70 % (in Cologne 30 %) of the annual heat transported into the groundwater, which is mainly caused by buildings reaching into or close to the groundwater. A covariance analysis confirmed these findings. Hence, basement depth is the most influential factor to citywide heat flow in cities with a high groundwater level. The spatial distribution of fluxes, however, is mostly influenced by the thermal gradient of the unsaturated zone. A cold GWT combined with a high surface temperature, as well as a high groundwater level, results in elevated fluxes like in the east of Karlsruhe. Overall,  $2.15 \pm 1.42$  PJ and  $0.99 \pm 0.32$  PJ of thermal energy are annually transported into the groundwater of Karlsruhe and western Cologne due to AHF<sub>S</sub>. This is sufficient to sustainably cover 32 % and 9 % of the annual residential space heating demand of Karlsruhe and western Cologne, respectively

Finally, this study aims to answer the question whether above and below ground urban heat islands are linked and to develop a method to estimate urban GWT from satellite-derived data. This estimation allows for a first assessment of the subsurface urban heat island (SUHI) and consequently the geothermal potential and groundwater ecological conditions, without the need for groundwater temperature measurements and data

interpolation. Previous findings within this thesis demonstrate that rural undisturbed GWTs can be linked to satellite derived land surface temperatures (LST) via evapotranspiration and snow cover. However, in urban settlements, GWTs are also influenced by heated buildings and other sources of AHFs. Here, surface urban heat islands (UHI) and subsurface urban heat islands (SUHI) are first compared in four German cities. Their dissimilarities are analyzed in order to understand the interaction between the urban surface and subsurface. The correlation coefficient for all cities and years ranges from  $0.5 \pm 0.1$  for Karlsruhe, 2011, to  $0.8 \pm 0.0$  for Cologne, 2012 and can be improved if groundwater flow is taken into account.

In the four studied cities, GWTs indicate local hotspots which are not observed in the satellite-derived LST data. In Berlin, Cologne and Karlsruhe, these hotspots are especially distinct and occur mainly under the city center where building densities are the highest. Moreover, in Cologne the hotspot can be directly linked to specific groundwater wells located next to the subway system and areas of local high sewage leakages. Similarly, the rise in GWT in the northwest of Karlsruhe is due to several existing reinjection wells of thermal wastewater. These anthropogenic heat sources affect GWT, but have no or only minor effects on above-ground temperatures.

Annual mean urban GWT are then estimated from annual mean satellite derived LST, evapotranspiration, and snow days as well as building densities. The proposed method is tested for Berlin, Cologne and Karlsruhe estimates GWT with a root mean square error of 0.9 K. In comparison, when matching GWTs directly with LSTs the RMSE is 1.9 K.

### **6.3. Perspective**

Within this study it was shown that mean annual groundwater temperatures (GWT) can be well approximated by combining land surface temperatures (LST) with other satellite-derived data such as evapotranspiration, snow cover and building density. The novel method allows investigations of subsurface urban heat islands (SUHI) and related issues such as geothermal potential and water quality where intensive GWT monitoring is not feasible. However, as the urban estimation technique has so far only been applied to central European cities, it must be applied to cities in different climate zones before definite conclusions can be drawn. Especially its usefulness in young mega-cities that are typically found in developing and BRIC (Brazil, Russia, India and China) countries needs further validation. In principle, as all used data are available from remote sensing, the proposed method has the potential for large scale and even global estimations of GWTs in both urban and undisturbed regions. However, for an improved estimation the heat impact of urban structures has to be analyzed in more detail (233). Additionally, once the temporal aspects of LST and GWT are linked, GWT, and thus river temperature (149) forecast becomes also plausible.

In Chapter 3 of this thesis the annual mean anthropogenic heat intensity (AHI) is introduced, which quantifies the human impact on temperatures for a large scale temperature datasets such as LST. Future work should also analyze global datasets.

Analyzing the differences in daytime and nighttime surface AHI as well as its annual variation will help to classify surface urban heat islands and thus help to develop appropriate mitigation strategies for different types of urban heat islands. Additionally, AHIs give the opportunity for detailed, 3-D analysis of anthropogenic heat islands, both urban and industrial, for large scale studies and also case specific studies.

Furthermore, the spatial heat flux model presented in Chapter 4 enables development of a sustainable thermal energy management tool. By combining the introduced sustainable geothermal potential with heating demand (234) and the capacities of borehole heat exchangers, a GIS-based sustainable geothermal energy concept becomes possible. Additional insight can be gained by quantifying the temporal variation of all anthropogenic heat fluxes into the subsurface. However, several economic, technical, behavioral, and political challenges need to be overcome before the goal of urban sustainability can truly be reached (67).



## Acknowledgements

*Cui honorem, honorem.*

I would like to thank Prof. Dr. Philipp Blum for the opportunity to do a PhD, for the guidance, for the time, for the help, sometimes for just letting me be, and for teaching me how to “science”. Thank you very much!

I would like to thank Prof. Dr. Peter Bayer for always being constructive and for making my research just better.

I would like to thank Prof. Dr. Nico Goldscheider for being the second reviewer and for betting on my success.

I would like to thank Dr. Kathrin Menberg for the tremendous help at the beginning of my time as a PhD student and for sharing your knowledge and experience.

I would like to thank Dr. Manuela Hübsch for decorating the most perfect office the world has ever seen and for sharing it with me.

I would like to thank the “Schnittchengruppe” and all its honorary members. You are awesome. I had a lot of fun.

I would like to thank the Engineering Geology and Hydrogeology working groups. I’ve really enjoyed working (and, well, not-working) with you.

I would like to thank my family; my mother; my siblings. Just thanks, no specific reasoning.

And...

...I would like to thank everyone who listened to me cheering and/or whining about everything and at all times...

... But you're not gonna read this anyway...

... ☺



## Declaration of Authorship

### Study 1 (Chapter 4):

**Citation:** Susanne A. Benz, Peter Bayer, Kathrin Menberg, Stephan Jung, Philipp Blum, Spatial resolution of anthropogenic heat fluxes into urban aquifers, *Science of the Total Environment*, 524–525, 427-439, doi: 10.1016/j.scitotenv.2015.04.003 , 2015.

**Declaration of authorship:** Susanne A. Benz (SB) developed the analytical heat flux model based on the work of Kathrin Menberg (KM) and in consultation with KM, Peter Bayer, and Philipp Blum. Data for Karlsruhe was collected by KM, data for Cologne was collected by Stephan Jung. SB obtained all results and wrote the manuscript. The final manuscript was reviewed by all authors.

### Study 2 (Chapter 5)

**Citation:** Susanne A. Benz, Peter Bayer, Frank M. Goettsche, Folke S. Olesen, Philipp Blum, Linking surface urban heat islands with groundwater temperatures, *Environmental Science & Technology*, 50(1), 70-78, doi: 10.1021/acs.est.5b03672, 2016.

**Declaration of authorship:** Susanne A. Benz (SB) developed the methods and obtained all results in consultation with Peter Bayer and Philipp Blum. Frank M. Goettsche and Folke S. Olesen collected all land surface temperature data. SB wrote the manuscript. The final manuscript was reviewed by all authors.

### Study 3 (Chapter 2)

**Citation:** Susanne A. Benz, Peter Bayer, Philipp Blum, Global patterns of shallow groundwater temperatures, *Environmental Research Letters*, under review.

**Declaration of authorship:** Susanne A. Benz (SB) collected the data, developed the method and obtained all results in consultation with Peter Bayer and Philipp Blum. SB wrote the manuscript. The final manuscript was reviewed by all authors.

### Study 4 (Chapter 3)

**Citation:** Susanne A. Benz, Peter Bayer, Philipp Blum, Identifying anthropogenic anomalies in air, surface and groundwater temperatures in Germany, *Science of the Total Environment*, in press.

**Declaration of authorship:** Susanne A. Benz (SB) collected the data, developed the

method and obtained all results in consultation with Peter Bayer and Philipp Blum. SB wrote the manuscript. The final manuscript was reviewed by all authors.

---

## References

- 1 Cornu, J.-F., Eme, D. & Malard, F. The distribution of groundwater habitats in Europe. *Hydrogeology Journal* **21**, 949-960, doi:10.1007/s10040-013-0984-1 (2013).
- 2 Shiklomanov IA, World water resources: an appraisal for the 21st century, IHP Rep. UN Educ. Sci. Cult. Organ. (UNESCO), Paris, Fr. (1998).
- 3 Haehnlein, S., Bayer, P., Ferguson, G. & Blum, P. Sustainability and policy for the thermal use of shallow geothermal energy. *Energy Policy* (2013).
- 4 IPCC: Climate Change 2013: The Physical Science Basis. Contribution of Working Group I to the Fifth Assessment Report of the Intergovernmental Panel on Climate Change [Stocker, T.F., D. Qin, G.-K. Plattner, M. Tignor, S.K. Allen, J. Boschung, A. Nauels, Y. Xia, V. Bex and P.M. Midgley (eds.)]. Cambridge University Press, Cambridge, United Kingdom and New York, NY, USA, 1535 pp, doi:10.1017/CBO9781107415324 (2013).
- 5 Shook, G. M. Predicting thermal breakthrough in heterogeneous media from tracer tests. *Geothermics* **30**, 573-589, doi:10.1016/S0375-6505(01)00015-3 (2001).
- 6 Pasquale, V., Verdoya, M. & Chiozzi, P. *Geothermics - Heat Flow in the Lithosphere*. (Springer, 2014).
- 7 Davies, J. H. Global map of solid Earth surface heat flow. *Geochemistry Geophysics Geosystems* **14**, 4608-4622, doi:10.1002/ggge.20271 (2013).
- 8 Anderson, M. P. Heat as a ground water tracer. *Ground Water* **43**, 951-968, doi:10.1111/j.1745-6584.2005.00052.x (2005).
- 9 Taylor, C. A. & Stefan, H. G. Shallow groundwater temperature response to climate change and urbanization. *Journal of Hydrology* **375**, 601-612, doi:10.1016/j.jhydrol.2009.07.009 (2009).
- 10 Beltrami, H. & Kellman, L. An examination of short- and long-term air-ground temperature coupling. *Global and Planetary Change* **38**, 291-303, doi:10.1016/S0921-8181(03)00112-7 (2003).

- 11 Hall, F. G., Huemmrich, K. F., Goetz, S. J., Sellers, P. J. & Nickeson, J. E. Satellite Remote-Sensing of Surface-Energy Balance - Success, Failures, and Unresolved Issues in FIFE. *Journal of Geophysical Research-Atmospheres* **97**, 19061-19089 (1992).
- 12 Li, Z.-L. *et al.* Satellite-derived land surface temperature: Current status and perspectives. *Remote Sensing of Environment* **131**, 14-37, doi:10.1016/j.rse.2012.12.008 (2013).
- 13 Sobrino, J. A., Jiménez-Muñoz, J. C. & Paolini, L. Land surface temperature retrieval from LANDSAT TM 5. *Remote Sensing of Environment* **90**, 434-440, doi:10.1016/j.rse.2004.02.003 (2004).
- 14 Land Processes Distributed Active Archive Center (LP DAAC), MODIS L3 1km Land Surface Temperature and Emissivity, Version 5. NASA EOSDIS Land Processes DAAC, USGS Earth Resources Observation and Science (EROS) Center: Sioux Falls, SD, <https://lpdaac.usgs.gov>
- 15 Wan, Z. M. & Dozier, J. A generalized split-window algorithm for retrieving land-surface temperature from space. *Ieee Transactions on Geoscience and Remote Sensing* **34**, 892-905, doi:10.1109/36.508406 (1996).
- 16 Wan, Z. M., Zhang, Y. L., Zhang, Q. C. & Li, Z. L. Validation of the land-surface temperature products retrieved from Terra Moderate Resolution Imaging Spectroradiometer data. *Remote Sensing of Environment* **83**, 163-180, doi:10.1016/S0034-4257(02)00093-7 (2002).
- 17 Wan, Z. New refinements and validation of the MODIS Land-Surface Temperature/Emissivity products. *Remote Sensing of Environment* **112**, 59-74, doi:10.1016/j.rse.2006.06.026 (2008).
- 18 Hachem, S., Duguay, C. R. & Allard, M. Comparison of MODIS-derived land surface temperatures with ground surface and air temperature measurements in continuous permafrost terrain. *Cryosphere* **6**, 51-69, doi:10.5194/tc-6-51-2012 (2012).
- 19 Zhang, P., Bounoua, L., Imhoff, M. L., Wolfe, R. E. & Thome, K. Comparison of MODIS Land Surface Temperature and Air Temperature over the Continental USA Meteorological Stations. *Canadian Journal of Remote Sensing* **40**, 110-122, doi:10.1080/07038992.2014.935934 (2014).

- 
- 20 Walther, G. R. *et al.* Ecological responses to recent climate change. *Nature* **416**, 389-395, doi:10.1038/416389a (2002).
- 21 Peterson, T. C. *et al.* Global rural temperature trends. *Geophysical Research Letters* **26**, 329-332, doi:10.1029/1998gl900322 (1999).
- 22 Hansen, J. *et al.* A closer look at United States and global surface temperature change. *Journal of Geophysical Research-Atmospheres* **106**, 23947-23963, doi:10.1029/2001jd000354 (2001).
- 23 Nordli, O., Hestmark, G., Benestad, R. E. & Isaksen, K. The Oslo temperature series 1837-2012: homogeneity testing and temperature analysis. *International Journal of Climatology* **35**, 3486-3504, doi:10.1002/joc.4223 (2015).
- 24 Ogrin, D. Long-term air temperature changes in Ljubljana (Slovenia) in comparison to Trieste (Italy) and Zagreb (Croatia). *Moravian Geographical Reports* **23**, 17-26, doi:10.1515/mgr-2015-0014 (2015).
- 25 Menberg, K., Blum, P., Kurylyk, B. L. & Bayer, P. Observed groundwater temperature response to recent climate change. *Hydrology and Earth System Sciences* **18**, 4453-4466, doi:10.5194/hess-18-4453-2014 (2014).
- 26 Thomas, C. D. *et al.* Extinction risk from climate change. *Nature* **427**, 145-148, doi:10.1038/nature02121 (2004).
- 27 Karl, T. R. & Trenberth, K. E. Modern global climate change. *Science* **302**, 1719-1723, doi:10.1126/science.1090228 (2003).
- 28 Foley, J. A. *et al.* Global consequences of land use. *Science* **309**, 570-574, doi:10.1126/science.1111772 (2005).
- 29 Costa, M. H. & Foley, J. A. Combined effects of deforestation and doubled atmospheric CO<sub>2</sub> concentrations on the climate of Amazonia. *Journal of Climate* **13**, 18-34, doi:10.1175/1520-0442(2000)013<0018:Ceodad>2.0.Co;2 (2000).
- 30 Oke, T. R. City size and the urban heat island. *Atmospheric Environment (1967)* **7**, 769-779, doi:10.1016/0004-6981(73)90140-6 (1973).
- 31 Bowler, D. E., Buyung-Ali, L., Knight, T. M. & Pullin, A. S. Urban greening to cool towns and cities: A systematic review of the empirical evidence. *Landscape and Urban Planning* **97**, 147-155, doi:10.1016/j.landurbplan.2010.05.006 (2010).
-

- 32 Jauregui, E. Heat island development in Mexico City. *Atmospheric Environment* **31**, 3821-3831, doi:10.1016/S1352-2310(97)00136-2 (1997).
- 33 Santamouris, M. *et al.* On the impact of urban climate on the energy consumption of building. *Solar Energy* **70**, 201-216 (2001).
- 34 Peng, S. *et al.* Surface urban heat island across 419 global big cities. *Environ Sci Technol* **46**, 696-703, doi:10.1021/es2030438 (2012).
- 35 Ward, K., Lauf, S., Kleinschmit, B. & Endlicher, W. Heat waves and urban heat islands in Europe: A review of relevant drivers. *Sci Total Environ* **569-570**, 527-539, doi:10.1016/j.scitotenv.2016.06.119 (2016).
- 36 Menberg, K., Bayer, P., Zosseder, K., Rumohr, S. & Blum, P. Subsurface urban heat islands in German cities. *Sci Total Environ* **442**, 123-133, doi:10.1016/j.scitotenv.2012.10.043 (2013).
- 37 Chow, W. T. L. & Roth, M. Temporal dynamics of the urban heat island of Singapore. *International Journal of Climatology* **26**, 2243-2260, doi:10.1002/joc.1364 (2006).
- 38 Zhou, B., Rybski, D. & Kropp, J. P. On the statistics of urban heat island intensity. *Geophysical Research Letters* **40**, 5486-5491, doi:10.1002/2013GL057320 (2013).
- 39 Kourtidis, K. *et al.* A study of the hourly variability of the urban heat island effect in the Greater Athens Area during summer. *Sci Total Environ* **517**, 162-177, doi:10.1016/j.scitotenv.2015.02.062 (2015).
- 40 Schwarz, N., Lautenbach, S. & Seppelt, R. Exploring indicators for quantifying surface urban heat islands of European cities with MODIS land surface temperatures. *Remote Sensing of Environment* **115**, 3175-3186, doi:10.1016/j.rse.2011.07.003 (2011).
- 41 Imhoff, M. L., Zhang, P., Wolfe, R. E. & Bounoua, L. Remote sensing of the urban heat island effect across biomes in the continental USA. *Remote Sensing of Environment* **114**, 504-513, doi:10.1016/j.rse.2009.10.008 (2010).
- 42 Yow, D. M. Urban Heat Islands: Observations, Impacts, and Adaptation. *Geography Compass* **1**, 1227-1251, doi:10.1111/j.1749-8198.2007.00063.x (2007).

- 
- 43 Patz, J. A., Campbell-Lendrum, D., Holloway, T. & Foley, J. A. Impact of regional climate change on human health. *Nature* **438**, 310-317, doi:10.1038/nature04188 (2005).
- 44 Luber, G. & McGeehin, M. Climate change and extreme heat events. *Am J Prev Med* **35**, 429-435, doi:10.1016/j.amepre.2008.08.021 (2008).
- 45 Dhainaut, J. F., Claessens, Y. E., Ginsburg, C. & Riou, B. Unprecedented heat-related deaths during the 2003 heat wave in Paris: consequences on emergency departments. *Crit Care* **8**, 1-2, doi:10.1186/cc2404 (2004).
- 46 Santamouris, M. On the energy impact of urban heat island and global warming on buildings. *Energy and Buildings* **82**, 100-113, doi:10.1016/j.enbuild.2014.07.022 (2014).
- 47 Watkins, R., Palmer, J., Kolokotroni, M. & Littlefair, P. The balance of the annual heating and cooling demand within the London urban heat island. *Building Services Engineering Research and Technology* **23**, 207-213, doi:10.1191/0143624402bt043oa (2002).
- 48 Jochner, S. & Menzel, A. Urban phenological studies - Past, present, future. *Environ Pollut* **203**, 250-261, doi:10.1016/j.envpol.2015.01.003 (2015).
- 49 Meineke, E. K., Dunn, R. R., Sexton, J. O. & Frank, S. D. Urban warming drives insect pest abundance on street trees. *PLoS One* **8**, e59687, doi:10.1371/journal.pone.0059687 (2013).
- 50 McIntyre, N. E. Ecology of urban arthropods: A review and a call to action. *Annals of the Entomological Society of America* **93**, 825-835, doi:10.1603/0013-8746(2000)093[0825:Eouaar]2.0.Co;2 (2000).
- 51 Eggleston, J. & McCoy, K. J. Assessing the magnitude and timing of anthropogenic warming of a shallow aquifer: example from Virginia Beach, USA. *Hydrogeology Journal* **23**, 105-120 (2014).
- 52 Ferguson, G. & Woodbury, A. D. Urban heat island in the subsurface. *Geophysical Research Letters* **34**, L23713, doi:10.1029/2007gl032324 (2007).
- 53 Headon, J., Banks, D., Waters, A. & Robinson, V. K. Regional distribution of ground temperature in the Chalk aquifer of London, UK. *Quarterly Journal of Engineering Geology and Hydrogeology* **42**, 313-323, doi:10.1144/1470-9236/08-073 (2009).
-

- 54 Muller, N., Kuttler, W. & Barlag, A. B. Analysis of the subsurface urban heat island in Oberhausen, Germany. *Climate Research* **58**, 247-256, doi:10.3354/cr01195 (2014).
- 55 Yalcin, T. & Yetemen, O. Local warming of groundwaters caused by the urban heat island effect in Istanbul, Turkey. *Hydrogeology Journal* **17**, 1247-1255, doi:10.1007/s10040-009-0474-7 (2009).
- 56 Lubis, R. F. *et al.* Assessment of urban groundwater heat contaminant in Jakarta, Indonesia. *Environmental Earth Sciences* **70**, 2033-2038, doi:10.1007/s12665-013-2712-5 (2013).
- 57 Taniguchi, M. *et al.* Anthropogenic effects on the subsurface thermal and groundwater environments in Osaka, Japan and Bangkok, Thailand. *Sci Total Environ* **407**, 3153-3164, doi:10.1016/j.scitotenv.2008.06.064 (2009).
- 58 Allen, A., Milenic, D. & Sikora, P. Shallow gravel aquifers and the urban 'heat island' effect: a source of low enthalpy geothermal energy. *Geothermics* **32**, 569-578, doi:10.1016/S0375-6505(03)00063-4 (2003).
- 59 Arola, T. & Korkka-Niemi, K. The effect of urban heat islands on geothermal potential: examples from Quaternary aquifers in Finland. *Hydrogeology Journal* **22**, 1953-1967, doi:10.1007/s10040-014-1174-5 (2014).
- 60 Zhu, K., Blum, P., Ferguson, G., Balke, K. D. & Bayer, P. The geothermal potential of urban heat islands. *Environmental Research Letters* **5**, art. no. 044002, doi:10.1088/1748-9326/5/4/044002 (2010).
- 61 Bayer, P., Saner, D., Bolay, S., Rybach, L. & Blum, P. Greenhouse gas emission savings of ground source heat pump systems in Europe: A review. *Renewable & Sustainable Energy Reviews* **16**, 1256-1267, doi:10.1016/j.rser.2011.09.027 (2012).
- 62 Blum, P., Campillo, G., Munch, W. & Kolbel, T. CO2 savings of ground source heat pump systems - A regional analysis. *Renewable Energy* **35**, 122-127, doi:10.1016/j.renene.2009.03.034 (2010).
- 63 Gleeson, T., Wada, Y., Bierkens, M. F. & van Beek, L. P. Water balance of global aquifers revealed by groundwater footprint. *Nature* **488**, 197-200, doi:10.1038/nature11295 (2012).



- 
- 64 Gleeson, T., Befus, K. M., Jasechko, S., Luijendijk, E. & Cardenas, M. B. The global volume and distribution of modern groundwater. *Nature Geoscience* **9**, 161-+, doi:10.1038/NGEO2590 (2016).
- 65 Jaramillo, F. & Destouni, G. Local flow regulation and irrigation raise global human water consumption and footprint. *Science* **350**, 1248-1251, doi:10.1126/science.aad1010 (2015).
- 66 Potocnik, J. Renewable energy sources and the realities of setting an energy agenda. *Science* **315**, 810-811, doi:10.1126/science.1139086 (2007).
- 67 Kammen, D. M. & Sunter, D. A. City-integrated renewable energy for urban sustainability. *Science* **352**, 922-928, doi:10.1126/science.aad9302 (2016).
- 68 Danielopol, D. L., Griebler, C., Gunatilaka, A. & Notenboom, J. Present state and future prospects for groundwater ecosystems. *Environmental Conservation* **30**, 104-130, doi:10.1017/S0376892903000109 (2003).
- 69 Stauffer, F., Bayer, P., Blum, P., Molina-Giraldo, N. & Kinzelbach, W. *Thermal Use of Shallow Groundwater*. (2013).
- 70 Rivera, J. A., Blum, P. & Bayer, P. Increased ground temperatures in urban areas: Estimation of the technical geothermal potential. *Renewable Energy*, doi:10.1016/j.renene.2016.11.005 (2016).
- 71 Taniguchi, M., Uemura, T. & Sakura, Y. Effects of urbanization and groundwater flow on subsurface temperature in three megacities in Japan. *Journal of Geophysics and Engineering* **2**, 320-325, doi:10.1088/1742-2132/2/4/S04 (2005).
- 72 Beltrami, H., Matharoo, G. S. & Smerdon, J. E. Ground surface temperature and continental heat gain: uncertainties from underground. *Environmental Research Letters* **10**, 014009, doi:10.1088/1748-9326/10/1/014009 (2015).
- 73 Cey, B. D. On the accuracy of noble gas recharge temperatures as a paleoclimate proxy. *Journal of Geophysical Research* **114**, doi:10.1029/2008jd010438 (2009).
- 74 Taylor, R. G. *et al.* Ground water and climate change. *Nature Climate Change* **3**, 322-329, doi:10.1038/nclimate1744 (2012).
- 75 Pollack, H. N., Huang, S. & Shen, P. Y. Climate change record in subsurface temperatures: A global perspective. *Science* **282**, 279-281 (1998).

- 76 Maxwell, R. M. & Kollet, S. J. Interdependence of groundwater dynamics and land-energy feedbacks under climate change. *Nature Geoscience* **1**, 665-669, doi:10.1038/ngeo315 (2008).
- 77 Kappelmeyer & Haenel, R. *Geothermics with Special References to Application*. Vol. 4 (Gebrüder Borntraeger, 1974).
- 78 Čermák, V., Bodri, L., Šafanda, J., Krešl, M. & Dědeček, P. Ground-air temperature tracking and multi-year cycles in the subsurface temperature time series at geothermal climate-change observatory. *Studia Geophysica et Geodaetica* **58**, 403-424, doi:10.1007/s11200-013-0356-2 (2014).
- 79 Shukla, J. & Mintz, Y. Influence of Land-Surface Evapotranspiration on the Earth's Climate. *Science* **215**, 1498-1501, doi:10.1126/science.215.4539.1498 (1982).
- 80 Sun, Z. G., Wang, Q. X., Batkhishig, O. & Ouyang, Z. Relationship between Evapotranspiration and Land Surface Temperature under Energy- and Water-Limited Conditions in Dry and Cold Climates. *Advances in Meteorology* **2016**, 1-9, doi:10.1155/2016/1835487 (2016).
- 81 Scanlon, B. R., Healy, R. W. & Cook, P. G. Choosing appropriate techniques for quantifying groundwater recharge. *Hydrogeology Journal* **10**, 18-39, doi:10.1007/s10040-001-0176-2 (2002).
- 82 Döll, P. Vulnerability to the impact of climate change on renewable groundwater resources: a global-scale assessment. *Environmental Research Letters* **4**, 035006, doi:10.1088/1748-9326/4/3/035006 (2009).
- 83 Shah, T. Climate change and groundwater: India's opportunities for mitigation and adaptation. *Environmental Research Letters* **4**, 035005, doi:10.1088/1748-9326/4/3/035005 (2009).
- 84 Zhang, T. J. Influence of the seasonal snow cover on the ground thermal regime: An overview. *Reviews of Geophysics* **43**, doi:10.1029/2004rg000157 (2005).
- 85 Banks, D. *et al.* The evolution of alkaline, saline ground- and surface waters in the southern Siberian steppes. *Applied Geochemistry* **19**, 1905-1926, doi:10.1016/j.apgeochem.2004.05.009 (2004).

- 
- 86 Benz, S. A., Bayer, P., Menberg, K., Jung, S. & Blum, P. Spatial resolution of anthropogenic heat fluxes into urban aquifers. *Sci Total Environ* **524-525**, 427-439, doi:10.1016/j.scitotenv.2015.04.003 (2015).
- 87 Fan, Y., Li, H. & Miguez-Macho, G. Global patterns of groundwater table depth. *Science* **339**, 940-943, doi:10.1126/science.1229881 (2013).
- 88 Whittington, A. G., Hofmeister, A. M. & Nabelek, P. I. Temperature-dependent thermal diffusivity of the Earth's crust and implications for magmatism. *Nature* **458**, 319-321, doi:10.1038/nature07818 (2009).
- 89 Wan, Z. MODIS Land-Surface Temperature. Algorithm theoretical basis document (LST ATBD): LST calculations. (1999).
- 90 Ermida, S. L. *et al.* Validation of remotely sensed surface temperature over an oak woodland landscape - The problem of viewing and illumination geometries. *Remote Sensing of Environment* **148**, 16-27, doi:10.1016/j.rse.2014.03.016 (2014).
- 91 Guillevic, P. C. *et al.* Validation of Land Surface Temperature products derived from the Visible Infrared Imaging Radiometer Suite (VIIRS) using ground-based and heritage satellite measurements. *Remote Sensing of Environment* **154**, 19-37, doi:10.1016/j.rse.2014.08.013 (2014).
- 92 Trigo, I. F., Monteiro, I. T., Olesen, F. & Kabsch, E. An assessment of remotely sensed land surface temperature. *Journal of Geophysical Research-Atmospheres* **113**, doi:10.1029/2008jd010035 (2008).
- 93 Google Earth Engine Team, 2015. Google Earth Engine: A planetary-scale geospatial analysis platform. <https://earthengine.google.com>
- 94 Rodell, M. *et al.* The Global Land Data Assimilation System. *Bulletin of the American Meteorological Society* **85**, 381-394, doi:10.1175/bams-85-3-381 (2004).
- 95 Rodell, M., McWilliams, E. B., Famiglietti, J. S., Beaudoing, H. K. & Nigro, J. Estimating evapotranspiration using an observation based terrestrial water budget. *Hydrological Processes* **25**, 4082-4092, doi:10.1002/hyp.8369 (2011).
- 96 Mueller, B. *et al.* Evaluation of global observations-based evapotranspiration datasets and IPCC AR4 simulations. *Geophysical Research Letters* **38**, n/a-n/a, doi:10.1029/2010gl046230 (2011).
-

- 97 Wang, F. *et al.* Evaluation and application of a fine-resolution global data set in a semiarid mesoscale river basin with a distributed biosphere hydrological model. *Journal of Geophysical Research: Atmospheres* **116**, doi:10.1029/2011jd015990 (2011).
- 98 Kato, H. *et al.* Sensitivity of land surface simulations to model physics, land characteristics, and forcings, at four CEOP sites. *Journal of the Meteorological Society of Japan* **85A**, 187-204, doi:10.2151/Jmsj.85a.187 (2007).
- 99 Hall, D. K., Salomonson, V. V., G. A. Riggs, G. A. MODIS/Terra Snow Cover Daily L3 Global 500m Grid. Version 5. Boulder, Colorado USA: NASA National Snow and Ice Data Center Distributed Active Archive Center. (2006)
- 100 Gladkova, I., Grossberg, M., Bonev, G., Romanov, P. & Shahriar, F. Increasing the Accuracy of MODIS/Aqua Snow Product Using Quantitative Image Restoration Technique. *IEEE Geoscience and Remote Sensing Letters* **9**, 740-743, doi:10.1109/Lgrs.2011.2180505 (2012).
- 101 Klein, A. G. & Stroeve, J. Development and validation of a snow albedo algorithm for the MODIS instrument. *Annals of Glaciology, Vol 34, 2002* **34**, 45-52, doi:10.3189/172756402781817662 (2002).
- 102 Tekeli, A. E., Şensoy, A., Şorman, A., Akyürek, Z. & Şorman, Ü. Accuracy assessment of MODIS daily snow albedo retrievals within situ measurements in Karasu basin, Turkey. *Hydrological Processes* **20**, 705-721, doi:10.1002/hyp.6114 (2006).
- 103 Battogtokh, B., Lee, J. M. & Woo, N. Contamination of water and soil by the Erdenet copper–molybdenum mine in Mongolia. *Environmental Earth Sciences* **71**, 3363-3374, doi:10.1007/s12665-013-2727-y (2013).
- 104 Benz, S. A., Bayer, P., Goettsche, F. M., Olesen, F. S. & Blum, P. Linking Surface Urban Heat Islands with Groundwater Temperatures. *Environmental Science & Technology* **50**, 70-78, doi:10.1021/acs.est.5b03672 (2016).
- 105 Zemann, M. *et al.* Sources and processes affecting the spatio-temporal distribution of pharmaceuticals and X-ray contrast media in the water resources of the Lower Jordan Valley, Jordan. *Sci Total Environ* **488-489**, 100-114, doi:10.1016/j.scitotenv.2014.04.063 (2014).
- 106 Touhari, F., Meddi, M., Mehaiguene, M. & Razack, M. Hydrogeochemical assessment of the Upper Cheliff groundwater (North West Algeria).

- 
- Environmental Earth Sciences* **73**, 3043-3061, doi:10.1007/s12665-014-3598-6 (2014).
- 107 Department of Primary Industries, Parks, Water and Environment (DPIPWE), Water Information System of Tasmania, accessed 18 Jan 2016, at URL <http://wrt.tas.gov.au/wist/ui#fopt>
- 108 Department of Environment, Land, Water and Planning, State Government Victoria, Groundwater – data extracts, accessed 14 Jan 2016, at URL <http://data.water.vic.gov.au/monitoring.htm>
- 109 Abteilung Wasserhaushalt im Bundesministerium für Land- und Forstwirtschaft, Umwelt und Wasserwirtschaft (BMLFUW), Austria, Jan 2016, URL <http://ehyd.gv.at/>
- 110 IAEA, International Atomic Energy Agency, Atlas of Isotope Hydrology – Africa; Atlas of Isotope Hydrology – the Americas; and Atlas of Isotope Hydrology - Asia and the Pacific. Water Resources Program, Vienna).
- 111 Buschmann, J., Berg, M., Stengel, C. & Sampson, M. L. Arsenic and manganese contamination of drinking water resources in Cambodia: coincidence of risk areas with low relief topography. *Environ Sci Technol* **41**, 2146-2152 (2007).
- 112 Réseau de suivi des eaux souterraines du Québec, Ministère du Développement durable, de l'Environnement et de la Lutte contre les changements, accessed 29 Apr 2016, at URL <http://www.mddelcc.gouv.qc.ca/EAU/piezo/index.htm>
- 113 Muñoz, M. *et al.* Estimating low-enthalpy geothermal energy potential for district heating in Santiago basin–Chile (33.5 °S). *Renewable Energy* **76**, 186-195, doi:10.1016/j.renene.2014.11.019 (2015).
- 114 Well database, Geological survey of Denmark and Greenland (GEUS), accessed 28 Jan 2016, at URL <http://data.geus.dk/geusmap/?lang=en&mapname=jupiter>
- 115 Britschgi, R., Antikainen, M., Ekholm-Peltonen, M., Hyvärinen, V., Nylander, E., Siiro, P., Suomela, T. Pohjavesialueiden kartoitus ja luokitus. Ympäristöopas 2009. Finnish Environment Institute, Helsinki, (2009).
- 116 BRGM, Bureau de Recherches Géologiques et Minières ; InfoTerre, accessed Apr 24, 2016, at URL <http://infoterre.brgm.fr/viewer/MainTileForward.do>; and Portail nationale d'Accès aux Données sur les Eaux Souterraines, accessed Apr 24, 2016, at URL <http://www.ades.eaufrance.fr/ConsultationPELocalisation.aspx>
-

- 117 Jahresdatenkatalog Grundwasser, Landesanstalt für Umwelt, Messungen und Naturschutz, Baden-Württemberg (LUBW), Germany, accessed 10 Nov 2015 and 28 Jul 2016, at URL <http://193.197.158.205/servlet/is/200/>
- 118 Irawan, D. E. *et al.* Groundwater–surface water interactions of Ciliwung River streams, segment Bogor–Jakarta, Indonesia. *Environmental Earth Sciences* **73**, 1295-1302, doi:10.1007/s12665-014-3482-4 (2014).
- 119 Jassas, H. & Merkel, B. Assessment of hydrochemical evolution of groundwater and its suitability for drinking and irrigation purposes in Al-Khazir Gomal Basin, Northern Iraq. *Environmental Earth Sciences* **74**, 6647-6663, doi:10.1007/s12665-015-4664-4 (2015).
- 120 Jassas, H. A. & Merkel, B. J. Investigating groundwater recharge by means of stable isotopes in the Al-Khazir Gomal Basin, northern Iraq. *Environmental Earth Sciences* **73**, 8533-8546, doi:10.1007/s12665-015-4013-7 (2015).
- 121 Daisy harvester, Helmholtz Centre for Environmental Research (UFZ), accessed 02 Feb 2016, at URL [https://www.ufz.de/daisy\\_harvester/](https://www.ufz.de/daisy_harvester/)
- 122 Zemann, M. *et al.* Tracking changing X-ray contrast media application to an urban-influenced karst aquifer in the Wadi Shueib, Jordan. *Environ Pollut* **198**, 133-143, doi:10.1016/j.envpol.2014.11.033 (2015).
- 123 Mapoma, H. W. T. *et al.* Hydrochemical characteristics of rural community groundwater supply in Blantyre, southern Malawi. *Journal of African Earth Sciences* **114**, 192-202, doi:10.1016/j.jafrearsci.2015.11.023 (2016).
- 124 Pfeiffer, M. *et al.* Investigating arsenic (As) occurrence and sources in ground, surface, waste and drinking water in northern Mongolia. *Environmental Earth Sciences* **73**, 649-662, doi:10.1007/s12665-013-3029-0 (2014).
- 125 Delalande, M. *Hydrologie et géochimie isotopique du lac masoko et de lacs volcaniques de la province active du rungwe (sud-ouest Tanzanie)* PhD thesis, Université Paris Sud, (2008).
- 126 Vystavna, Y., Yakovlev, V., Diadin, D., Vergeles, Y. & Stolberg, F. Hydrochemical characteristics and water quality assessment of surface and ground waters in the transboundary (Russia/Ukraine) Seversky Donets basin. *Environmental Earth Sciences* **74**, 585-596, doi:10.1007/s12665-015-4060-0 (2015).

- 
- 127 Yakovlev, V., Vystavna, Y., Diadin, D. & Vergeles, Y. Nitrates in springs and rivers of East Ukraine: Distribution, contamination and fluxes. *Applied Geochemistry* **53**, 71-78, doi:10.1016/j.apgeochem.2014.12.009 (2015).
- 128 U.S. Geological Survey, 2012, National Water Information System data available on the World Wide Web (USGS Water Data for the Nation), accessed 19 Jan 2016, at URL [http://waterdata.usgs.gov/nwis/dv/?referred\\_module=qw](http://waterdata.usgs.gov/nwis/dv/?referred_module=qw)
- 129 Winkel, L. H. *et al.* Arsenic pollution of groundwater in Vietnam exacerbated by deep aquifer exploitation for more than a century. *Proc Natl Acad Sci U S A* **108**, 1246-1251, doi:10.1073/pnas.1011915108 (2011).
- 130 Alderwish, A. M. & Almatary, H. A. Hydrochemistry and thermal activity of damt region, Yemen. *Environmental Earth Sciences* **65**, 2111-2124, doi:10.1007/s12665-011-1192-8 (2011).
- 131 Rhee, J., Park, S. & Lu, Z. Y. Relationship between land cover patterns and surface temperature in urban areas. *Giscience & Remote Sensing* **51**, 521-536, doi:10.1080/15481603.2014.964455 (2014).
- 132 Skinner, W. R. & Majorowicz, J. A. Regional climatic warming and associated twentieth century land-cover changes in north-western North America. *Climate Research* **12**, 39-52, doi:10.3354/Cr012039 (1999).
- 133 Rotem-Mindali, O., Michael, Y., Helman, D. & Lensky, I. M. The role of local land-use on the urban heat island effect of Tel Aviv as assessed from satellite remote sensing. *Applied Geography* **56**, 145-153, doi:10.1016/j.apgeog.2014.11.023 (2015).
- 134 Hung, T., Uchihama, D., Ochi, S. & Yasuoka, Y. Assessment with satellite data of the urban heat island effects in Asian mega cities. *International Journal of Applied Earth Observation and Geoinformation* **8**, 34-48, doi:10.1016/j.jag.2005.05.003 (2006).
- 135 Doyle, D. & Hawkins, T. W. Assessing a small summer urban heat island in rural South Central Pennsylvania. *Geographical Bulletin - Gamma Theta Upsilon* **49**, 65-76 (2008).
- 136 Hinkel, K. M., Nelson, F. E., Klene, A. F. & Bell, J. H. The urban heat island in winter at Barrow, Alaska. *International Journal of Climatology* **23**, 1889-1905, doi:10.1002/joc.971 (2003).

- 137 Giannopoulou, K. *et al.* On the characteristics of the summer urban heat island in Athens, Greece. *Sustainable Cities and Society* **1**, 16-28, doi:10.1016/j.scs.2010.08.003 (2011).
- 138 Pongracz, R., Bartholy, J. & Dezso, Z. Application of remotely sensed thermal information to urban climatology of Central European cities. *Physics and Chemistry of the Earth* **35**, 95-99, doi:10.1016/j.pce.2010.03.004 (2010).
- 139 Schwarz, N., Schlink, U., Franck, U. & Großmann, K. Relationship of land surface and air temperatures and its implications for quantifying urban heat island indicators—An application for the city of Leipzig (Germany). *Ecological Indicators* **18**, 693-704, doi:10.1016/j.ecolind.2012.01.001 (2012).
- 140 Martin-Vide, J., Sarricolea, P. & Moreno-García, M. C. On the definition of urban heat island intensity: the "rural" reference. *Frontiers in Earth Science* **3**, doi:10.3389/feart.2015.00024 (2015).
- 141 Stewart, I. D. & Oke, T. R. Local Climate Zones for Urban Temperature Studies. *Bulletin of the American Meteorological Society* **93**, 1879-1900, doi:10.1175/bams-d-11-00019.1 (2012).
- 142 Rajasekar, U. & Weng, Q. H. Urban heat island monitoring and analysis using a non-parametric model: A case study of Indianapolis. *ISPRS Journal of Photogrammetry and Remote Sensing* **64**, 86-96, doi:10.1016/j.isprsjprs.2008.05.002 (2009).
- 143 Weber, N., Haase, D. & Franck, U. Zooming into temperature conditions in the city of Leipzig: how do urban built and green structures influence earth surface temperatures in the city? *Sci Total Environ* **496**, 289-298, doi:10.1016/j.scitotenv.2014.06.144 (2014).
- 144 Santamouris, M. Analyzing the heat island magnitude and characteristics in one hundred Asian and Australian cities and regions. *Sci Total Environ* **512-513**, 582-598, doi:10.1016/j.scitotenv.2015.01.060 (2015).
- 145 Menberg, K., Blum, P., Schaffitel, A. & Bayer, P. Long-term evolution of anthropogenic heat fluxes into a subsurface urban heat island. *Environ Sci Technol* **47**, 9747-9755, doi:10.1021/es401546u (2013).
- 146 Hoffmann, P., Krueger, O. & Schlünzen, K. H. A statistical model for the urban heat island and its application to a climate change scenario. *International Journal of Climatology* **32**, 1238-1248, doi:10.1002/joc.2348 (2012).



- 
- 147 Zhang, P., Imhoff, M. L., Wolfe, R. E. & Bounoua, L. Characterizing urban heat islands of global settlements using MODIS and nighttime lights products. *Canadian Journal of Remote Sensing* **36**, 185-196, doi:10.5589/m10-039 (2014).
- 148 Smerdon, J. E. *et al.* Daily, seasonal, and annual relationships between air and subsurface temperatures. *Journal of Geophysical Research-Atmospheres* **111**, doi:10.1029/2004jd005578 (2006).
- 149 Kurylyk, B. L., MacQuarrie, K. T. B. & McKenzie, J. M. Climate change impacts on groundwater and soil temperatures in cold and temperate regions: Implications, mathematical theory, and emerging simulation tools. *Earth-Science Reviews* **138**, 313-334, doi:10.1016/j.earscirev.2014.06.006 (2014).
- 150 Climate Data Center (CDC), Deutscher Wetterdienst (DWD), accessed 4 Jul 2016 at URL <ftp://ftp-cdc.dwd.de/pub/CDC/>
- 151 Benz, S. A., Bayer, P. & Blum, P. Global patterns of shallow groundwater temperatures. *Environmental Research Letters* **in review** (2017).
- 152 GlobCover 2009 Project, ESA, Université Catholique de Louvain, accessed 22 Dec 2015 at URL [http://due.esrin.esa.int/page\\_globcover.php](http://due.esrin.esa.int/page_globcover.php)
- 153 Zensusdatenbank 2011, Statistische Ämter des Bundes und der Länder, accessed 26 May 2016, at URL <https://www.zensus2011.de/SharedDocs/Aktuelles/Ergebnisse/DemografischeGrunddaten.html>
- 154 Regionaldatenbank Deutschland, Statistische Ämter des Bundes und der Länder, accessed 13 Sep 2016, at URL <https://www.regionalstatistik.de>
- 155 Middel, A., Häb, K., Brazel, A. J., Martin, C. A. & Guhathakurta, S. Impact of urban form and design on mid-afternoon microclimate in Phoenix Local Climate Zones. *Landscape and Urban Planning* **122**, 16-28, doi:10.1016/j.landurbplan.2013.11.004 (2014).
- 156 Stewart, I. D., Oke, T. R. & Krayenhoff, E. S. Evaluation of the 'local climate zone' scheme using temperature observations and model simulations. *International Journal of Climatology* **34**, 1062-1080, doi:10.1002/joc.3746 (2014).
- 157 Mellander, C., Lobo, J., Stolarick, K. & Matheson, Z. Night-Time Light Data: A Good Proxy Measure for Economic Activity? *PLoS One* **10**, e0139779, doi:10.1371/journal.pone.0139779 (2015).

- 158 Li, D., Zhao, X. & Li, X. Remote sensing of human beings – a perspective from nighttime light. *Geo-spatial Information Science* **19**, 69-79, doi:10.1080/10095020.2016.1159389 (2016).
- 159 Stegner, J. *Bestimmung thermischer Materialkennwerte von Erdkabelbettungen*. PhD thesis, TU Darmstadt, Germany, (2016).
- 160 Perrier, F., Le Mouel, J. L., Poirier, J. P. & Shnirman, M. G. Long-term climate change and surface versus underground temperature measurements in Paris. *International Journal of Climatology* **25**, 1619-1631, doi:10.1002/joc.1211 (2005).
- 161 Brundl, W. & Hoppe, P. Advantages and Disadvantages of the Urban Heat-Island - an Evaluation According to the Hygro-Thermic Effects. *Archives for Meteorology Geophysics and Bioclimatology Series B-Theoretical and Applied Climatology* **35**, 55-66, doi:10.1007/Bf02269409 (1984).
- 162 Li, W. F. *et al.* Discrepant impacts of land use and land cover on urban heat islands: A case study of Shanghai, China. *Ecological Indicators* **47**, 171-178, doi:10.1016/j.ecolind.2014.08.015 (2014).
- 163 Zhibin, R., Haifeng, Z., Xingyuan, H., Dan, Z. & Xingyang, Y. Estimation of the Relationship Between Urban Vegetation Configuration and Land Surface Temperature with Remote Sensing. *Journal of the Indian Society of Remote Sensing* **43**, 89-100, doi:10.1007/s12524-014-0373-9 (2014).
- 164 Fallmann, J., Emeis, S. & Suppan, P. Mitigation of urban heat stress -a modelling case study for the area of Stuttgart. *Erde* **144**, 202-216, doi:10.12854/erde-144-15 (2013).
- 165 Gioia, A., Paolini, L., Malizia, A., Oltra-Carrio, R. & Sobrino, J. A. Size matters: vegetation patch size and surface temperature relationship in foothills cities of northwestern Argentina. *Urban Ecosystems* **17**, 1161-1174, doi:10.1007/s11252-014-0372-1 (2014).
- 166 Li, D. & Bou-Zeid, E. Quality and sensitivity of high-resolution numerical simulation of urban heat islands. *Environmental Research Letters* **9**, doi:10.1088/1748-9326/9/5/055001 (2014).
- 167 Beltrami, H., Ferguson, G. & Harris, R. N. Long-term tracking of climate change by underground temperatures. *Geophysical Research Letters* **32**, 1 - 4, doi:10.1029/2005gl023714 (2005).

- 
- 168 Taniguchi, M., Uemura, T. & Jago-on, K. Combined effects of urbanization and global warming on subsurface temperature in four Asian cities. *Vadose Zone Journal* **6**, 591-596, doi:10.2136/vzj2006.0094 (2007).
- 169 Gabriel, K. M. & Endlicher, W. R. Urban and rural mortality rates during heat waves in Berlin and Brandenburg, Germany. *Environ Pollut* **159**, 2044-2050, doi:10.1016/j.envpol.2011.01.016 (2011).
- 170 Sarrat, C., Lemonsu, A., Masson, V. & Guedalia, D. Impact of urban heat island on regional atmospheric pollution. *Atmospheric Environment* **40**, 1743-1758, doi:10.1016/j.atmosenv.2005.11.037 (2006).
- 171 Taha, H. Urban climates and heat islands: Albedo, evapotranspiration, and anthropogenic heat. *Energy and Buildings* **25**, 99-103, doi:10.1016/S0378-7788(96)00999-1 (1997).
- 172 Allen, L., Lindberg, F. & Grimmond, C. S. B. Global to city scale urban anthropogenic heat flux: model and variability. *International Journal of Climatology* **31**, 1990-2005, doi:10.1002/joc.2210 (2011).
- 173 Ichinose, T., Shimodozono, K. & Hanaki, K. Impact of anthropogenic heat on urban climate in Tokyo. *Atmospheric Environment* **33**, 3897-3909, doi:10.1016/S1352-2310(99)00132-6 (1999).
- 174 Sailor, D. J. & Lu, L. A top-down methodology for developing diurnal and seasonal anthropogenic heating profiles for urban areas. *Atmospheric Environment* **38**, 2737-2748, doi:10.1016/j.atmosenv.2004.01.034 (2004).
- 175 Kertesz, R. & Sansalone, J. Hydrologic Transport of Thermal Energy from Pavement. *Journal of Environmental Engineering* **140**, doi:10.1061/(Asce)Ee.1943-7870.0000831 (2014).
- 176 Kollet, S. J. *et al.* The Influence of Rain Sensible Heat and Subsurface Energy Transport on the Energy Balance at the Land Surface. *Vadose Zone Journal* **8**, 846-857, doi:10.2136/vzj2009.0005 (2009).
- 177 Zhu, K., Bayer, P., Grathwohl, P. & Blum, P. Groundwater temperature evolution in the subsurface urban heat island of Cologne, Germany. *Hydrological Processes* **29**, 965-978, doi:10.1002/hyp.10209 (2015).

- 178 Hötzl, H. & Makurat, A. Veränderungen der Grundwassertemperaturen unter dicht bebauten Flächen am Beispiel der Stadt Karlsruhe. *Zeitschrift der Deutschen Geologischen Gesellschaft* **132**, 767 - 777 (1981).
- 179 Epting, J., Handel, F. & Huggenberger, P. Thermal management of an unconsolidated shallow urban groundwater body. *Hydrology and Earth System Sciences* **17**, 1851-1869, doi:10.5194/hess-17-1851-2013 (2013).
- 180 Herbert, A., Arthur, S. & Chillingworth, G. Thermal modelling of large scale exploitation of ground source energy in urban aquifers as a resource management tool. *Applied Energy* **109**, 94-103, doi:10.1016/j.apenergy.2013.03.005 (2013).
- 181 Stadt Karlsruhe, Amt für Stadtentwicklung: Statistisches Jahrbuch 2012, accessed 19 Jan 2015, at URL <http://web1.karlsruhe.de/Stadtentwicklung/siska/pdf/Jahrbuch2012.pdf>
- 182 Stadt Köln. Amt für Stadtentwicklung und Statistik: Kölner Stadtteilinformationen – Zahlen 2010, accessed 19 Jan 2015, at URL [http://www.stadt-koeln.de/mediaasset/content/pdf15/stadtteilinformationen\\_2010.pdf](http://www.stadt-koeln.de/mediaasset/content/pdf15/stadtteilinformationen_2010.pdf)
- 183 Deutscher Wetterdienst (DWD) Web-based Weather Request and Distribution System, accessed 20 May 2014, at URL <http://www.dwd.de/>
- 184 Geyer, O. F. & Gwinner, M. P. *Geologie von Baden-Württemberg*. 5 edn, (Schweizerbart, 2011).
- 185 Haehnlein, S., Bayer, P. & Blum, P. International legal status of the use of shallow geothermal energy. *Renewable & Sustainable Energy Reviews* **14**, 2611-2625, doi:10.1016/j.rser.2010.07.069 (2010).
- 186 Balke, K. D. Geothermische und hydrogeologische Untersuchungen in der südlichen Niederrheinischen Bucht., (Hannover: Bundesanstalt für Bodenforschung und den Geologischen Landesämtern der Bundesrepublik Deutschland., 1973).
- 187 Jung, S. *Wärmefluss in der urbanen Wärmeinsel Köln* M.Sc. thesis, KIT, (2013).
- 188 Global Monitoring for environment and security (GMES), European Environment Agency: Urban Atlas, accessed 19 Jan 2015, at URL <http://www.eea.europa.eu/data-and-maps/data/urban-atlas>

- 
- 189 Zeitung für kommunale Wirtschaft (Zfk) (2001), Fernwärmeumfrage. Energieverluste aus dem Fernwärmenetz, accessed 23 May 2013, at URL <http://zfk.ve.m-online.net/navframe/umfrage01.pdf>
- 190 Dědeček, P., Šafanda, J. & Rajver, D. Detection and quantification of local anthropogenic and regional climatic transient signals in temperature logs from Czechia and Slovenia. *Climatic Change* **113**, 787-801 (2012).
- 191 Verein Deutscher Ingenieure (VDI). Thermische Nutzung des Untergrunds: Grundlagen, Genehmigungen, Umweltaspekte (Thermal use of the underground: Fundamentals, approvals, environmental aspects). VDI 4640. Beuth Verlag GmbH, Berlin, (2010).
- 192 Deutsches Institut für Normung e.V. DIN EN ISO 13370: Wärmetechnisches Verhalten von Gebäude - Wärmeübertragung über das Erdreich (Thermal performance of buildings - Heat transfer via the ground); Beuth Verlag GmbH: Berlin, (2008).
- 193 Makurat, A. *Analyse der Temperaturschwankungen des Grundwassers im Stadtgebiet von Karlsruhe* Diploma Thesis thesis, Universität Karlsruhe (TH), Karlsruhe, Germany, (1980).
- 194 Stadtentwässerungsbetriebe, Einzugsgebiete der Kläranlagen, Köln, accessed 9 Jan 2013, at URL <http://www.steb-koeln.de/klaeranlagen.html>
- 195 Stadt Karlsruhe. Tiefbauamt Karlsruhe: Die Stadtentwässerung in Karlsruhe, accessed 20 Mar 2013, at URL [http://www.karlsruhe.de/b3/bauen/tiefbau/entwaesserung/entwaesserungsgebuehr/HF\\_sections/content/ZZk9uVuzOo24XJ/ZZk9uWfqOuhpKP/Tiefbauamt\\_Broschuer\\_e\\_2010.pdf](http://www.karlsruhe.de/b3/bauen/tiefbau/entwaesserung/entwaesserungsgebuehr/HF_sections/content/ZZk9uVuzOo24XJ/ZZk9uWfqOuhpKP/Tiefbauamt_Broschuer_e_2010.pdf)
- 196 Eiswirth, M., Held, I., Hötzl, H. & Wolf, L. Abwasser im urbanen Grundwasserleiter: Stoffeintrag, Umsetzung und Gefährdungspotential. In Progress Report, Gorscherguppe Kanalleckage: Gefährdungspotential von Abwasser aus undichten Kanälen für Boden und Grundwasser. (Universität Karlsruhe (TH), Karlsruhe, Germany, 2002).
- 197 Klinger, J. *Beschreibung der Wasser- und Stoffflüsse in einem urbanen Raum unter besonderer Berücksichtigung von Kanalleckagen* Ph.D. thesis, Universität Karlsruhe (TH), Karlsruhe, Germany, (2007).

- 198 Rheinenergie AG, (2011), Geschäftsbericht (Daten des Fernwärmenetzes), accessed 23 May 2013, at URL [http://www.rheinenergie.com/de/unternehmensportal/ueber\\_uns/rheinenergie/geschaeftsberichte/index.php](http://www.rheinenergie.com/de/unternehmensportal/ueber_uns/rheinenergie/geschaeftsberichte/index.php)
- 199 Kölner Verkehrsbetriebe (KVB), accessed 15 May 2013, at URL <http://www.nord-sued-stadtbahn.de>
- 200 Deutsches Institut für Normung e.V. DIN 4108-2: Wärmeschutz und Energie-Einsparung in Gebäuden - Teil 2: Mindestanforderungen an den Wärmeschutz (Thermal protection and energy economy in buildings - Part 2: Minimum requirements to thermal insulation); Beuth Verlag GmbH: Berlin, (2011).
- 201 Balke, K. D. Das Grundwasser als Energieträger. *Brennstoff-Wärme-Kraft* **29** (1977).
- 202 Timm, U. Wohnsituation in Deutschland 2006 - Ergebnisse der Mikrozensus-Zusatzerhebung,. (2008).
- 203 Nitsch, J. Struktur und Entwicklung der zukünftigen Stromversorgung Baden-Württembergs. (Arbeitsgemeinschaft DLR/ISI/ZSW, 2002).
- 204 Rigo, G. & Parlow, E. Modelling the ground heat flux of an urban area using remote sensing data. *Theoretical and Applied Climatology* **90**, 185-199, doi:10.1007/s00704-006-0279-8 (2007).
- 205 Liebenthal, C. & Foken, T. Evaluation of six parameterization approaches for the ground heat flux. *Theoretical and Applied Climatology* **88**, 43-56, doi:10.1007/s00704-005-0234-0 (2007).
- 206 Baker, J. M. & Baker, D. G. Long-term ground heat flux and heat storage at a mid-latitude site. *Climatic Change* **54**, 295-303, doi:10.1023/A:1016144718218 (2002).
- 207 Wild, M. *et al.* The global energy balance from a surface perspective. *Climate Dynamics* **40**, 3107-3134, doi:10.1007/s00382-012-1569-8 (2013).
- 208 Beltrami, H., Bourlon, E., Kellman, L. & Gonzalez-Rouco, J. F. Spatial patterns of ground heat gain in the Northern Hemisphere. *Geophysical Research Letters* **33**, doi:10.1029/2005gl025676 (2006).

- 
- 209 Rees, S. W., Thomas, H. R. & Zhou, Z. Ground heat transfer: Some further insights into the influence of three-dimensional effects. *Building Services Engineering Research and Technology* **21**, 233-239 (2000).
- 210 Thomas, H. R. & Rees, S. W. The thermal performance of ground floor slabs - a full scale in-situ experiment. *Building and Environment* **34**, 139-164 (1999).
- 211 Ferguson, G. & Woodbury, A. D. Subsurface heat flow in an urban environment. *Journal of Geophysical Research-Solid Earth* **109**, B02402 02401 - 02409, doi:10.1029/2003jb002715 (2004).
- 212 Cermak, V. & Rybach, L. *Terrestrial heat flow in Europe*. (Springer Verlag, 1979).
- 213 Menberg, K. *Anthropogenic and natural alterations of shallow groundwater temperatures* PhD thesis, KIT, (2013).
- 214 Zhang, Y., Soga, K. & Choudhary, R. Shallow geothermal energy application with GSHPs at city scale: study on the City of Westminster. *Géotechnique Letters* **4**, 125-131, doi:10.1680/geolett.13.00061 (2014).
- 215 Arola, T., Eskola, L., Hellen, J. & Korkka-Niemi, K. Mapping the low enthalpy geothermal potential of shallow Quaternary aquifers in Finland. *Geothermal Energy* **2**, 1-20, doi:10.1186/s40517-014-0009-x (2014).
- 216 Shi, B., Tang, C. S., Gao, L., Liu, C. & Wang, B. J. Observation and analysis of the urban heat island effect on soil in Nanjing, China. *Environmental Earth Sciences* **67**, 215-229, doi:10.1007/s12665-011-1501-2 (2012).
- 217 Cheon, J. Y., Ham, B. S., Lee, J. Y., Park, Y. & Lee, K. K. Soil temperatures in four metropolitan cities of Korea from 1960 to 2010: implications for climate change and urban heat. *Environmental Earth Sciences* **71**, 5215-5230, doi:10.1007/s12665-013-2924-8 (2014).
- 218 Shamir, E. & Georgakakos, K. P. MODIS Land Surface Temperature as an index of surface air temperature for operational snowpack estimation. *Remote Sensing of Environment* **152**, 83-98, doi:10.1016/j.rse.2014.06.001 (2014).
- 219 Chakraborty, S. D., Kant, Y. & Mitra, D. Assessment of land surface temperature and heat fluxes over Delhi using remote sensing data. *J Environ Manage* **148**, 143-152, doi:10.1016/j.jenvman.2013.11.034 (2015).

- 220 Hu, L. Q. & Brunsell, N. A. A new perspective to assess the urban heat island through remotely sensed atmospheric profiles. *Remote Sensing of Environment* **158**, 393-406, doi:10.1016/j.rse.2014.10.022 (2015).
- 221 Smerdon, J. E. *et al.* Air-ground temperature coupling and subsurface propagation of annual temperature signals. *Journal of Geophysical Research-Atmospheres* **109**, D21107 21101-21110, doi:10.1029/2004jd005056 (2004).
- 222 Kooi, H. Spatial variability in subsurface warming over the last three decades; insight from repeated borehole temperature measurements in The Netherlands. *Earth and Planetary Science Letters* **270**, 86-94, doi:10.1016/j.epsl.2008.03.015 (2008).
- 223 Majorowicz, J. & Safanda, J. Measured versus simulated transients of temperature logs - a test of borehole climatology. *Journal of Geophysics and Engineering* **2**, 291-298, doi:10.1088/1742-2132/2/4/S01 (2005).
- 224 Huang, S., Pollack, H. N. & Shen, P. Y. Temperature trends over the past five centuries reconstructed from borehole temperatures. *Nature* **403**, 756-758, doi:10.1038/35001556 (2000).
- 225 Huang, S., Taniguchi, M., Yamano, M. & Wang, C. H. Detecting urbanization effects on surface and subsurface thermal environment--a case study of Osaka. *Sci Total Environ* **407**, 3142-3152, doi:10.1016/j.scitotenv.2008.04.019 (2009).
- 226 Zhan, W. *et al.* Satellite-derived subsurface urban heat island. *Environ Sci Technol* **48**, 12134-12140, doi:10.1021/es5021185 (2014).
- 227 Hannappel, S. & Limberg, A. Ermittlung des Flurabstands des oberflächennahem Grundwassers in Berlin (Determination of the floor distance of shallow groundwater in Berlin). *Brandenburg. geowiss. Beitr.* **14**, 65-74 (2007).
- 228 Kerl, M., Runge, N., Tauchmann, H. & Goldscheider, N. Conceptual hydrogeological model of the City of Munich, Germany, as a basis for geothermal groundwater utilisation. *Grundwasser* **17**, 127-135, doi:10.1007/s00767-012-0199-8 (2012).
- 229 Dugord, P. A., Lauf, S., Schuster, C. & Kleinschmit, B. Land use patterns, temperature distribution, and potential heat stress risk - The case study Berlin, Germany. *Computers Environment and Urban Systems* **48**, 86-98, doi:10.1016/j.compenvurbsys.2014.07.005 (2014).



- 230 Open Street Map; © OpenStreetMap contributors, accessed 13 Jul 2015, at URLs <http://www.openstreetmap.org/copyright>; <http://www.openstreetmap.org>; <http://opendatacommons.org>
- 231 Balke, K. D. *Die Grundwassertemperaturen in Ballungsgebieten*; Forschungsbericht – T81-028 (Institutional research report T81-028); Geologisches Landratsamt Nordrhein-Westfalen, Krefeld; (1981).
- 232 Senate Department for Urban Development and the Environment, Berlin. Environmental Atlas, accessed 04 Jul 2015, at URL [http://www.stadtentwicklung.berlin.de/umwelt/umweltatlas/edua\\_index.shtml](http://www.stadtentwicklung.berlin.de/umwelt/umweltatlas/edua_index.shtml)
- 233 Zhou, H. *et al.* Horizontal Heat Impact of Urban Structures on the Surface Soil Layer and Its Diurnal Patterns under Different Micrometeorological Conditions. *Sci Rep* **6**, 18790, doi:10.1038/srep18790 (2016).
- 234 Schiel, K., Baume, O., Caruso, G. & Leopold, U. GIS-based modelling of shallow geothermal energy potential for CO<sub>2</sub> emission mitigation in urban areas. *Renewable Energy* **86**, 1023-1036, doi:10.1016/j.renene.2015.09.017 (2016).



# Curriculum Vitae

## Personal Information

Name	Susanne Amelie Benz
Date of Birth	04.05.1987
Place of Birth	Reutlingen
Nationality	German

## Education

2000-2006	A-level, Keppler Gymnasium, Freudenstadt
-----------	--

## Academic Studies

10/2007-10/2010	University of Konstanz Department of Physics Bachelor of Science (Grade: 2.0)  Bachelor Thesis: <i>“Identification of simultaneous Pc5 Events”</i> Written at the University of KwaZulu-Natal, Institute of Space Physics, South Africa
10/2010-03/2013	Georg August University Goettingen Faculty of Physics Master of Science (Grade: 1.8)  Master Thesis: <i>“Konstruktion und Feldtest von Silber-Silberchlorid- Elektroden für langperiodische Magnetotellurik”</i> <i>(Development of silver chloride electrodes for long-period magnetotellurics )</i>

## Professional Experiences

05/2013-12/2016	Karlsruhe Institute of Technology (KIT) Institute for Applied Geosciences PhD Student  PhD Thesis: <i>“Human Impact on Groundwater Temperatures”</i>
-----------------	---

**Journal Publications (peer – reviewed)**

S. A. Benz, P. Bayer, K. Menberg, S. Jung, P. Blum, Spatial resolution of anthropogenic heat fluxes into urban aquifers. *Science of the Total Environment*, 524-525, 427 (2015).

S. A. Benz, P. Bayer, F. M. Goettsche, F. S. Olesen, P. Blum, Linking Surface Urban Heat Islands with Groundwater Temperatures. *Environmental Science & Technology*, 50 (1), 70 (2016).

S. A. Benz, P. Bayer, P. Blum, Global patterns of shallow groundwater temperatures. Submitted to 'Environmental Research Letters'.

S. A. Benz, P. Bayer, P. Blum, Identifying anthropogenic anomalies in air, surface and groundwater temperatures in Germany. *Science of the Total Environment*, in press.

**Conference abstracts**

S. A. Benz, P. Bayer, K. Menberg, P. Blum, Comparison of local and regional heat transport processes into the subsurface urban heat island of Karlsruhe, Germany, Abstract accepted for the EGU General Assembly 2014; Poster

S. A. Benz, P. Bayer, K. Menberg, S. Jung, P. Blum, Anthropogene Wärme-flüsse in das Grundwasser von Karlsruhe und Köln, Abstract accepted for the Meeting of the German Association for Hydrogeology 2014 (Tagung der Fachsektion Hydrogeologie in der DGGV 2014); oral presentation

S. A. Benz, P. Bayer, K. Menberg, P. Blum, Spatial resolution of subsurface anthropogenic heat fluxes in cities, Abstract accepted for the EGU General Assembly 2015; Poster (presented by Co-Author P. Bayer)

S. A. Benz, P. Bayer, K. Menberg, P. Blum, Anthropogenic heat fluxes into subsurface urban heat islands, Abstract accepted for the IUGG General Assembly 2016; oral presentation

S. A. Benz, P. Bayer, F. Goettsche, F. Olesen, P. Blum, Remote Sensing of Urban Groundwater Temperatures, Abstract accepted for the 2016 AGU Fall Meeting; oral presentation

S. A. Benz, P. Bayer, F. Goettsche, F. Olesen, P. Blum, Satellitengestützte Fernerkundung urbaner Wärmeinseln im Grundwasser, Abstract accepted for the Meeting of the German Association for Hydrogeology 2016 (Tagung der Fachsektion Hydrogeologie in der DGGV 2016); oral presentation

S. A. Benz, P. Bayer, K. Menberg, P. Blum, Combined Geothermal Potential of Subsurface Urban Heat Islands, Abstract accepted for the EGU General Assembly 2016; Poster (presented by Co-Author P. Blum)

S. A. Benz, P. Bayer, F. Goettsche, F. Olesen, P. Blum, Link between Surface and Subsurface Urban Heat Islands, Abstract accepted for the EGU General Assembly 2016; oral presentation (presented by Co-Author P. Blum)